From the

Medizinische Klinik and Poliklinik I (Cardiology)

of the Ludwig-Maximilians-Universität München

Director: Prof. Dr. med. Steffen Massberg

DISSERTATION

zum Erwerb des Doctor of Philosophy (Ph.D.)

an der Medizinischen Fakultät der

Ludwig-Maximilians-Universität zu München

The role of calcium signaling analysis in myeloid leukocyte activation and interactions in inflammation

submitted by

Fitsumbirhan Tetemke Mehari

from

Addis Ababa, Ethiopia

Munich, 2021

Mit Genehmigung der Medizinischen Fakultät der

Ludwig-Maximilians-Universität zu München

First supervisor: PD. Dr. med. Konstantin Stark

Second supervisor*:*   Prof. Dr. med. Steffen Massberg

Third supervisor: Prof. Dr. med. Christian Schulz

Dean: **Prof. Dr. med. dent. Reinhard Hickel**

Date of oral defence: 30.04.2021

Abstract

Inflammation is the pathophysiologic basis of many diseases that are main causes of mortality. Caused by environmental or microbial factors, inflammation leads to the destruction of tissue around the primary focus and expands to other tissues when not resolved in a timely manner. The body's mechanism for inflammation resolution is based on an interplay of immune cells that first drive a pro-inflammatory response necessary for recruiting neutrophils and macrophages that phagocytose debris and dendritic cells that relay information to lymphocytes that build up the body's adaptive immunity. Neutrophils are key to this process as they are the first cell type to recognize damage and pathogen associated molecular patterns (DAMPs and PAMPs). Eventually, they undergo necrosis amplifying the chemokine and cytokine gradient needed for added neutrophil swarming and other cells' recruitment. In addition to the release of chemokine cues, neutrophil necrosis results in the release of reactive oxygen species that is an additional mediator of tissue damage.

Although the literature hints at a cellular interplay as mechanism to prevent excessive neutrophil-induced tissue damage, there is to date no tool to investigate intravital leukocyte activation patterns *in vivo* in this setting. For this purpose, we turned to calcium (Ca^{++}) signaling since it is known to be involved in most aspects of cellular function. By using myeloid leukocyte specific Ca^{++} reporter strains together with *in vivo* two-photon and spinning disk confocal microscopy in a sterile inflammation mouse model, we developed an image analysis algorithm of frequency spectra that offers the following insights: macrophages react to sterile inflammation by Ca^{++} transients in a distinct spatiotemporal pattern and neutrophils vary their intracellular dynamics during the migration cascade in a Gαi-protein-coupled receptor-dependent manner. Furthermore, during resolution of inflammation we observed tissue macrophages (TMs) physically contacting injury-bound neutrophils with their dendrites and instructing them to withdraw. Ca^{++} signal analysis displays that both cell types undergo cellular activation adjustments during interaction. Finally, we uncovered that the HMGB1-TLR4 axis is responsible for TM dendrite formation and that LFA-1 mediates neutrophil interaction with these dendrites. Therefore, we have uncovered a mechanism how tissue inflammation is limited through macrophage-neutrophil interactions.

Table of content

Table of content

Table of content

List of figures

List of tables

List of abbreviations

2P-IVM	Two-photon excitation intravital microscopy
bp	Base pair
Ca^{++}	Calcium ion
CaM	Calmodulin
CCD	Charge-coupled Device
CFU	Colony forming unit
CRAC	Calcium-release-activated channel
CRP	C-reactive protein
CX3CL1	Chemokine (C-X-C motif) 3 ligand 1
CX3CR1	Chemokine (C-X-C motif) 3 receptor 1
CXCL	Chemokine (C-X-C motif) ligand
CXCR	Chemokine (C-X-C motif) receptor
DNA	Deoxyribonucleic Acid
dNTP	Deoxyribonucleoside triphosphate
DAMP	Damage-associated molecular pattern
E. coli	Escherichia coli
EDTA	Ethylenediaminetetraacetic acid
ER	Endoplasmic Reticulum
ESAM	Endothelial cell-selective adhesion molecule
fMLP	N-Formylmethionine-leucyl-phenylalanine
FoV	Field of View
G-CSF	Granulocyte-Colony Stimulating Factor
GFP	Green fluorescent protein
Gαi-PCRS	G-protein coupled receptor
HMGB1	High mobility group box 1
ICAM	Intercellular adhesion molecule
IL-1β	Interleukin-1 beta
IL-6	Interleukin-6
i.p.	Intraperitoneal
i.v.	Intravenous
kg	Kilogram
ki	Knock-in
LFA-1	Lymphocyte function-associated antigen 1
LI	Laser injury
LSCM	Laser scanning confocal microscopy

List of abbreviations

µg	Microgram
µl	Microliter
M13	Myosin-light-chain kinase peptide
mHz	Millihertz
ml	Milliliter
ms	Millisecond
NA	Numerical aperture
NET	Neutrophil extracellular trap
nm	Nanometer
PAMP	Pathogen-associated molecular pattern
PBS	Phosphate-buffered saline
PCR	Polymerase chain reaction
PECAM-1	Platelet endothelial cell adhesion molecule 1
PRR	Pattern recognition receptor
PSD	Power spectral density
PTx	Pertussis toxin
RAGE	Receptor for advanced glycation end products
RAP	RAGE antagonist peptide
rpm	Rounds per minute
RPMI	Roswell Park Memorial Institute
ROS	Reactive oxygen species
SDCM	Spinning disk confocal microscopy
SOCE	Store-operated Calcium entry
TLR-4	Toll-like receptor 4
TNF-α	Tumor necrosis factor
TM	Tissue macrophage
wt	Wild type
ZT	Zeitgeber time

1. Introduction

1.1 Sterile inflammation

Inflammation is the process of the body, which is attained when undesired external agents result in bodily harm in order to contain invading pathogens and to promote tissue recovery. The consequences of such a damage can range from a barely noticeable swelling and soreness resulting from a flu shot to severe trauma leading to cytokine release syndromes and cytokine storms, and consequently multiple organ failures (Aikawa 1996). Inflammation can be acute or chronic in its nature. Acute inflammations usually lie at the higher end of the severity level and are mostly associated with quick responses to an external insult, for example, the fore mentioned flu shot. They are important in relatively quick repair of tissue damage, fight infection during that process and fulfill their purpose within several days to weeks. On the other hand, chronic inflammation is relatively less intense in the immediate response but fail to subside for considerably longer periods, sometimes even spanning a whole lifetime. Well-known examples of chronic inflammation are arthritis, atherosclerosis and bowel diseases like ulcerative colitis and Crohn's disease. Chronic inflammation carries an important socio-economic burden in human lives at times rendering subjects unable to carry out work (Jacobs, Bissonnette, and Guenther 2011). The differences between acute and chronic inflammation are detailed in **Table 1**.

Table 1: Acute versus chronic inflammation

	Acute inflammation	Systemic chronic inflammation
Trigger	PAMPs (infection), DAMPs (cellular stress, trauma)	DAMPs ('exposome', metabolic dysfunction, tissue damage)
Duration	Short-term	Persistent, non-resolving
Magnitude	High-grade	Low-grade
Outcome(s)	Healing, trigger removal, tissue repair	Collateral damage
Age-related	No	Yes
Biomarkers	IL-6, TNF-α, IL-1β, CRP	Silent — no canonical standard biomarkers
Magnitude	High-grade	Low-grade

(adapted from (Furman et al. 2019) with the kind permission of Springer Nature)

There are two types of inflammation: sterile, the main focus of this thesis, and microbial inflammation. Both types of inflammation are sensed by cells of the immune system via pattern recognition receptors (PRRs), more specifically damage-associated molecular patterns

1. Introduction

(DAMPs) in sterile inflammation and pathogen-associated molecular patterns (PAMPs) in microbial inflammation (Hato and Dagher 2015).

Sterile inflammation is triggered by tissue damage from non-infectious causes. Examples of such causative agents are stress, ischemia, mechanical trauma, environmental conditions such as exposure to UV radiation and asbestos or even cancer caused by genetic mutations (Mossman and Churg 1998), (Mantovani et al. 2008). Neutrophils and other ROS producing immune cells infiltrate all kinds of tissues to mitigate inflammation but overexposure leads to further tissue damage (Wilgus, Roy, and McDaniel 2013). Therefore, it is of utmost importance that such events are limited only to the necessary extent by mechanisms put in place to remove apoptotic cells from the necrosis site.

In the center of sterile inflammation, we find immune cells orchestrating the body's response to initiate tissue inflammation, limit the damage and bring it back to homeostasis as quickly as possible. There is an ever-increasing type of immune cells and interactions responsible for this complex undertaking that happens quietly and regularly, rarely failing to accomplish the goal. A very long and meticulous evolutionary tailoring of the genetic basis of this feat, most of which we do not comprehend, has resulted in a robust system by-in-large. It is in the instances where it fails that understanding the basic cellular interactions presents both a challenge and an opportunity for intervention. Thus far, we have uncovered that sterile inflammation is initiated by the release of molecules such as the alarmin HMGB1, fMLP, and ATP which normally would reside in the cytosol or nucleus. These molecules in turn trigger a proinflammatory response within the blood vessels, setting the leukocyte recruitment cascade into motion. Perivascular pericytes then facilitate the transmigration of leukocytes into the tissue. Once in the tissue, we know that leukocytes are guided to the site of necrosis by a combination of various chemokine gradients but not much more (Stark et al. 2013).

Small laser-induced injuries (microlesion) in the mouse peritoneum were shown to be physically shielded from neutrophil swarming by dendrite-forming macrophages (Uderhardt et al. 2019). TMs first formed dendritic extensions from all sides of the microlesion, effectively sealing it. Upon arrival, the first responder neutrophils fail to physically contact the debris and become activated leading to no swarming. In the absence of TMs, neutrophils successfully swarmed the microlesion and initiated inflammation. In the case of a bigger injury (macrolesion), TMs are not able to sufficiently cloak the lesion allowing first responder neutrophils to contact the debris, initiate swarming and induce collateral tissue damage. The same cascade of events was also observed in the absence of TMs. Mechanistically, the study points to nucleotide-induced TM sensing of microlesions while the physical extension of dendrites for cloaking is mediated by Receptor for Advanced Glycation End products (RAGE) and Gαi-PCRS s. Roughly 24 hours after induction, cloaked microlesions were shown to have

almost disappeared or shrunk significantly in size while non-cloaked lesions, be it micro or macro, increased in size. Those non-cloaked lesions that ended up getting bigger needed monocyte involvement to attain resolution. TM cloaking was also in muscle dystrophy mouse model and was shown to reduce the inflammatory effects of neutrophils to a certain extent. Another therapeutic target that interferes with cellular interactions is Annexin A1. Annexin A1, also known as lipocortin-1, inhibits neutrophil accumulation in the tissue, stimulates monocyte recruitment to site of inflammation and promotes clearance of apoptotic neutrophils by macrophages (Sugimoto et al. 2016). This supports the concept that leukocyte interactions (especially neutrophil-macrophage interactions) are an important target in sterile inflammation resolution and hence forms the basis of this dissertation.

1.2 The leukocyte recruitment and migration cascade

In order for immune cells to reach a site of damage or combat pathogens in the tissue, they first need to pass the endothelial barrier of blood vessels that transport them all over the body. This process is conducted in a series of steps and mediated by various molecular interactions between immune cells and endothelial cells. Among a list of many immune cells that undergo this process, neutrophils and monocytes are the two most important in the setting of sterile and microbial inflammation. This dissertation focuses on neutrophils and the characterization of these steps as well as their interactions with other tissue-resident immune cells during sterile and bacterial inflammation (**Figure 1**).

1. Introduction
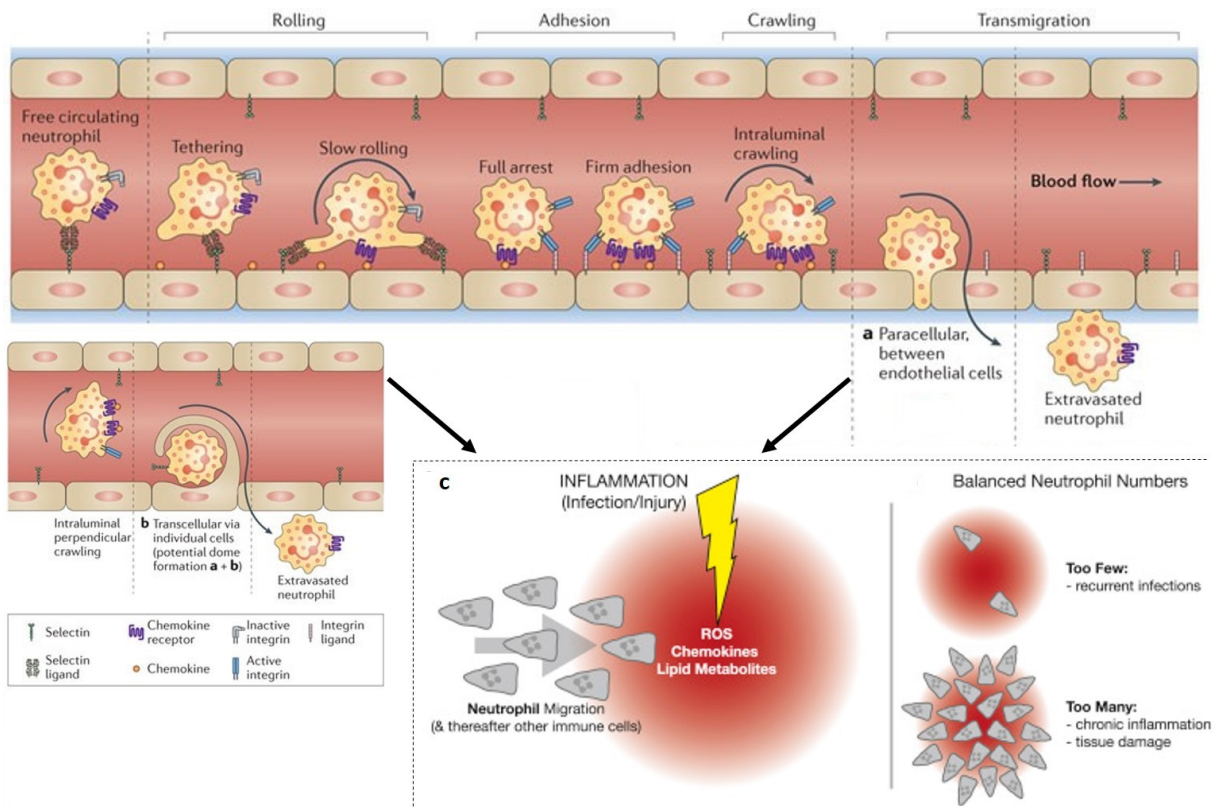
Figure 1: Neutrophil recruitment cascade to sterile inflammation

Neutrophil intravascular and cross barrier migration is mediated via a range of ligand-receptor interactions between neutrophils and endothelial cells and by the cellular milieu surrounding venules. This interaction leads more commonly to neutrophil paracellular transmigration (**a**) but also to transcellular transmigration (**b**). Release of damage or pathogen associated cytokines from necrosis sites recruits and amplifies neutrophil response. Recruitment of neutrophils to necrosis sites is dependent on tissue gradient of PAMPs, DAMPs, chemokines, and lipid mediators (**c**).

(Adapted from (Kolaczkowska and Kubes 2013) and (Renkawitz and Sixt 2016) with the kind permission of Springer Nature and Elsevier, respectively)

1.2.1 From bone marrow to peripheral blood

Although the most abundant immune cell type, neutrophils spend most of their time in the bone marrow where they differentiate from myeloid progenitor cells into mature neutrophils. In steady-state conditions, only about 2% are found within the blood and spend only several hours there owing to clearance roles played by the liver, spleen and bone marrow itself (Rankin 2010). Despite this, during inflammatory or infectious conditions, neutrophils are the first responders and do so at very large numbers (Summers et al. 2010). In order to facilitate this transition, stimulating factors like G-CSF, and chemokines like CXCL1/2 released from tissue damage and detected by receptors like CXCR2 facilitate the egress of neutrophils from the bone marrow into blood while other receptors like CXCR4 favor retention in the bone marrow (**Figure 2)** (Semerad et al. 2002).
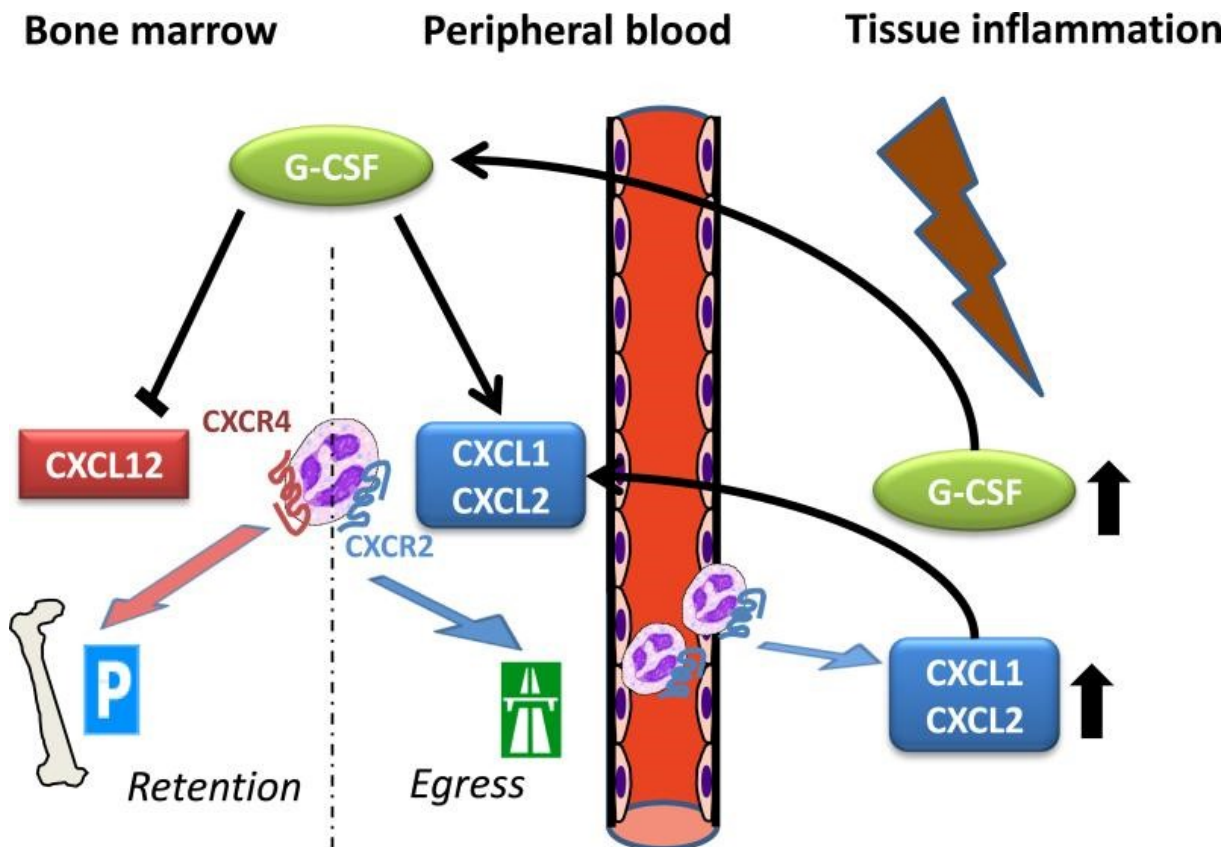
Figure 2: Neutrophil egress from bone marrow

The CXCR2 ligands CXCL1 and CXCL2 stimulate neutrophil egress while the CXCR4 ligand CXCL12 promotes retention of neutrophils in the bone marrow. G-CSF production is enhanced during tissue inflammation which in turn helps mobilize neutrophils from the bone marrow.

(Adapted from (Sadik, Kim, and Luster 2011)) with the kind permission of Elsevier)

1.2.2 Rolling

Neutrophils are in constant homeostasis within the blood flow in a circadian rhythm fashion, owing to production in the bone marrow and clearance in different organs where they effect their functions (Zhang et al. 2015), (Suratt et al. 2001). In steady-state conditions, neutrophils are circulated with the blood and do not interact with the endothelium. However, once inflammatory signals originating from sterile or bacterial inflammation are released, neutrophils slowdown to form transient interactions with the endothelium resulting in rolling. These interactions are made between VCAM-1 and ICAM-1 on endothelial cells and PSGL-1, P-/L-/E-selectin, ß2 integrins, Integrin α-L (CD11a), Integrin α-4 (CD49d), or CXCR4 (CD184) on neutrophils (He et al. 2018). VCAM-1 and ICAM-1 are inducible endothelial counter-receptor ligands for the integrins mentioned above (Rahman and Fazal 2009). ß2 integrins have three conformations of different ligand binding affinities, depending on which they can bind to ligands and neutrophils exhibit rolling (Fan and Ley 2015). Rolling cells exhibit slower migration speeds than neutrophils in free flow; depending on the type of interaction, neutrophils undergo E-

selectin mediated slow rolling (< 5 μm/s) or P-/L-selectin mediated fast rolling (> 5 μm/s) (Kunkel and Ley 1996).

1.2.3 Adhesion and arrest

Neutrophil arrest occurs when stronger interactions happen with the endothelium. These strong interactions replace those that initiate rolling and are mediated by Beta2 integrins. CXCR2 induces arrest in neutrophils through LFA-1 activation. Talin-1 and Kindlin-3 are two integrin co-activators that have important roles in bringing about LFA-1 conformational rearrangements resulting in neutrophil arrest (Lefort and Ley 2012). Neutrophil arrest effectively reduces rolling speed to 0 μm/s. It has been shown that neutrophil arrest is a reversible process, whereby adherent neutrophils can detach from the endothelium and re-enter blood flow (Sadik, Kim, and Luster 2011).

1.2.4 Transmigration

The first step of transmigration is locating a hotspot on the endothelium through which neutrophils can leave the vasculature. Also referred to as intraluminal migration, crawling or diapedesis is the process by which arrested neutrophils very slowly migrate over the endothelium into the interstitial space until the transmigration process is initiated. Pericytes, mural cells that wrap around the endothelium, form an important part of transmigration initiation. Pericyte gaps in the endothelium serve as hotspots through which neutrophils transmigrate, mediated by ICAM-1 expressed by pericytes and its receptors LFA-1 and Mac-1 on neutrophils (Proebstl et al. 2012), (Hyun et al. 2019). Neutrophils mostly squeeze through endothelial cell-cell junctions (paracellular transmigration) but can also pass through endothelial cells (transcellular transmigration). Adhesion molecules such as ESAM, PECAM-1 and CD99 are known to mediate paracellular transmigration (Lou et al. 2007), (Wegmann et al. 2006). Unlike neutrophil arrest, transmigration cannot be reversed once started (Sadik, Kim, and Luster 2011). Once in the interstitial tissue and having effected their inflammatory functions, neutrophils that are not phagocytosed can partly reenter the vasculature by a process known as reverse transmigration (Mathias et al. 2006), (Buckley et al. 2006), (de Oliveira, Rosowski, and Huttenlocher 2016). On the other hand, another study by Woodfin et al. showed that reverse transmigration in neutrophils can lead to the distribution of proinflammatory molecules resulting in systematic inflammation (Woodfin et al. 2011).

1.2.5 Interstitial migration

Upon completion of the transmigration process, neutrophils enter a state of abluminal crawling between endothelial cells and pericytes. Following this, they enter the interstitial tissue and are directed towards the site of necrosis by a gradient of DAMPs or chemokines originating from other immune cells already at the site of necrosis (Weninger, Biro, and Jain 2014). It has been shown in the inflamed skin that neutrophils that contacted pericytes were able to interstitially

migrate to the focal necrosis faster (Stark et al. 2013). During this process, neutrophils migrate through a maze of collagen fibers by constantly shifting their shape into lamellipodia and uropods by constant cytoskeletal rearrangements (Friedl, Borgmann, and Brocker 2001), (Voisin, Woodfin, and Nourshargh 2009). This allows the neutrophils to move at an average speed of 10 µm/minute and a peak of 30 µm/minute, and to be the first immune cells at the site of necrosis. At the damage site, neutrophils then go through apoptosis exposing yet more DAMPs and intensifying neutrophil swarming until the damage is contained, a phenomenon marked by monocyte swarming (Weninger, Biro, and Jain 2014). Neutrophil interstitial response to laser-induced lesions in the mouse skin has been shown to happen in well-defined steps: 1) Neutrophils in proximity to lesion sense short-range chemoattractants. 2) These first neutrophils travel to the lesion and undergo apoptosis releasing DAMPs that amplify further neutrophil recruitment. 3) LTB4, released from neutrophils, intensifies the chemotactic response to even more distant sites (up to 300 µm). 4) A wound seal is formed through the clustering of neutrophils that requires LTB4, CXCR2 ligands, and FPR2 ligands. 5) Neutrophils cease to swarm the lesion site at the same time as CX3CR1 monocytes migrate to the lesion site (Lammermann 2016).

1.3 Neutrophil-macrophage interaction in sterile inflammation

Neutrophils and TMs have been shown to interact during inflammation to effect their pathogen and debris clearing functions (Prame Kumar, Nicholls, and Wong 2018). Monocytes recruited to the interstitial tissue differentiate into M1 (proinflammatory) TMs, phagocytose debris and pathogens inducing the release of G-CSF, and thereby promote neutrophil recruitment into the tissue. Upon inflammation resolution, M1 TMs induce neutrophil apoptosis, phagocytose them and shift to an M2 (pro-resolution) phenotype denoting homeostasis restoration (**Figure 3**) (Hamilton et al. 2014). Moreover, neutrophils secrete cytokines such as IL-13 and CSF-1 that shape the macrophage gene expression polarization (Bouchery and Harris 2019). Tauzin et al. showed that in zebrafish that macrophage contact induced reverse migration in neutrophils at the edge of the wound (Tauzin et al. 2014). This was reflected by an inverse correlation between the number of macrophages and neutrophils at the site of the wound. Finally, (Bouchery and Harris 2019) further highlight how the neutrophil-macrophage interaction fosters proliferative tissue remodeling. In this process, macrophages are shown to be shifted in polarization by microvesicles and cytokines released by neutrophils while neutrophils attain N1 (immunostimulant) or N2 (immunosuppressive) polarizations much like macrophages themselves.

1. Introduction
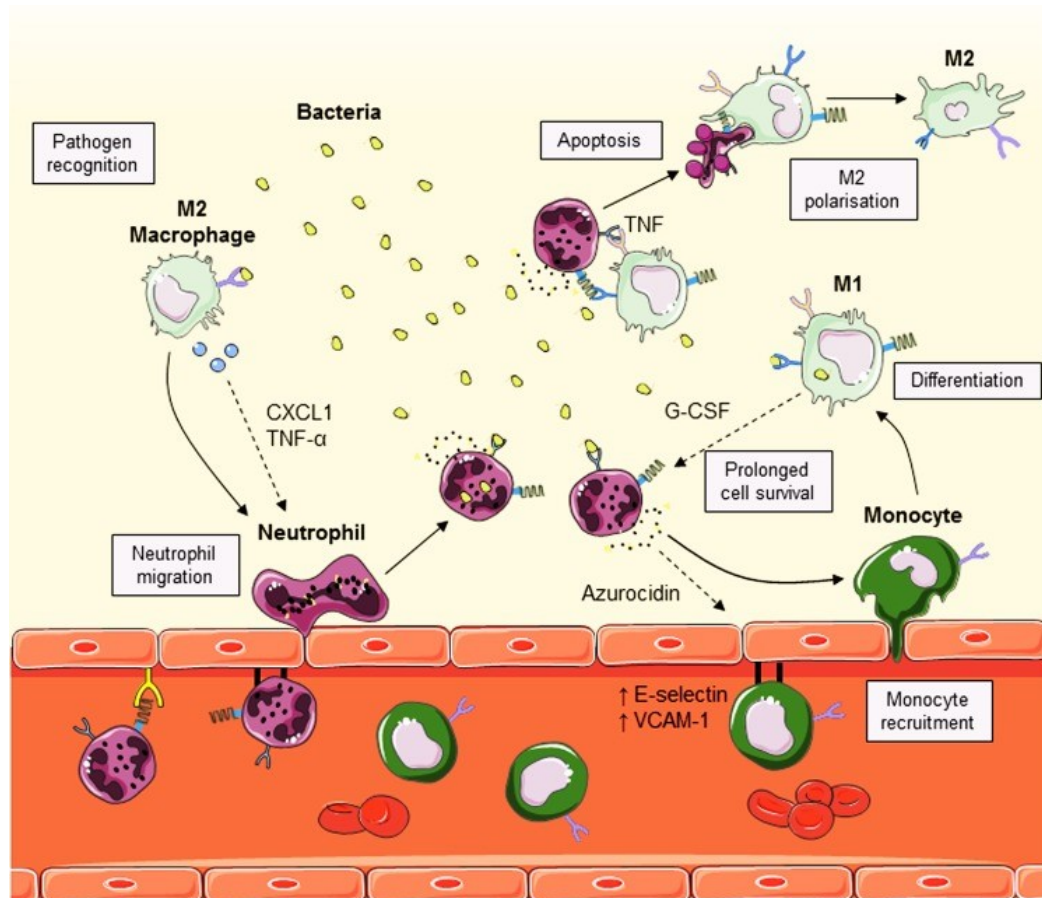
Figure 3: Neutrophils interact with tissue macrophages (TM)

After recognizing pathogens, M2 TM-produced CXCL1 and TNF-α promote neutrophil transmigration. Neutrophils in turn kill bacteria and thereby increase monocyte recruitment by VCAM-1 and E-selectin expression on the endothelium. These transmigrated monocytes differentiate into M1 macrophages and continue to kill the invading bacteria while producing G-CSF, which helps neutrophils persist. Upon inflammation resolution, M1 macrophages induce neutrophil apoptosis via TNF binding. M1 macrophages then proceed to clear apoptotic neutrophils and attain an M2 polarization, through which homeostasis is re-established.

(Adapted from (Prame Kumar, Nicholls, and Wong 2018))

1.4 Molecular mechanisms involved in sterile inflammation

1.4.1 Damage associated molecular patterns

HMGB1 is a nuclear protein that was one of the very first DAMPs to be described in the literature (Goodwin, Sanders, and Johns 1973), (Scaffidi, Misteli, and Bianchi 2002). It has also been described as an important mediator of the inflammatory process within the tissue (Wang et al. 1999), (Musumeci, Roviello, and Montesarchio 2014). HMGB1 is released from necrotic cells either passively when their cell membranes lose stability or actively through lysosomal transport from the nucleus (He et al. 2017).

HMGB1 is a nonhistone chromatin-binding DAMP in the nucleus which transmits proinflammatory signals from necrotic cells. Comprised of 215 amino acids, it is compartmentalized into two HMG boxes; box-A and box-B. Two cysteine residues at positions

1. Introduction

23 and 45 in box-A and one more at position 106 in box-B create sites of redox modifications depending on which HMGB1 acquires various biological functions. Owing to their proximity in the primary structure, Cys23 and Cys45 can form a disulfide bond, while Cys106 remains reduced, that leads to proinflammatory cytokine release via TLR4. When all three cysteine residues are in the reduced state, RAGE induced autophagy occurs (Tang et al. 2010). Upon binding of CXCL12 and signaling via CXCR4, this fully reduced form brings about cell migration and tissue regeneration (Schiraldi et al. 2012), (Tirone et al. 2018). The oxidization of the cysteines to sulfonates results in resolution of inflammation (Venereau et al. 2012). In summary, HMGB1 is an important mediator known to be involved in both pro-inflammatory and pro-resolution aspects of sterile inflammation.

Although HMGB1 is the most widely known DAMP, there are others such as heat shock proteins, ATP and uric acid that are generated as a result of proteolysis in dying cells and promote tissue repair and remodeling(Chen and Nunez 2010).

1.4.2 Pattern recognition receptors

PRRs are a crucial part of the properly functioning innate immune system. They are proteins found on the outer membranes of leukocytes that are able to recognize molecules from pathogens or damaged cells. Signals resulting from their ligand binding results in important pro-inflammatory or germicidal response (Amarante-Mendes et al. 2018). A member of the toll-like receptor family, TLR4 is a transmembrane protein that is classified as a PRR and expressed by myeloid leukocytes. When bound to a response eliciting ligand, it leads to activation of the NF-κB signaling pathway and cytokine release that in turn activate other innate immune system cells (Vaure and Liu 2014). Recently, (Wang et al. 2019) showed that the HMGB1-TLR4 axis is involved in neutrophil recruitment in response to neutrophil extracellular trap-microparticle complexes in the setting of sterile inflammation (Wang et al. 2019).

First discovered in the early 1990 by (Neeper et al. 1992), RAGE received its name from its affinity to advanced glycation endproducts like glycoproteins (Neeper et al. 1992). Also a PRR like TLR-4, RAGE is another important transmembrane receptor expressed by myeloid leukocytes and results in pro-inflammatory reactions when bound to one of its many ligands. Many of the calcium-binding S100 family proteins and HMGB1 have been shown to bind to RAGE (Hermani et al. 2006), (Ibrahim et al. 2013). Furthermore, these RAGE ligands, including HMGB1, S100 and Advanced Glycation End products, have been shown to activate TMs via TLR4 and RAGE thereby activating inflammatory MyD88 signaling. In that way, TLR4/RAGE signaling has been shown to promote phagocytosis and chemotaxis in TMs (Prantner, Nallar, and Vogel 2020).

1.4.3 Adhesion molecules

An integrin expressed by lymphocytes and leukocytes, LFA-1 is a receptor molecule that plays an important role in cellular arrest of neutrophils on endothelial cells prior to transmigration (Lefort et al. 2012), (Dixit et al. 2012). Its most potent group of receptors is the ICAM protein family, which plays an important role in the inflammatory response by neutrophils (Salomon and Bluestone 1998), (Wojcikiewicz et al. 2006), (Pflugfelder et al. 2017) . More importantly, LFA-1 expressed on macrophages triggers ICAM-1 binding by neutrophils and eventually adhesion (Ding et al. 1999). (Li et al. 2018) showed that macrophage-1 antigen (Mac-1) facilitate LFA-1-JAM-C bonds that trigger neutrophil spreading and polarization and accelerate neutrophil crawling under high shear stress (Li et al. 2018). (Ding et al. 1999). also showed the contribution of LFA-1 and Mac-1 to neutrophil adhesion and migration (Ding et al. 1999). There is therefore reason to believe LFA-1 also mediates neutrophil-TM interstitial interaction.

1.4.4 Pathogen associated molecular patterns

Microbial inflammation is caused by pathogens such as bacteria, viruses, pathogens, protozoa and fungi (Chen and Nunez 2010). Although humans depend on symbiotic relationships with microorganisms in many different ways, the shift from these relationships leads to inflammatory diseases such as those in the gut (Ong and Yim 2017). PAMPs are small molecular patterns that are conserved within these microbes and can be sensed by PRRs. Bacteria are a major cause of microbial inflammations. Because immune cells sense bacterial presence based on molecular patterns present on bacterial cell wall such as fMLP and lipopolysaccharides (Newton and Dixit 2012), one can simulate and initiate bacterial inflammatory responses by solely presenting these molecular patterns to the immune cells. This represents a model to study bacterial inflammation.

1.5 Classical parameters for studying leukocyte migration and interaction

1.5.1 Leukocyte migration patterns

Leukocytes sense molecular patterns emanating from inflammation sites, integrate them using PRRs and adapt to them intracellularly by in one of many ways involving a shift in their cytoskeletal structure. TMs for instance are known to undergo cytoskeletal activation leading to shape changes such as protrusion formations without effectively moving. Neutrophils on the other hand have been shown to go through various types of migration patterns depending on the environment they are in. When not attached to a surface, neutrophils induce non-directed migration (chemokinesis) in the absence of a chemokine gradient whereas they follow chemotaxis when a chemokine gradient is present. When attached to a surface, they carry out what is in general called hapto-migration. Upon perception of surface chemokines such as those on the endothelium, neutrophils initiate haptokinesis which allows them to stay confined to a small area and probe it in a non-directed manner. Once they receive a sense of the chemokine gradient along the endothelium, they engage in haptotaxis which allows them to

crawl towards the source of the chemokines. In all forms of migration patterns, expansion and contraction of the actin network is what allows the amoeboid-like migration patterns of leukocytes (Lammermann and Sixt 2009), (Lammermann and Germain 2014).

1.5.2 Speed

One of the mostly used parameters to quantify cell migration is speed. It could be regarded as one way of telling how strongly attracted a cell is towards a certain target (e.g. cell or injury site). If on the other hand one is investigating cellular-substrate interaction (e.g. a rolling cell starting to adhere onto endothelial wall or platelets spreading on a fibrinogen coated surface), how quickly they lose speed quantifies how intense the interaction is.

1.5.3 Displacement rate

This parameter is essentially the speed but only accounts the starting and finishing points of a cell's migration. In **Figure 4a**, it is the length of the straight line (black) over the time the cell took along the actual migration path (red). The higher the displacement rate, the more ground a cell has covered in a fixed amount of time or the same ground in a smaller amount of time; i.e. reflecting on the directed nature of its migration (Beltman, Maree, and de Boer 2009).

1.5.4 Meandering index (track straightness)

It describes how straight the path a cell takes from start to endpoint is. The direct distance from start to end of the cell (black) is divided through the complete migration path covered (red) (**Figure 4B**). The shortest path, a straight line, results in a 1 whereas a circular path with the same start and endpoint is 0, while all sorts of meandering paths lie somewhere in between. The straighter a path, the more directed the migration of a cell is considered (Beltman, Maree, and de Boer 2009), (Benhamou 2004).
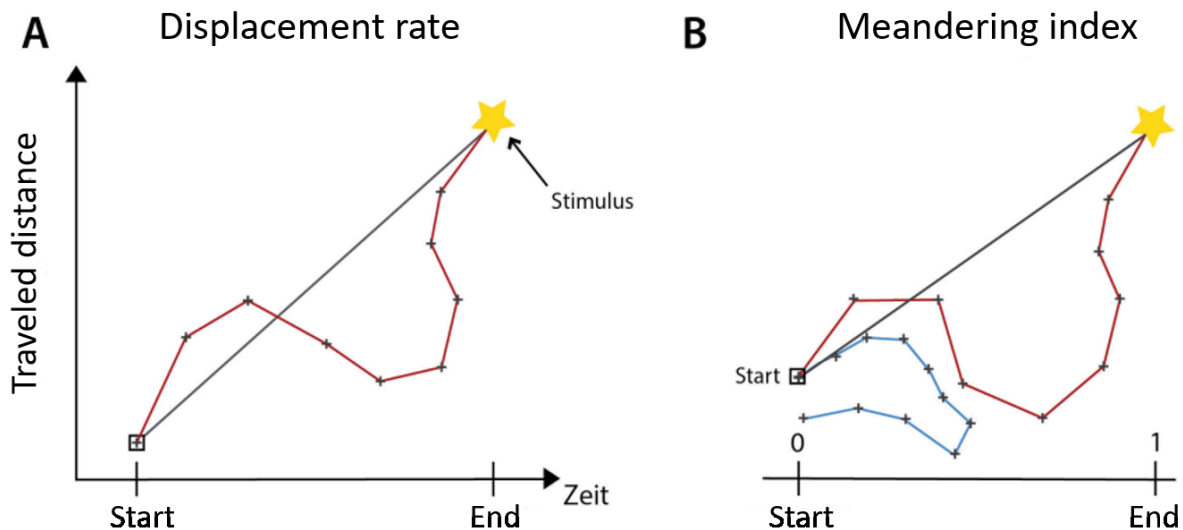
Figure 4: Depiction of a cell's displacement rate and meandering index

A cell's displacement rate the amount of time it takes to travel a certain distance (A). Its meandering index is a measure of how straight its path is; the more linear it is, the closer its value lies to 1 (red line). If it is more circular, meaning that its starting and end points lie near each other, its meandering index lies closer to 0 (blue line) (B).

(Adapted from (Miller 2015)) with the kind permission of Meike Miller)

1.5.5 Cellular morphology

Depending on the surrounding they are in, leukocytes adopt different shapes allowing them to cover more ground, stay stationary or initiate interaction with other cells or objects (e.g. a laser injury). Within the vasculature, neutrophils in flow are round in shape as that it best suited for easy flow. Once these cells acquire inflammatory signals, they start to lose their roundness in favor of a more flattened structure as they begin to roll and adhere on the endothelium. This flattened structure becomes even more evident during paracellular or transcellular transmigration into the interstitial area as cells mobilize actin filaments from the center to the outer edges. Once in tissue, cells adopt a more amoeboid migration technique. It has been shown that neutrophils morphology can be a useful indicator of diagnosis and prognosis of sepsis (Zonneveld, Molema, and Plotz 2016). TMs on the other hand effect their functions from a stationary position (Uderhardt et al. 2019). Largely limited to a sedentary position, our lab previously showed that they grow protrusions known as dendrites with which they can probe a laser injury or interact with neutrophils (Boda 2019). Therefore, cellular morphology is an important indicator of cellular activation and functional states.

1.6 Calcium signaling in leukocytes

Calcium (Ca^{++}) is a ubiquitous doubly-charged positive ion that is required in every part of the body for its normal function. Ca^{++} homeostasis is required for a variety of important cellular activities. The role of Ca^{++} ions in cells ranges from gene transcription, fertilization and cellular

communication to effector functions such as autophagy and phagocytosis (Russell 2011). Moreover, Ca^{++} has been found to be involved in neutrophil chemotaxis, leukocyte-endothelial cell adhesion and transmigration, neutrophil apoptosis at site of inflammation, and macrophage phagocytosis of apoptotic neutrophils that reprograms them into a phenotype of inflammation resolution (Ortega-Gomez, Perretti, and Soehnlein 2013), (Serhan et al. 2020), (Dalal et al. 2021).

1.6.1 Calcium signaling as a parameter in leukocyte migration and interaction

Because Ca^{++} is so integral in the activation of immune cells in their effector functions during inflammation, Ca^{++} has long been used to measure the activation status of immune cells. Starting about 30 years ago, scientists were able to load leukocytes *in vitro* with organic cell permeant Ca^{++} indicators like Fura-2 and Fluo-4 (Tsien 1981) that allowed them to compare the effects of different stimulation factors (Zou et al. 2012), to investigate the roles of various genes in response to inflammations (de Seabra Rodrigues Dias et al. 2017) and to study neuronal development and function (Sharma et al. 2020). With the advent of transgenic techniques, scientists came up with Ca^{++} reporter cell lines that could endogenously report Ca^{++} concentrations in the form of fluorescence (Heim et al. 2007). Coupling transgenic techniques to advances in microscopy brought about the possibility to do *in vivo* Ca^{++} imaging first in invertebrates such as insects and worms (Dal Santo et al. 1999) and in small vertebrates like the zebrafish (Friedrich and Korsching 1997). Further developments led to *in vivo* Ca^{++} imaging in mice, some even where the subjects were freely moving (Lutcke et al. 2010).

With all the technological and biological advances mentioned above, we have come to learn exactly how intricately Ca^{++} signaling is embedded in the lives of innate immune cells. What allows innate immune cells across the board to use this single mechanism to regulate their functions is the enormous versatility it carries in the form of a toolkit that can be mixed and matched to create specific spatial and temporal signals. In their inactivated status, immune cells maintain a low intracellular Ca^{++} concentration by stowing away their cellular stores in the endoplasmic reticulum (ER) and mitochondria or by pumping it out of the cytoplasm (Duchen 2000). This 'OFF' mechanism allows them to buffer the local Ca^{++} concentration in cellular microdomains. Upon polarization of their membranes through contact with other cells or chemokines, intracellular 'ON' signals mainly regulated by inositol-1,4,5-trisphosphate, cyclic ADP ribose, and sphingosine-1-phosphate mobilize the release of internally stored Ca^{++} and opening up of plasma membrane channels resulting in the increase of cytoplasmic Ca^{++} concentration. These 'ON' signals are then converted into physiological responses (Berridge, Lipp, and Bootman 2000).

The involvement of numerous mediators in the 'ON' and 'OFF' signals in Ca^{++} signals allows for an extensive temporal range using which numerous cellular physiological responses can

be conveyed. This coupled to Ca^{++} signaling being a very rapid process results in vastly varied transients known as sparks, quarks, puffs and blips, which can in turn be combined in various ways to make up waves (Eisner and Trafford 1996), (Berridge, Lipp, and Bootman 2000). At the onset of life, mammalian cells require Ca^{++} spikes that persist for several hours to initiate fertilization (Miyazaki et al. 1993). Following that, Ca^{++} signaling drives the proliferation and differentiation of the zygote (Webb and Miller 2000). Ca^{++} spikes have been shown to play a role in cell differentiation of neural and muscle cells (Buonanno and Fields 1999), xenopus myocytes into somites (Ferrari et al. 1998), and neurons in mice (Carey and Matsumoto 1999). Moreover, during the lives of immune cells Ca^{++} signaling plays the very important role of transcription faction activation (Crabtree 1999). Finally, Ca^{++} waves have been implicated in the progression (Benzaquen et al. 1995) and apoptosis of cells from human liver cancer cell line (Szalai, Krishnamurthy, and Hajnoczky 1999).

1.6.2 Calcium channels

The patch clamp technique introduced us long ago to the importance of Ca^{++} channels in leukocyte electrophysiology (Gallin 1986). Ca^{++} ions are transported in and out of cells through various types of channels on the plasma membrane that help healthy cells maintain a certain concentration of Ca^{++} ions that is required for their normal activity (Krebs, Agellon, and Michalak 2015). Ca^{++} ion channels can be categorized into two levels: higher and lower levels. Higher level refer to those that are on the plasma membrane and are readily affected by external factors. A good example of a higher level channel are voltage-gated Ca^{++} channels coupled to Gαi-protein coupled receptors (Gαi-PCRs); factors that interact with this receptor directly lead to intracellular Ca^{++} concentration regulation and cell signaling (Zamponi 2015). This induction of Ca^{++} signaling at the higher level leads to lower level channels that regulate the intracellular Ca^{++} homeostasis more intricately. This refers to those that execute Ca^{++} flux inherently from the cell. STIM1 and ORAI1 are good examples of lower level channels. Located on the Endoplasmic Reticulum (ER) membrane, STIM1 undergoes a structural change upon depletion of Ca^{++} in the ER allowing it to interact with ORAI1 on the plasma membrane forming the basis of store-operated Ca^{++} entry (SOCE). This interaction in turn leads to an opening of the pore-forming subunit of the calcium-release-activated channel (CRAC) of the ORAI1 channel, allowing further Ca^{++} influx and efflux (Muik et al. 2008), (Ong et al. 2015). Because higher level Ca^{++} homeostasis serves as the basis for all subsequent Ca^{++} signaling, this dissertation focuses on understanding its role in cellular interactions during inflammation.

1.6.3 Calcium channelopathy

These channels play such an important role in Ca^{++} homeostasis that a failure in even one of them could result in various autoimmune malignancies. Among the main reasons why Ca^{++} channels lose their functionality are loss-and gain-of-function mutations. Loss-of-function mutations occur when the resulting gene is either totally or partially inactivated. On the other

hand, gain-of-function mutations result in products from the affected gene with an enhanced activation capacity. Loss-of-function gene mutations in the CRAC channels STIM1 and ORAI1, also known as CRAC channelopathy, eradicate their function in SOCE (Lacruz and Feske 2015). This leads to several phenotypes such as thrombocytopenia and platelet dysfunction (Picard et al. 2009), autoimmunity (Fuchs et al. 2012), ectodermal dysplasia such as amelogenesis imperfecta (McCarl et al. 2009) and muscular hypotonia. Gain-of-function mutations in STIM1 and ORAI1 on the other hand cause another host of diseases; tubular aggregate myopathy in skeletal muscles, York platelet syndrome resulting in mild bleeding diathesis, and Stormorken syndrome in platelets resulting in similar bleeding diathesis, small stature, and cognitive defects (Lacruz and Feske 2015).

1.6.4 Calcium imaging and signal analysis

Ca^{++} signaling is clearly a fundamental process in normal cellular activity and overall organism well-being, and in its restoration when it is pushed out of balance by one reason or another. This aspect has been understood by researchers of cell biology since long ago and ways to characterize it have thus been developed. *In vitro* patch clamp experiments introduced the following parameters as standard (Saxena, Ganguly, and Chattopadhyay 2012):

- normalized intensity – or simply signal intensity directly corresponds to the intracellular Ca^{++} concentration. This allows the back calculation of concentration from intensity values both for *in vitro* and *in vivo* scenarios (Maravall et al. 2000),
- dose response plots – these plot spikes per individual cells versus maximum fold change showing, for instance, dependence on ligand concentration,
- amplitude – reflects the maximum fold change in intracellular Ca^{++},
- full width at half maxima (FWHM) – shows how long ligand-induced intracellular Ca^{++} concentration spikes are maintained and,
- area under the intensity-vs-time curve – denotes the total amount of Ca^{++} released during spikes.

Frequency analysis of Ca^{++} signals presented a way of defining cellular Ca^{++} signaling that allowed newer insight into means of information transformation by different cell types (**Figure 5**) (Smedler and Uhlen 2014).
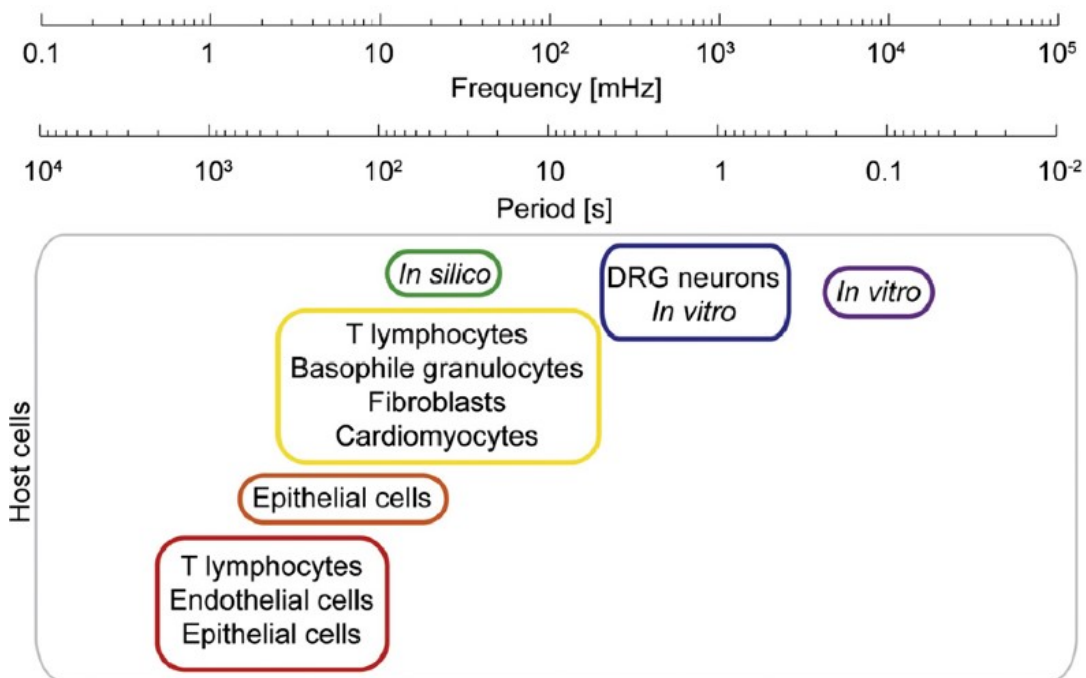
Figure 5: Ca++ signal frequencies and periods in immune cells

Different Ca++-signal periods and frequencies are used by immune cells to modulate their activities.

(Adapted from (Smedler and Uhlen 2014))

Although these signals were all first described for *in vitro* systems, they hold an even more meaningful place *in vivo* since cellular signaling effects cannot be accurately replicated when the whole physiological milieu is missing. Similarly, many disease states – especially sterile inflammation that involves so much of the surrounding cellular infrastructure – cannot be dependably duplicated *in vitro* (Russell 2011). For instance, (Oka et al. 2006) showed that in drosophila odorant receptor-specific glomeruli exhibited different ligand spectra and greater sensitivity *in vivo* in comparison to pericams *in vitro* (Oka et al. 2006)*.* This goes to show *in vivo* Ca++ experiments are well superior in investigating disease states.

1.6.5 The GCaMP5G fusion protein as a tool for in vivo Ca++ imaging

To study Ca++ levels and dynamics *in vivo* several tools have been developed. A genetically encoded calcium indicator, GCaMP is a fusion of 3 different proteins: green fluorescent protein (GFP), calM13modulin (CaM) and Myosin light chain kinase peptide (M13) (**Figure 6** (Akerboom et al. 2009). In the absence of Ca++ ions, the GCaMP is poorly fluorescent due to a protonation of the chromophore and poor absorbance of the excitation wavelengths. Calcium binding to CaM results in a structural change that allows M13 to interact with CaM and ultimately leads to green fluorescence in GFP thanks to rapid de-protonation of the chromophore. GCaMP5 is a newer variant over GCaMP3 and other previous variants with a higher normalized intensity (F/F_o) and signal-to-noise ratio while they both have a fluorescence half-decay time of approximately 500 ± 430 ms (Akerboom et al. 2012). Cre recombinase expression of GCaMP5G and tdTomato in these mice allows for identification of GCaMP5G-

expressing cells and normalization of the green signal. These two fluorescent proteins are inserted in an intergenic region downstream of the endogenous Polr2a gene with the CAG promoter (**Figure 7**) (Gee et al. 2014). The GCaMP5G protein fusion allows *in vitro* and *in vivo* neuroscience and myeloid leukocyte research and more specifically enables us to test for Gαi-PCRS and ion channel agonists and antagonists (Pham et al. 2020).
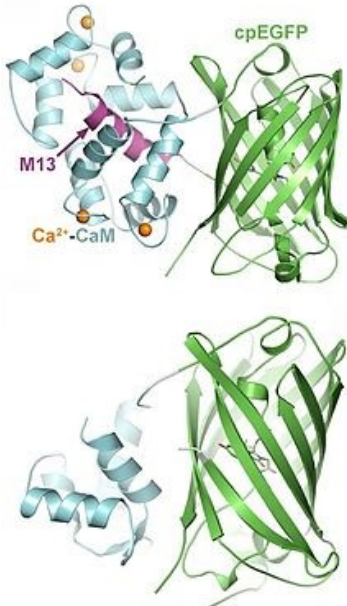
Figure 6: Crystal structure of the GCaMP protein fusion

Quaternary structure of the Ca^{++}-saturated GCaMP monomer depicting where Ca++ binds M13 and CaM (helices) and EGFP (ribbons) is positioned.

(Adapted from (Akerboom et al. 2009))
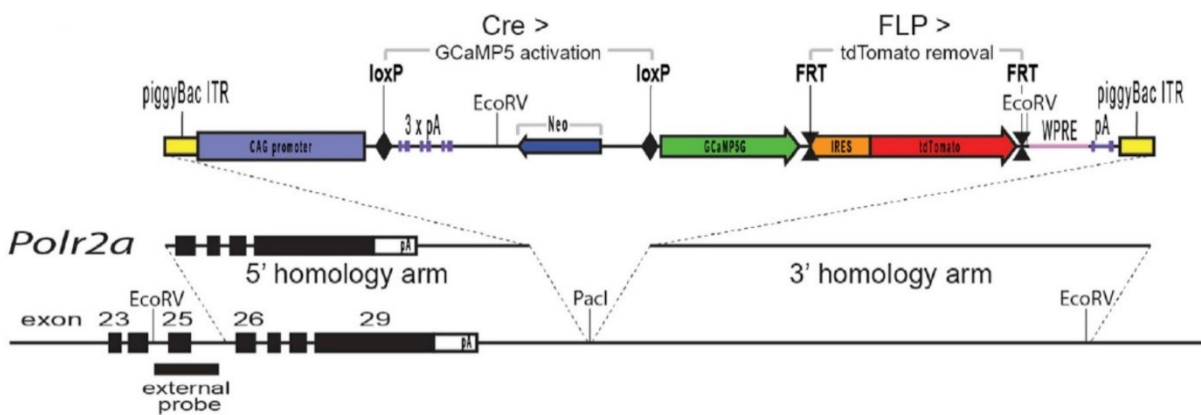
Figure 7: Genetic construct of the PC-G5-tdT allele

The 5' and 3' homology arms of the targeting vector are depicted in relation to the endogenous *Polr2a* gene. The reporter component of the targeting vector is displayed on top. Following Cre-mediated removal of the STOP (3x pA) cassette, the CAG promoter initiates constitutive IRES-tdTomato and GCaMP5G expression. WPRE, Woodchuck hepatitis posttranscriptional regulatory element; pA, polyadenylation signal; ITR, inverted repeats.

(Adapted from (Gee et al. 2014) with the kind permission of Elsevier)

1.7 Research objective

Inflammation is the main underlying cause of diseases that are the leading causes of death in the world. Coronary artery disease (Weber and Noels 2011), cardiovascular diseases (Gistera and Hansson 2017), stroke (Khoshnam et al. 2017), sepsis from infection

(Napolitano 2018) and cancer (Lucas, Barnich, and Nguyen 2017) are a few of those diseases. Most of what we know around immune cell interactions during inflammation stem from *in vitro* experiments, which are only a modest approximation of the real situation *in vivo*. Be it as it may, we have learned a lot from these experiments including that neutrophils interact with TMs in inflammatory settings to bring about homeostasis although some details are still lacking. It is the primary objective of this dissertation to uncover some of these missing details by utilizing state-of-the-art intravital microscopy techniques coupled to transgenic techniques that allow us to measure inflammatory cellular activity *in vivo*. In these regards, the following points were examined more closely in this work:

1. Systematic *in vivo* analysis of Ca^{++} signals in myeloid leukocytes
2. Assessment of the effect of inhibiting Gαi-PCRs on leukocyte function and Ca^{++} signals *in vivo*
3. Characterization of *in vivo* Ca^{++} signals during neutrophil-macrophage interaction during sterile inflammation

In doing so, this dissertation introduces a novel way to analyze leukocyte activity *in vivo* via Ca^{++} signaling and thereby lays out a pipeline to investigate the involvement of various cellular mechanisms in inflammation that could possibly lead to the discovery of new druggable targets in many of today's leading causes of deaths.

2. Materials and methods

2.1 Animal lines

The following mouse strains were used for the preparation of this dissertation:

- C57Bl6/6J
- CX3CR1eGFP ki/wt and ki/ki
- LysM-eGFP ki/wt
- PC-G5-tdTflox (fl/fl) x LysMcre (cre/+)
- PC-G5-tdTflox (fl/fl) x CX3CR1cre (cre/+)

2.1.1 C57Bl6/6J

The wild type strain C57BL/6J (Black 6) is the gold standard in the field of biomedicine and genetic background of many transgenic lines, including all the ones listed below (Ahlgren and Voikar 2019). We purchased Black 6 mice from Charles River. In experiments carried out for this dissertation, this wild-type strain was used in the creation of bone marrow chimeras as recipient.

2.1.2 CX3CR1eGFP

The chemokine fractalkine (FKN, Neuroactin or CX3CL1) binds to a specific transmembrane receptor (fractalkine receptor, CX3CR1) that becomes expressed on neurons upon activation of the endothelium. Because fractalkine has a role during adhesion and as a chemokine, the receptor presents a potential target for therapeutic interventions in sterile inflammation. Cells endogenously containing the CX3CR1-locus like monocytes and microglia are knocked-in with the enhanced green fluorescent protein (eGFP) gene making it possible to identify them. This enables expression of the fractalkine receptor in heterozygous animals in monocytes where as it is not expressed in homozygous animals. Because monocytes differentiate into M1 TMs once in the tissue microenvironment, this allows the identification of TMs in the murine skin model and the CX3CR1-CX3CL1 axis (Jung et al. 2000). Furthermore, it allows for trafficking studies including their interactions with other immune cells such as neutrophils.

2.1.3 LysM-eGFP

In order to use visualize myeloid cells in intravital microscopy, myeloid cells are marked in this mouse strain with the green fluorescent protein (GFP) by genetic manipulation. By doing this, it is possible to study progenitor cells in which myelomonocytic cells are labeled with GFP. This is achieved by knocking-in the gene for the eGFP at the murine lysozyme M (LysM) locus. Research shows that out of granulocytes, neutrophils have the highest fluorescence intensity. The animals show normal vitality and fertility. In the experiments shown here, heterozygous animals are used (Faust et al. 2000).

2. Materials and methods

2.1.4 PC-G5-tdTflox x LysMcre and PC-G5-tdTflox x CX3CR1cre

Also known as PC-G5-tdT, the Polr2a$^{Tn(pb-CAG-GCaMP5g,-tdTomato)Tvrd}$ is bred on a Black 6 background to express td tomato constitutively and GFP in dependence to the amount of Ca^{++} ions in the specific cell types where it is inserted. The Cre/loxP system facilitates this genetic insertion through the enzyme Cre recombinase and the two loxP sites flanking the GCaMP5G gene (**Figure 7**). In this case, the PC-G5-tdT was crossed to LysMcre and CX3CR1cre mouse lines in our animal facility resulting in PC-G5-tdTflox x LysMcre and PC-G5-tdTflox x CX3CR1cre mice, respectively, creating mouse strains that allow the investigation of Ca^{++} signaling in myeloid cells (Shi et al. 2018).

2.2 Mouse genotyping

For intravital visualization, heterozygous CX3CR1eGFP$^{ki/wt}$ were used. B6;129S6-Polr2atm1(CAG-GCaMP5g-tdTomato)Tvrd/J (GCaMP5G-IRES-td-tomatofl/fl) were purchased from Jackson and crossbred in our animal facility with LysMCre or CX3Cr1Cre mice. Mice used in experiments were at ages of 8 – 14 weeks. We age- and sex-matched the treatment groups that were all on a C57BL/6 background. Genotyping analysis was carried out from an ear or tail tip biopsy that was incubated at 56°C for 12 hours in 250 µL tissue lysis buffer with proteinase k solution (0.2 mg/ml, Qiagen, Hilden, Germany) for tissue digestion (Qiagen, Hilden, Germany). DNA was finally was isolated according to the manufacturer's directions with a QIAxtractor (Qiagen, Hilden, Germany).

Table 2: PCR reagent mixes for CX3CR1eGFP and GCaMP5G-IRES-TdTomato mouse strains

Reaction component	Stock Concentration	Run 1X
H$_2$O, PCR grade		6.25 µL
KAPA2G Fast Hot start Mix (contains 1.5mM MgCl$_2$)	2X	12.5 µL
Primer 1	10µM	1.25 µL
Primer 2	10µM	1.25 µL
Primer 3	10µM	1.25 µL
MgCl$_2$ (Taq DNA Polymerase Kit, Qiagen)	25mM	0.5 µL
Genomic DNA		2.0 µL
	Total	25.0 µL

2. Materials and methods

Table 3: PCR reagent mixes for the LysM-Cre mouse strain

Reaction component	Stock Concentration	Run 1X
H$_2$O, PCR grade		17.2 µL
PCR buffer	10X	2.5 µL
dNTPs	10mM	0.5 µL
Primer 2	10µM	1.25 µL
Primer 3	10µM	1.25 µL
Perfect match	1U/µL	0.06 µL
Taq	5U/µL	0.24 µL
Genomic DNA		2.0 µL
	Total	25.0 µL

Table 4: PCR reagent mixes for the CX3CR1-Cre mouse strain

Reaction component	Stock Concentration	Run 1X
H$_2$O, PCR grade		17.2 µL
PCR buffer	10X	2.5 µL
dNTPs	10mM	0.5 µL
Primer 1	10µM	0.5 µL
Primer 2	10µM	0.5 µL
Primer 3	10µM	0.5 µL
Taq	5U/µL	0.3 µL
Genomic DNA		3.0 µL
	Total	25.0 µL

PCR reagent mixes were prepared containing the PCR reaction programs (**Tables 2 – 4**) and either mutant- or wildtype allele-detecting primer pairs (**Tables 5 – 8**) were implemented. Subsequently, PCR products were examined by gel electrophoresis using a QIAxcel Advanced System (Qiagen, Hilden, Germany) in accordance to the manufacturer's directions (**Figure 8**). For every set of biopsy samples, a reaction with mutant and wildtype material along with water was included as positive and negative controls.

Table 5: PCR primers used for CX3CR1eGFP

	Primer name	Primer sequence
1	14276	5' GTC TTC ACG TTC GGT CTG GT 3'
2	14277	5' CCC AGA CAC TCG TTG TCC TT 3'
3	14278	5' CTC CCC CTG AAC CTG AAA C 3'

2. Materials and methods

Table 6: PCR primers used for GCaMP5G-IRES-TdTomato

	Primer name	Primer sequence
1	14276	5' TAG ACA CAT GCC ACC AAA CC 3'
2	14277	5' TCT CTC CAG CAC CAT AAC TCC 3'
3	14278	5' GAT CGA TAA AAC ACA TGC GTC A 3'

Table 7: PCR primers used for LysM-Cre

	Primer name	Primer sequence
1	14276	5' CCC AGA AAT GCC AGA TTA CG 3'
2	14277	5' CTT GGG CTG CCA GAA TTT CTC 3'
3	14278	5' TTA CAG TCG GCC AGG CTG AC 3'

Table 8: PCR primers used for CX3CR1-Cre

	Primer name	Primer sequence
1	CX3 forward	5' CCT CTA AGA CTC ACG TGG ACC TG 3'
2	CX3 reverse	5' GAC TTC CGA GTT GCG GAG CAG 3'
3	CX3 spec	5' GCC GCC CAC GAC CGG CAA AC 3'
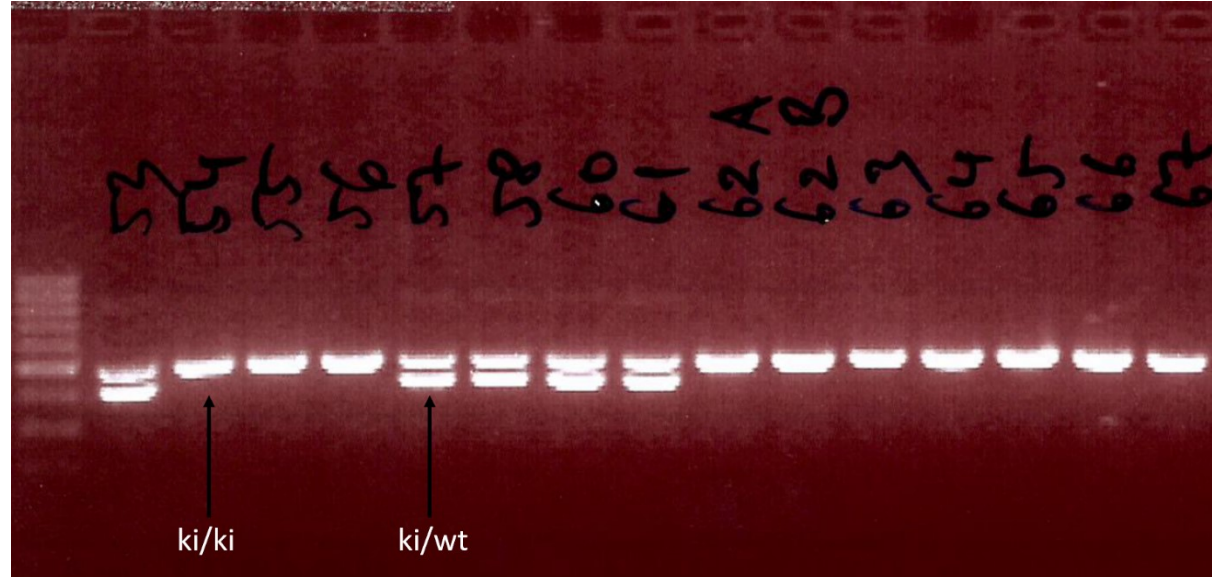
Figure 8: PCR genotyping gel

Representative genotyping of CX3CR1eGFP[ki/ki] and CX3CR1eGFP[ki/wt]. Homozygous ki/ki bands (600 bp) and heterozygous ki/wt bands (410 bp and 600 bp) were detected.

2.3 Surgical methods

2.3.1 *In vivo* imaging models

Cremaster muscle model

In the early 1960s, the cremaster muscle model was discovered in the rat as a viable model to study microcirculation in the live animal (Majno, Palade, and Schoefl 1961), (Grant 1964). In the early 1970s, (Baez 1973) made the jump to the mouse model and cemented it even more as the gold standard of microstructure research. The reasons for this are its thinness that allows high-resolution recordings, high vascularization with arterioles and venules, limited trauma caused by its externalization and the ease of its preparation (Glenn Merrill-Skoloff 2013). All of these combined and the possibility to inject inflammation causing substances make the cremaster muscle an ideal model to study microbial as well as sterile inflammation.

The cremaster muscle model was surgically prepared as (Baez) originally described it with minor modifications (**Figure 9**) (Baez 1973). Mice were put under narcosis with a mixture of midazolam (5 mg/kg body weight; Hameln), medetomidine (0.5 mg/kg body weight; Pfizer), and fentanyl (0.05mg/kg body weight; Albrecht) i.p. Labeled dyes were administered via tail vein catheter. The cremaster was inflamed 2 hours prior to surgery via intrascrotal injection of 50 µM fMLP (2 µl of 10mM stock solution diluted in 398 µl PBS). Imaging was performed on a scanning disc confocal microscopy (SDCM).
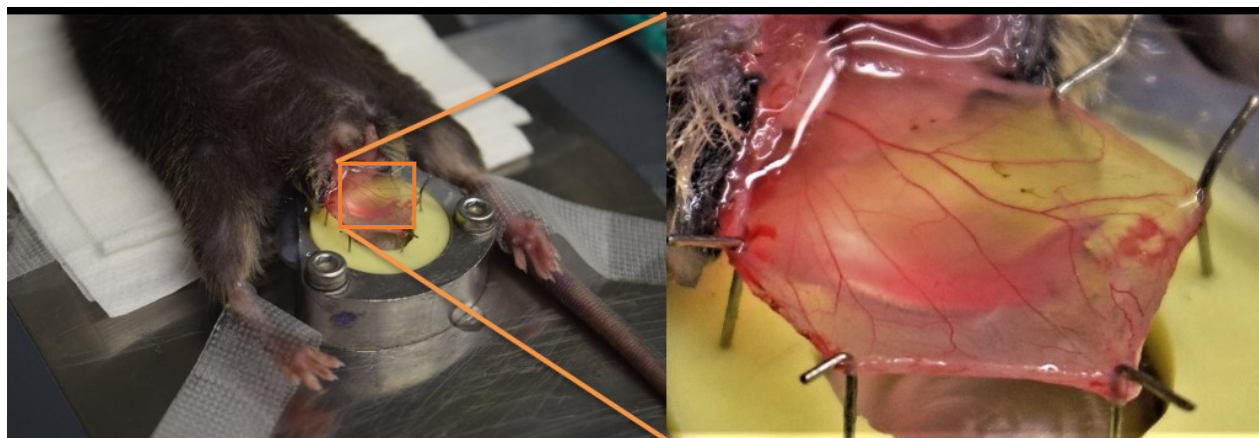
Figure 9: Murine cremaster muscle model

The cremaster muscle in the scrotum presents a good model for intravital imaging of leukocyte migration in part because of its high vascularization, and thin and transparent nature. After the mouse is fully under narcosis, an incision is made along the ventral surface of the scrotum. The cremaster muscle is then pulled out, pinned, stretched over the yellow pedestal and drenched in a physiological salt solution.

Ear skin model

The mouse ear is a proven model to study both microbial and sterile inflammation. A study by (Abdul Hamid et al. 2020) illustrates this model as valid for detecting and measuring inflammatory response elicited by biofilm and bacterial challenge as well as for the development of new preventive strategies (Abdul Hamid et al. 2020). Another study by (Chang et al. 2018) has shown the ear model to be well suited for studying inflammatory cytokine and

2. Materials and methods

chemokine release by macrophages and neutrophils in response to exposure to sulfur mustard, a potent agent known to induce sterile inflammation (Chang et al. 2018).

The structure of the murine ear pinna in combination with deep-reaching 2P-IVM is well suited for simulating sterile inflammation because it is made of two layers: the dermis and the epidermis (**Figure 10**). Only about 30 µm thick, the epidermis makes up the outer layer that is in direct contact to the outside and serves as the first line of protection against infectious agents. It is made up of rigid cells called keratinocytes made of a number of structural proteins giving it the integrity to serve as a barrier. The dermis on the other hand goes several hundreds of microns deeper and is where hair follicles, collagen fiber, blood vessels, nerve fibers and immune cells reside (Li et al. 2012). It is within the dermis where 2P-IVM experiments are set to study cellular interactions during laser-induced inflammation. It is this double-layered structure of the mouse ear pinna that makes it possible to model sterile inflammation; i.e. an inflammation that ensues while the epidermis barrier remains intact. Moreover, the dermis is highly vascularized insuring that a laser injury placed anywhere across the pinna elicits the desired inflammatory response (**Figure 11**) (Liu, Liang, and Wang 2020).
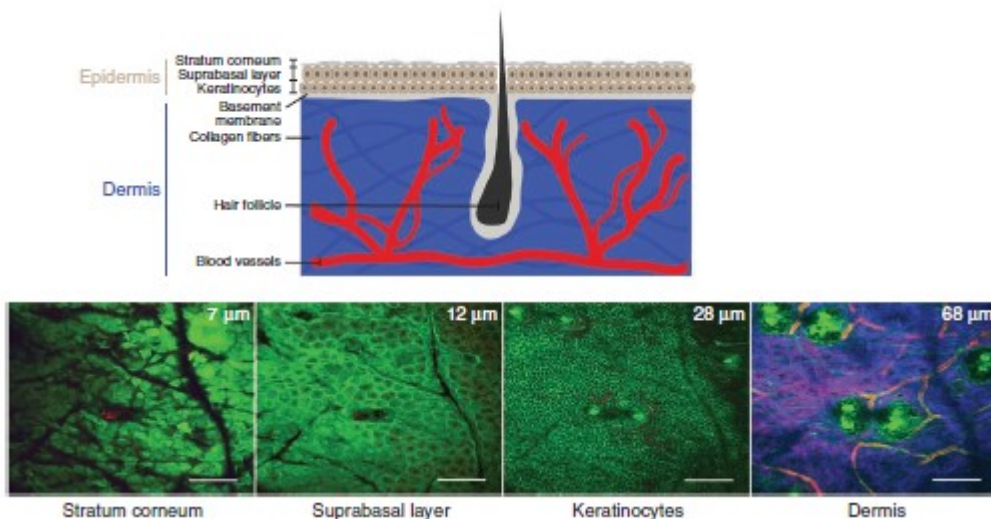
Figure 10: Structure and make-up of the murine ear

Top: A schematic depiction of the mouse skin showing the make-up of the epidermis and dermis. **Bottom**: 2P-IVM images of the ear skin at various vertical depths showing different cell types (green), collagen fibers (SHG, blue) and blood vessels (Evans blue, red). Scale bar, 100 µm

(adapted from (Li et al. 2012) with the kind permission of Springer Nature)

2. Materials and methods
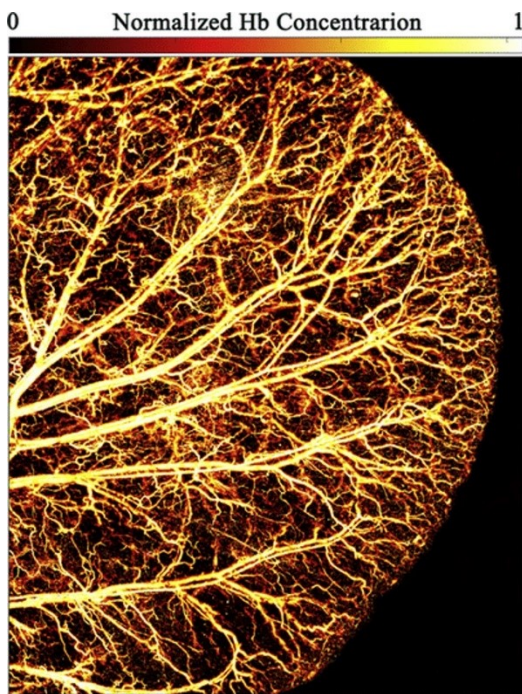
Figure 11: Vascularization of the mouse ear dermis

Normalized hemoglobin concentration of the blood imaged by functional optical-resolution photoacoustic microscopy shows the microvascular structure of the mouse ear.

(adapted from (Liu, Liang, and Wang 2020))

The mouse was sedated as described above. The ear was fixed on a custom-built-stage made of plexiglass base with a round raised stage of resin where the ear can be pinned down. The ear was pinned down at the fringes and stretched across the resin stage with several pins, with minimal folds across its surface (**Figure 12**). Following that BoxA (HMGbiotech http://hmgbiotech.eu/partners/), LFA1 antagonist (Bio X Cell), RAGE antagonist peptide (Tocris Bioscience), TLR4 inhibitor TAK-242 (Merck) or E.coli, each vs an isotype-matched control group or PBS, were injected intradermally into the ear and incubated for 30 minutes before starting the imaging process (**Table 9**). For macrophage depletion experiments, CX3CR1eGFP mice were switched to PLX5622 diet or control diet for 5 days and imaged on the 6th day (Acharya et al. 2016). Hair removal was not done in order not to elicit any inflammatory response. The skin was scanned for an optimal fold-free and hairless spot that was well vascularized and contained a good number of tissue-resident cells before placing a laser injury. Antagonizing antibodies were injected in the vicinity of laser injury with an insulin syringe almost parallel to the ear surface. Imaging was performed on a 2P-IVM.

2. Materials and methods
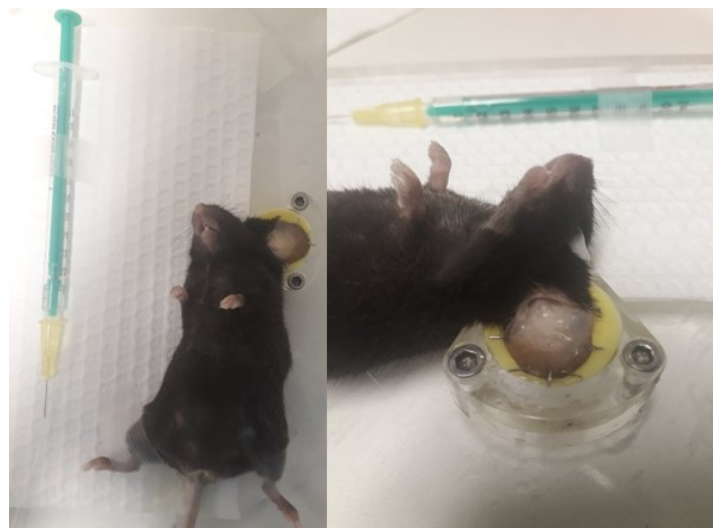
Figure 12: Ear skin model

After the mouse is fully under narcosis, the ear pinna is stretched over the yellow pedestal and pinned down so that there are minimal amounts of folds in the surface. Ultrasound gel is smeared on the surface for 2P-IVM.

Table 9: Treatment groups

Experiment group	Control (volume/concentration)	Treatment (volume/concentration)
HMGB1 inhibitor	Isotype antibody 10 µl / 8.3 µg/µl	BoxA 10 µl / 8.3 µg/µl
LFA-1 blocking antibody	Isotype antibody 10 µl / 9.25 µg/µl	LFA-1α (CD11a) 10 µl / 8.5 µg/µl
RAGE inhibitor	PBS (10 µl)	RAGE Antagonist Peptide 10 µl / 12.7 µg/ml
TLR-4 inhibitor	PBS (10 µl)	TLR4 inhibitor TAK-242 10 µl / 10 µg/ml
E. Coli	PBS (100 µl)	100 µl / $2.8 * 10^8$ CFU/ml

2.3.2 Chimera production

Cx3Cr1Cre-PCGtTflox in BL6

CX3Cr1Cre-PCGtTflox mice were rendered unconscious with isoflurane and then euthanized by cervical dislocation. The tibia, femur and tibiae were then removed, the flesh stripped off completely and placed in ice-cold PBS. They were then cut open on both sides and flushed with ice-cold PBS + 2% FCS on to a 70-µm strainer until the bone turned clear. Having passed the suspension through the strainer, it was centrifuged at 4°C and 300G for 7 minutes. Following that, it was discarded and the remaining pellet was resuspended in 5mL of Ery-Lysis buffer for 10 minutes. Following that, 30mL of PBS and 2mM EDTA were added to the suspension to stop the lysis reaction. The suspension was filtered once more with a 70-µm strainer and centrifuged at 4°C and 300G for 5 minutes. The supernatant was thrown away

and the remaining pellet resuspended in cold PBS. The suspension was then aliquoted into 250 µL per syringe for each recipient mouse. The cell count was 8 – 10 million per recipient mouse (**Figure 13a**).

Recipient Black 6 mice were placed on antibiotics one week prior to irradiation. On the day of irradiation, the mice were irradiated first 3 hours and once more 10 minutes prior to bone marrow cell suspension injection through the teil vein.

LysMCre-PCGtTflox in Cx3cr1eGFP

The same procedure was applied to make these chimeras as the one used to make the Cx3Cr1Cre-PCGtTflox in BL6 chimera **(Figure 13b)**.
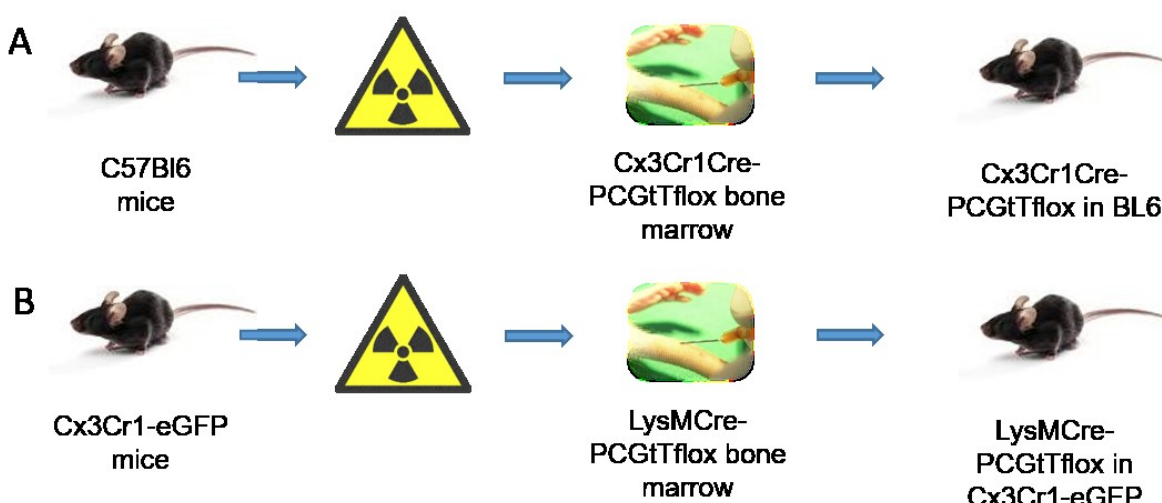
Figure 13: Chimera creation strategies for Cx3Cr1Cre-PCGtTflox in BL6 and LysMCre-PCGtTflox in CX3CR1eGFP

  A. Black 6 mice were first irradiated and received bone marrow cells i.v. from Cx3Cr1Cre-PCGtTflox mice generating 'Cx3Cr1Cre-PCGtTflox in Black 6' chimera.
  B. Cx3Cr1eGFP mice were first irradiated and received bone marrow cells i.v. from LysMCre-PCGtTflox generating and 'LysMCre-PCGtTflox in CX3CR1eGFP' mice.

2.3.3 Leukocyte adoptive transfer

Neutrophils were enriched from the bone marrow of a LysMcre-PC::G5-tdT reporter mouse. The mice were rendered unconscious with isoflurane and then euthanized by cervical dislocation. The tibia, femur and tibiae were then removed, the remaining tissue cleaned off using scalpels and placed in ice-cold PBS. They were then cut open on both sides and flushed with ice-cold 1*PBS + 2% FCS on to a 100-µm strainer until the bone turned clear. Having passed the suspension through the strainer, it was then centrifuged at 4°C and 300G for 5 minutes. The remaining pellet was resuspended in 1 mL PBS following which it was fractionated on a 52/64/72% Percoll gradient and the enriched neutrophil fraction was recovered at the interface of the 64% and 72% layers.

2. Materials and methods

Percoll gradient: 10% 10*PBS and 90% Percoll were mixed to make Isotonic Percoll solution. 52%, 64%, and 72% Percoll solutions were then prepared by mixing 5.2 mL isotonic Percoll with 2.8 mL PBS, 6.4 mL isotonic Percoll with 3.6 mL PBS, and 7.2 mL isotonic Percoll with 2.8 mL PBS, respectively.

The enriched neutrophil population was then divided into two, one half being stained in 20 µM CellTracker Blue CMAC Dye (control group) and the other in 10 µM Cell Proliferation Dye eFluor670 with 0.5 µg/ml Pertussis toxin (PTx) via incubation at 37°C for half an hour. The suspensions were subsequently washed once and resuspended in PBS. The two populations were then i.v. injected via the tail vein (in separate syringes in order to avoid unwanted staining of one or the other group by the wrong dye) into a Black 6 mouse whose cremaster muscle had already been inflamed (**Figure 14**).
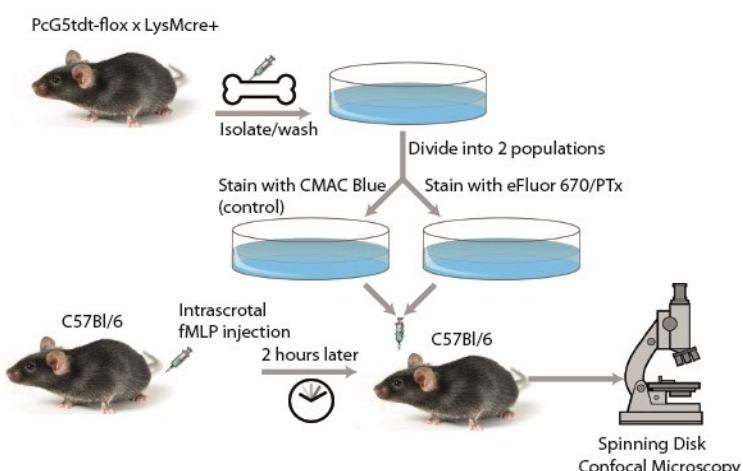
Figure 14: Neutrophil adoptive transfer

Experimental design of the adoptive transfer of control and PTx-treated neutrophils endogenously expressing Ca^{++} signal devised to analyze the role of G-protein coupled receptors during the neutrophil migration cascade.

2.3.4 Isolation of peritoneal macrophages

Sticky slide VI$^{0.4}$ Ibidi chambers were coated with Poly-L-Lys M (50 µg/ml) and incubated at 5.1% CO_2 and 37°C. *LysM^{Cre}-GCaMP5G-IRES-td-tomato$^{fl/fl}$* mice were anaesthetized by isoflurane inhalation and euthanized via cervical dislocation. A small patch of skin was carefully removed from the belly area, making sure the abdominal wall remains puncture-free. 5 – 10 ml of cold PBS were injected into the peritoneum. The abdomen was gently massaged on both sides to create a peritoneal macrophage suspension. The suspension was then slowly removed with the same cannula through the same hole that it was injected in and, after a centrifugation step, resuspended at $3*10^6$ cells/ml of RPMI 1640 + 10% FCS. 200 µl of this suspension were used to coat the Ibidi chambers and further incubated for 4 hours at the same conditions as before. Each slide was imaged for ten minutes. Before imaging, the chambers were flushed out with fresh RPMI solution to remove any non-attached cells. HMGB1 (2 µg/ml)

or PBS was added to the peritoneal macrophages. An automated inverted IX83 Olympus microscope with a UPlan 40×/1.0 or UPLSAPO-PH 100×/1.4 oil-immersion objective (Olympus) and a CCD camera (XM10, Olympus) was used to capture epifluorescence movies. The microscope was fitted with a humidified and heated stage incubator (Tokai Hit).

2.4 Microscopy

2.4.1 Epifluorescence Microscopy

Principle: Simple light microscopes can only use the 400 – 700 nm range, i.e. the visible spectrum, limiting them to contrast dyes that are only naturally visible. In contrast, epifluorescence microscopy enjoys the added functionality of shining whatever wavelength (340 to over 700 nm) excites fluorophores extending the range of visualizable cellular processes (Rudi Rottenfusser 1999). Cell samples on slides are illuminated by a beam of light that passes through them and ends up being captured by a camera. In general, epifluorescence microscopy suffers from signal loss through autofluorescence or background fluorescence falling outside of the focal plane (McAllister, Sisan, and Urbach 2008). Another disadvantage it suffers from is its lack of depth sectioning (Huang and Choma 2015).This can limit one's ability to deduce precise fluorescence localization or interpret 3D images.

Experiment protocol: An automated inverted IX83 Olympus microscope with a UPlan 40×/1.0 or UPLSAPO-PH 100×/1.4 oil-immersion objective (Olympus) and a CCD camera (XM10, Olympus) was used to capture epifluorescence movies. The microscope was fitted with a humidified and heated stage incubator (Tokai Hit).

2.4.2 Intravital microscopy

During intravital microscopy, mice were anesthetized and fully sedated before any surgical procedures began. Heating mats were used to keep the mice from cooling down during procedures while the microscope setups mentioned in section were fitted with heating chambers used to keep the mice warm during image acquisition. Mice were constantly checked for breathing irregularities and hind paw reflex and topped up with sedative when the reflex was positive. Intravital microscopy allows us to look at immune cells in their natural environment and serves as the best way to analyze their properties.

Spinning Disk Confocal Microscopy

Principle: SDCM uses the same principle as laser scanning confocal microscopy (LSCM) but builds on it by introducing a spinning disk full of pinholes as opposed to just one pinhole that eliminates out-of-focus light in LSCM (Stephens and Allan 2003). In LSCM, a single illumination volume scans the whole sample by zig-zagging across and back until the whole sample is acquired (Conchello and Lichtman 2005). This ends up in slow acquisition speeds especially for fast processes such as Ca++ signaling. In addition, LSCM suffers from low-resolution image acquisition and Airyscan processing improves this problem up to a certain level (Deroubaix,

2. Materials and methods

Moahla, and Penny 2020). In SDCM, the spinning disk allows for a precise illumination of the focal plane and imaging of multiple spots at the same time increasing the spatial and time resolution of live image acquisition over LSCM (McAllister, Sisan, and Urbach 2008). As a result, it results in diminished imaging duration and thereby less phototoxicity.

Experiment protocol: An upright spinning-disk confocal microscope (Examiner, Zeiss) with the confocal unit scanner CSU-X1 (Yokogawa Electric Corporation), 20× & 63×/1.0 NA water-immersion objectives (Zeiss), and a CCD camera (Evolve; Photometrics) and was used to perform imaging. Videos were recorded by four lasers with excitation wavelengths of 405 nm, 488 nm, 561 nm and 640 nm.

Two-photon excitation intravital microscopy

Principle: Two-photon excitation intravital microscopy (2P-IVM) uses the excitation of two photons at the same time from fluorophore-containing live tissue to half the energy level of a conventional one-photon excitation. Since a photon's energy is indirectly proportional to its wavelength, two photons would have approximately twice the wavelength of that of a photon in one-photon excitation. As a result, a fluorophore with an absorption at 420 nm under conventional excitation would be excited at 840 nm in two-photon microscopy (**Figure 15**). Due to the longer wavelengths utilized in two-photon microscopy, and consequently lower energy, one is able to image much deeper in live tissue than in confocal microscopy while reducing phototoxicity (Benninger and Piston 2013). But 2P-IVM suffers from worse temporal and spatial resolution compared to confocal microscopy techniques.
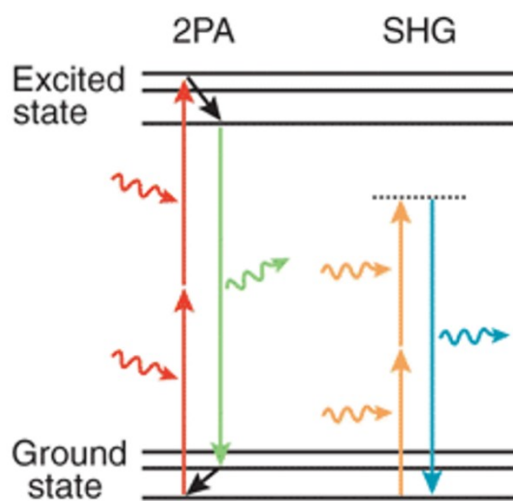
Figure 15: Jablonski diagram

Photons possess different energy states in a two-photon excitation system (2PA) and second harmonic generation (SHG) leading to specific emission wavelengths forming the basis for 2P-IVM.

(Adapted from (Helmchen and Denk 2005) with the kind permission of Springer Nature)

2. Materials and methods

With the 2P-IVM, a pulsed beam of IR laser light passes through a constellation of mirrors and raster scans the tissue through an objective with incremental vertical motion making individual stacks. This generates stacks of images, which are then put together into a 3D video and exported for demonstration purposes. With the videos, cell tracks are generated which lead to the analysis of different parameters and are then statistically evaluated (**Figure 16**) (Sumen et al. 2004).
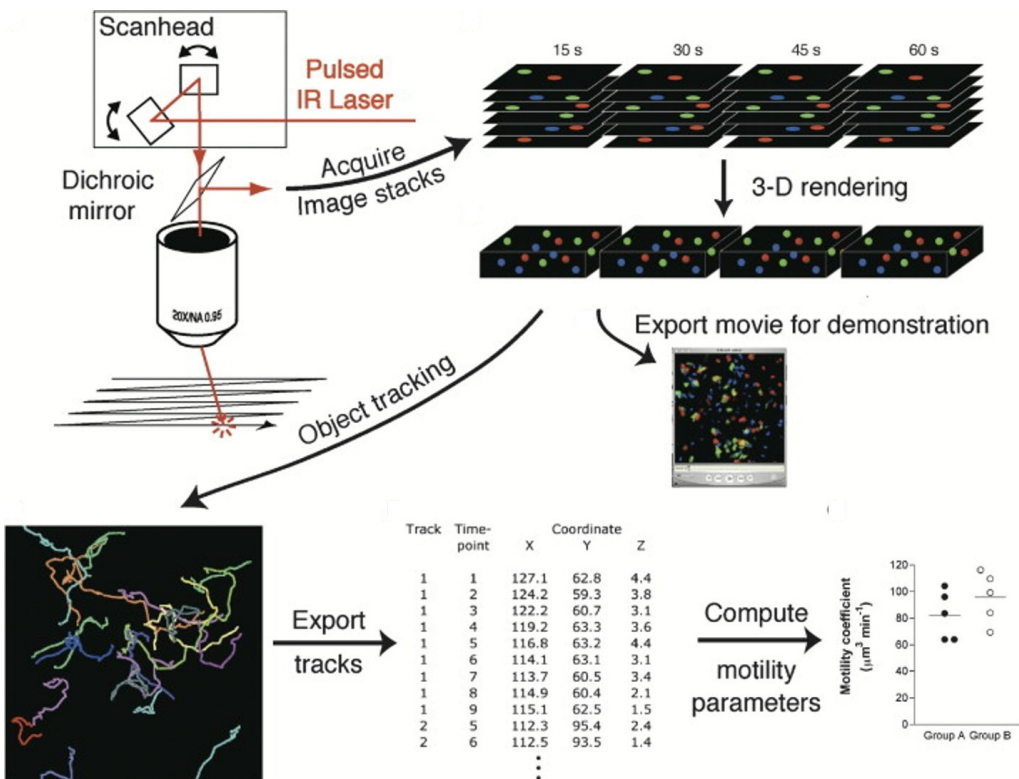
Figure 16: Steps of recording videos on the 2P-IVM to analyzing cell migration parameters

Pulsed IR laser is passed through the scanhead into the objective through which the sample is raster imaged. It is then reflected back through the objective onto a dichroic mirror that deflects it to a camera that acquires the image stacks. These stacks are then 3D-rendered in an imaging software and either exported as a movie or used for tracking and computing cellular migration parameters.

(adapted from (Sumen et al. 2004) with the kind permission of Elsevier)

Experiment protocol: A multiphoton TrimScope II system (LaVision BioTec) coupled with an upright Olympus microscope fitted with a 16× water immersion objective (NA 0.8; Nikon) and a Ti:Sa Chameleon Ultra II laser (690 to 1,040 nm; Coherent) was used to create a laser injury. Focusing the laser beam on a field of 42 µm × 42 µm until autofluorescence occured resulted in a single necrotic site, also called macrolesion. Imaging was performed with an excitation wavelength of 800 to 900 nm (depending of the fluorochromes) in an FoV frame of 559 µm × 559 µm with 515 × 515 pixels, at a frame rate of 2 per minute and a z-step of 3 µm in a range of 30 µm (approximately 20 – 50 µm underneath the epidermis). 3-D reconstruction,

2. Materials and methods

colocalization analysis, and acquisition of tracking parameters were made with Imaris (Bitplane).

Drift correction: The drift correction software Vivofollow (University of Bern) takes care of drift in the X, Y and Z dimensions by aligning every image (frame) to the previous one by using immobile markers. In this case, the software makes use of the second harmonic generation (SHG) produced by the collagen mesh in the skin to realign the frames, while in reality the tissue keeps drifting. The real drift in all 3 dimensions is caught and displayed on the frontend (**Figure 17**) (Vladymyrov et al. 2016).
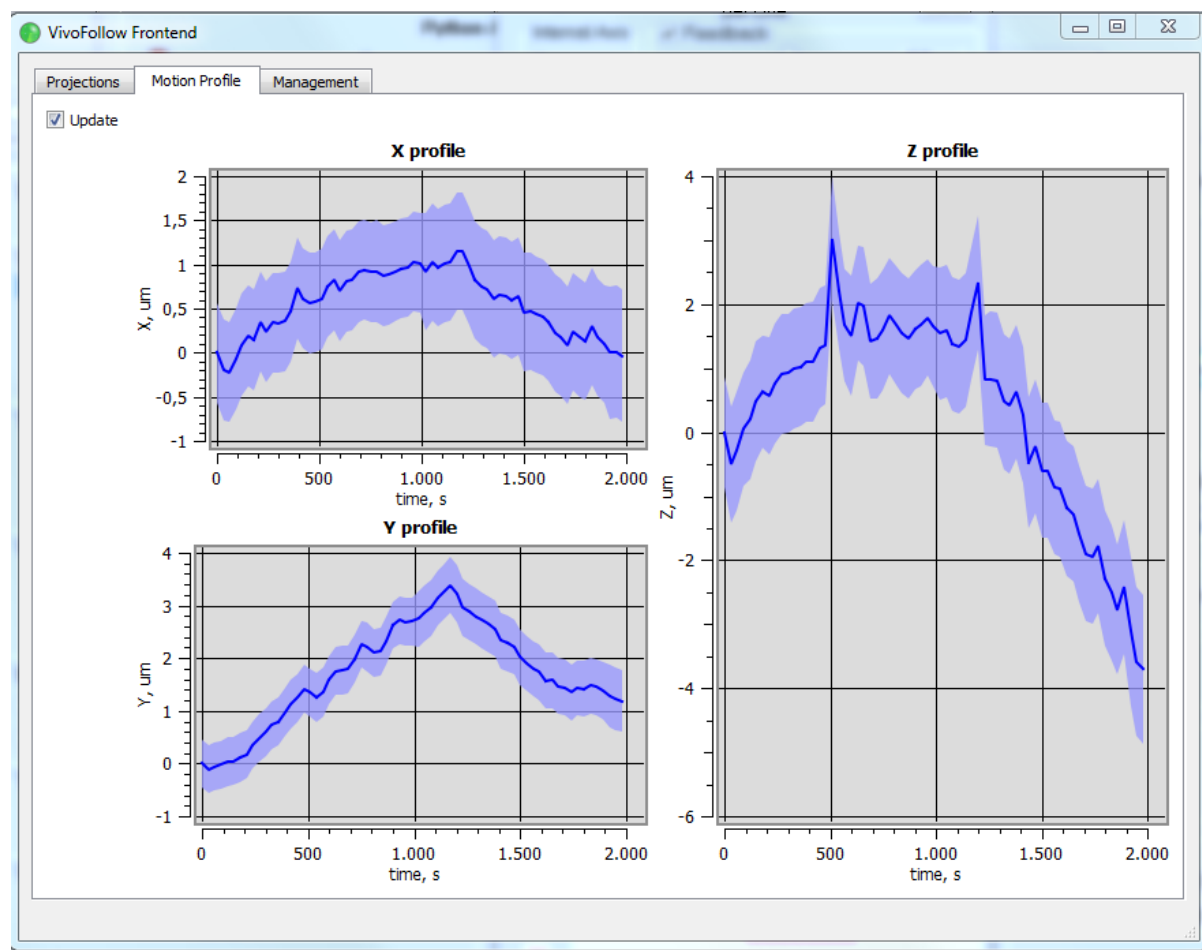
Figure 17: Vivofollow frontend displaying 3-dimensional dirfts.

Imaging without the Vivofollow software would result in drifts in the X, Y and Z dimensions. These potential drifts are corrected by the software and displayed as X, Y and Z-profiles over the imaging time.

2.5 E. coli cultivation

For microbial infection experiments, we used a frozen stock of E. coli (strain DH12) and inoculated it overnight in LB-broth medium (LB Broth (Luria lowsalt) Powder microbial growth medium, Sigma Aldrich, Steinheim) with 100µM Ampicillin (1:1000 Ampicillinsodiumsalt, Sigma Aldrich Chemie, Steinheim) and 1 mM IPTG (1:100 IPTG, Isopropyl β-D-1- 45

2. Materials and methods

thiogalactopyranoside; Sigma Aldrich Chemie, Steinheim) at 37°C and 260 rpm shaking. The CFU (Colony Forming Unit)/ml was established for OD600 = 1.0 with 3.2*10^8 CFU/ml. A starter culture of the overnight saturated culture was prepared the following morning in a 1:1000 dilution with LB-broth medium (1:1000), 100µM Ampicillin (1:1000), and 1 mM IPTG (1:100) and further incubated at 37 °C and 250 rpm for 2.5 hours to facilitate growth to early log phase. Afterwards, OD600 (reading of 0.3-0.4) was recorded and the required volume adjusted to OD600 = 1.0 equaling 2.8*10^8 CFU/ml to obtain an injection volume of 100 µl per mouse with a concentration of 3.2*10^8 CFU. Bacteria were then washed twice with 0.9% NaCl solution (Braun, Melsungen) and set aside on ice until injection.

2.6 Semi-automated algorithm for analyzing Ca^{++} signals

Intravital microscopy videos were imported into Imaris (Bitplane) and myeloid leukocyte surfaces rendered and segmented to determine the mean fluorescent intensity of the whole surface of a cell. The automation process was executed with Matlab (R2017a). To begin with, a code was designed around the excel sheet output from Imaris in order to create another excel sheet with two columns, namely the detrended signal and time. The intermediate excel sheet was then filtered in Matlab to remove any detectable noise and finally peaks selected out of it (for codes see **Appendix**). The final sheet contains normalized intensity (F_{norm}), difference in normalized intensity (ΔF_{norm}), and amplitude. Moreover, the final output also consists of signals with labeled positive and negative peaks along time. Ca^{++} signals were converted from the time domain into the frequency domain with the help of the Matlab plugin SpectralAnalysis (Version 3.0) as described in (Uhlen 2004).

$$F_{norm} = \frac{\text{Green channel intensity}}{\text{Red channel intensity}} \tag{1}$$

$$\Delta F_{norm} = F_{norm}(t+1) - F_{norm}(t); \; t \text{ - time} \tag{2}$$

$$\text{Amplitude} = F_{norm_{ave}}{}^{pos} - F_{norm_{ave}}{}^{neg} \tag{3}$$

$$\text{Minimum Peak Prominence (MP)} = p * [\max(F_{norm}) - \min(F_{norm})]; \; p\text{-percentage} \tag{4}$$

$$\text{Highest Peak Amplitude (HPA)} = \max(F_{norm}) - \min(F_{norm}) \tag{5}$$

2.6.1 Ca^{++} signal analysis parameters

The filtered Ca^{++} signal is quantified by using several parameters. The first parameter for quantifying Ca^{++} signals is the normalized fluorescence intensity – F_{norm} – (eq. 1) which is the value of the Ca^{++} dependent GFP signal originating from the GCaMP5G construct divided by that of the constitutive tdTomato signal. The difference in normalized intensity between consecutive time points is referred to as ΔF_{norm} (eq. 2). Furthermore, we defined the difference between the averages of the normalized intensity of the positive and negative peaks as

amplitude, because the highly irregular nature of the Ca^{++} signal *in vivo* does not allow the application of equations used for regular (e.g. sine wave) signals (eq. 3).

2.6.2 Power spectral density

The normalized signal intensity is swapped from the time domain into the frequency domain by using the mathematical approach known as Fourier transformation. The benefits of using Fourier transformation to compute analyses of biological transients have been detailed in (Harris 1998). By doing so, one uncovers periodicity in the signals that provide more information about the regulatory behavior of the cells. The resulting graphical representation of this transformation is called the power spectrum and is quantified by PSD (**Figure 18**) (Uhlen 2004).
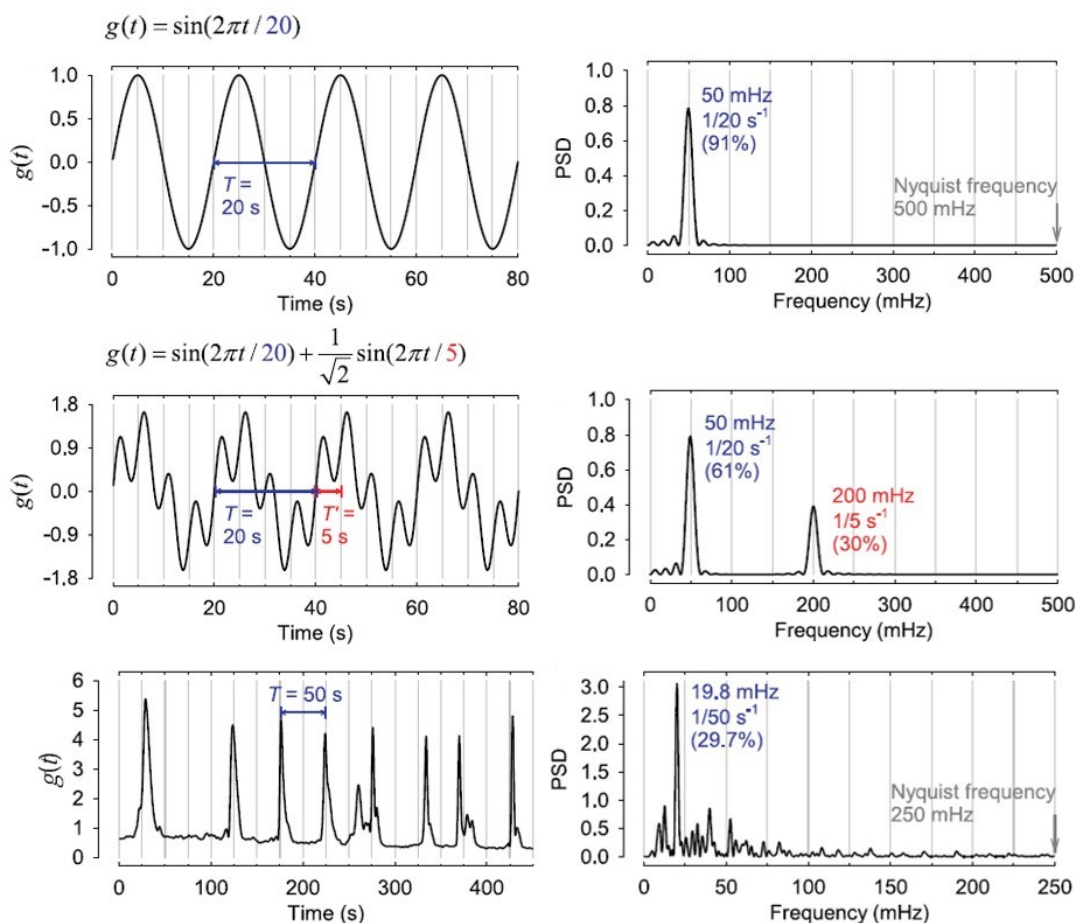
Figure 18: Distance-to-site-of-necrosis-dependent activation of myeloid leukocytes

A. **Left**: A simple sinusoidal curve with a period of 20 seconds in the time domain. **Right**: Frequency domain resulting from Fourier transformation of the sinusoidal curve.

B. **Left**: A superpositioning of two sinusoidal curves with periods of 5 and 20 seconds in the time domain. **Right**: Frequency domain resulting from Fourier transformation of the more complicated sinusoidal curve.

C. **Left**: Ca^{++} signal tracing of a regularly firing single-cell *in vitro* in the time domain. **Right**: Frequency domain resulting from Fourier transformation of the Ca^{++} signal tracing.

(adapted from (Uhlen 2004))

2.7 Quantitative imaging analysis.

2.7.1 Automated tracking

Videos of cells of interest originating from 2P-IVM, SDCM and epifluorescence microscopy were analyzed with Imaris automatically. The region of interest consisting of the cells to be analyzed is defined by a rectangular box (1). Following that, the shapes of the cells are best fitted using a threshold of the channel they are present in (2). Depending on the quality of the cells' voxels through the video, several tracks are created for every cell; i.e. the more visible a cell is throughout the video, the fewer tracks that will be created (3) (**Figure 19a**). Finally, corresponding partial tracks are connected to create full tracks from which track speed, meandering index, cell area/volume and many others can be extracted (4) (**Figure 19b**).
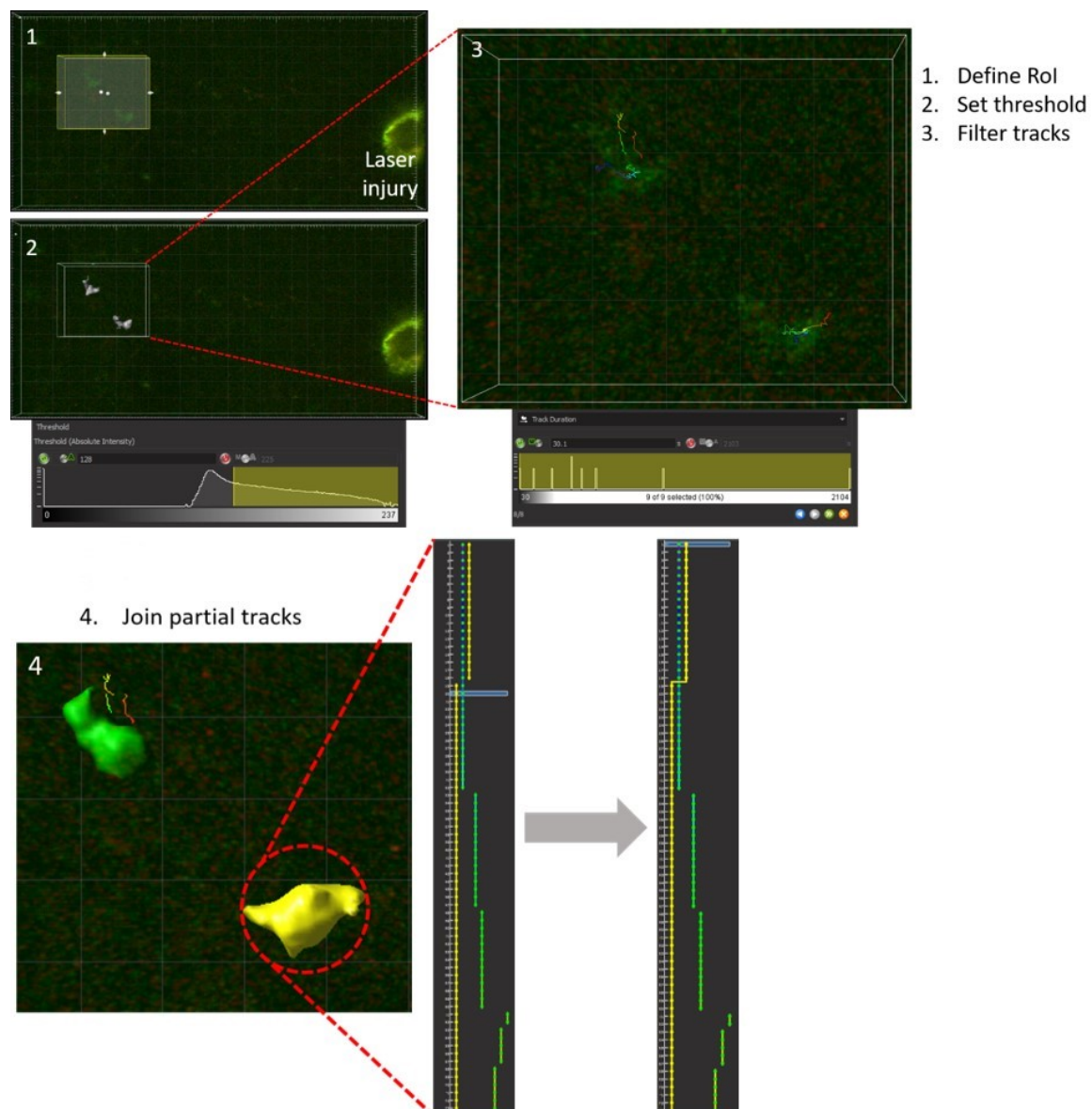
Figure 19: Automated tracking of cell migration in Imaris

- **A.** Steps of defining region of interest where cells are, setting threshold of surface rendering and filtering partial tracks
- **B.** Joining partial tracks to complete tracking

Once at the level of full tracks, mean intensity, speed, meandering index and time are exported into an 'Imaris output' excel file. The first of two Matlab codes (signal detrending) is then used to detrend the normalized signal leading to another excel file (intermediate sheet). From this point, there are 2 routes: SpectralAnalysis 3.0 renders PSD graphs while the second Matlab code (filter and peak finding) calculates amplitude (**Figure 20**).
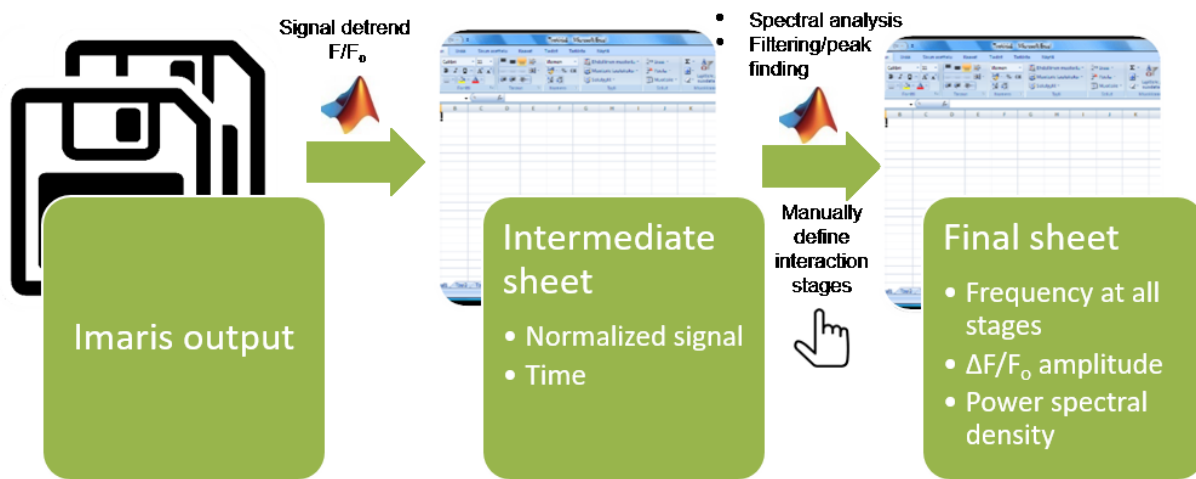
Figure 20: Semi-automated pipeline implemented for Ca^{++}-signal analysis

Ca^{++}-signal tracking output from Imaris in the form of excel files is signal detrended in Matlab and converted into the intermediate sheet consisting of normalized signal intensities and time values. The interaction stages, if applicable, are manually defined in this excel sheet and then further analyzed by one of two Matlab codes: 'Spectral Analysis' for frequency and power spectral density or 'Filtering/peak finding' for amplitude.

2.7.2 Target finding index

In order to define TFI, one needs to first classify the FoV into two main areas: A – a circular zone spanning 50 µm from the outer edge of the laser injury, and B – the remaining area farther out from the laser injury within the field of view (550 µm x 550 µm). In area A, neutrophils are considered to be in direct contact with the laser injury whereas in area B not. TFI is the number of neutrophils in A as a ratio of the number of neutrophils in B (**Figure 21**).

2. Materials and methods
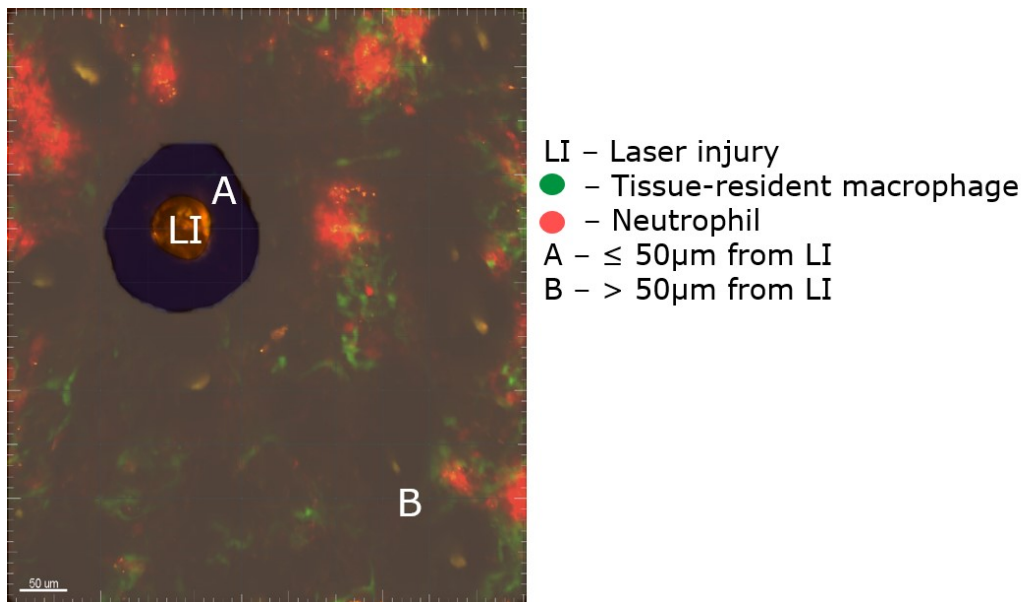
Figure 21: Field of view classification used to define TFI

Time projection of a video of the ear model of a CX3CR1eGFP mouse shows the TMs in green and neutrophils in red (Ly6G-PE). The circular area immediately around the laser injury (LI), defined as A, is considered where neutrophils are in contact with the tissue necrosis. Whereas the remaining area within the FoV, depicted as B, is considered where neutrophils are not in contact with the tissue necrosis. Therefore, the more neutrophils in A in proportion to B means an elevated target (tissue necrosis site) finding sense of neutrophils, and vice-versa. Scale bar, 50 μm

2.8 Software

Table 10: Software, versions and sources used to acquire and analyze cellular migration

Software	Version	Source	Purpose
Imaris	9.0.2	Bitplane	Cell tracking
Matlab	2017a	Mathworks	Ca^{++} signal analysis
ImageJ	1.8.0_172	NIH	Rolling cells visualization
Prism	7	GraphPad	Statistical analysis
Imspector Pro	5.0.275.0	LaVision BioTec	2P-IVM data acquisition
SlideBook	6	3i	SDCM data acquisition
CellSens	1.18	Olympus	Epifluorescence data acquisition
VivoFollow	1.0	University of Bern	2P-IVM drift correction

2.9 Statistics

Statistical analyses of the quantitative data in this dissertation were carried out with the software Graphpad Prism 7. Pair-wise comparisons were performed by use of the unpaired Students t-test and data shown depict means plus or minus standard error of the mean. Significance was determined by the value of the probability of error alpha (P) - *P < 0,05; **P <0,01; ***P < 0,001; ****P < 0,001.

3. Results

3.1 Intravital Ca⁺⁺ imaging in myeloid leukocytes with subcellular resolution using a transgenic Ca⁺⁺ reporter strain

To systematically determine Ca^{++} signals in myeloid leukocytes *in vivo,* we adopted a Ca^{++} reporter strain previously described for use in neurons. In these mice, intracellular Ca^{++} transients can be examined through the Ca^{++} indicator GCaMP5G giving a Ca^{++} binding dependent GFP signal with a temporal resolution in the range of milliseconds (Gee et al. 2014). This is coupled to constitutive tdTomato expression, allowing detection of cells independent from the dynamic Ca^{++} signal and normalization of the Ca^{++} signal.

To test the response of TMs from the peritoneum of *CX3CR1^{Cre}-GCaMP5G-IRES-td-tomato$^{fl/fl}$* mice to inflammation, these were treated by the prototypical DAMP HMGB1 as an activation stimulus. They showed Ca^{++} oscillations in response to this inflammatory stimulus, while they did not present such Ca^{++} oscillations in the absence of a stimulus (**Figure 22**).
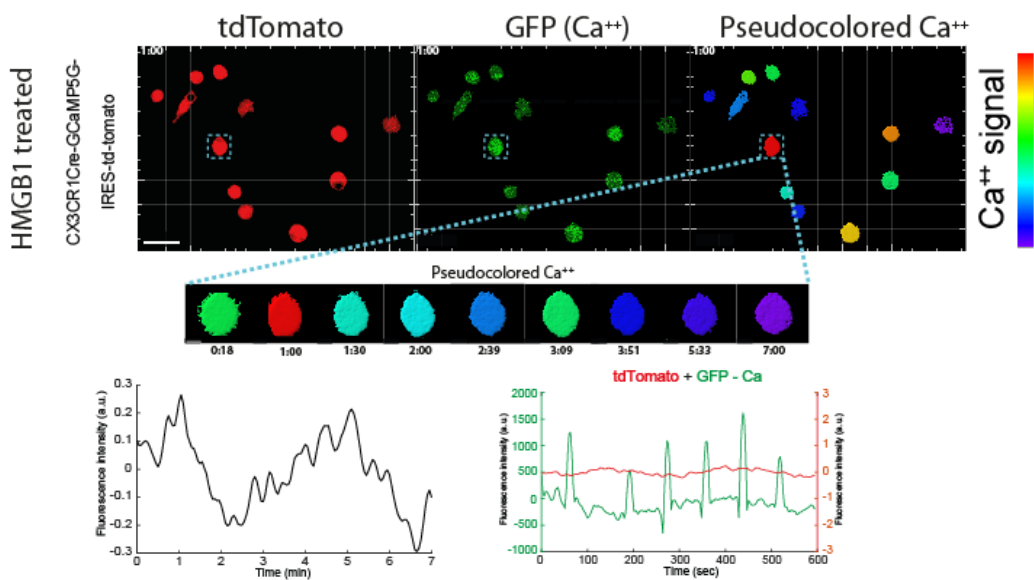
Figure 22: Macrophages' in vitro response to inflammatory cue via Ca⁺⁺

Top: Constitutive tdTomato signal and Ca^{++} signal in GFP and pseudocolor modes of peritoneal macrophages *in vitro* after HMGB1 treatment. Scale bar, 30 µm. Zoom-in: Time-lapse images of one cell's constitutive Ca^{++} signal in pseudocolor mode. Time is indicated as min:sec. **Bottom**: Mean fluorescence intensity-time plot tracings of the normalized Ca^{++} signal of the cell in zoom-in (left). Mean fluorescence intensity-time plot tracings of the Ca^{++} signal green and constitutive tdTomato red of the same cell. Time is indicated as sec (right).

To determine how immobile macrophages react to sterile inflammation *in vivo*, the ear model was used in *CX3CR1^{Cre}-GCaMP5G-IRES-td-tomato$^{fl/fl}$* mice in combination with 2-photon intravital microscopy. This allowed long term imaging with minimal bleaching and made it possible to capture Ca^{++} oscillations in TM. In response to a laser injury macrophages showed

a complex spectrum with highly variable frequency and amplitude, while they did not show such activity before laser injury (**Figure 23**).
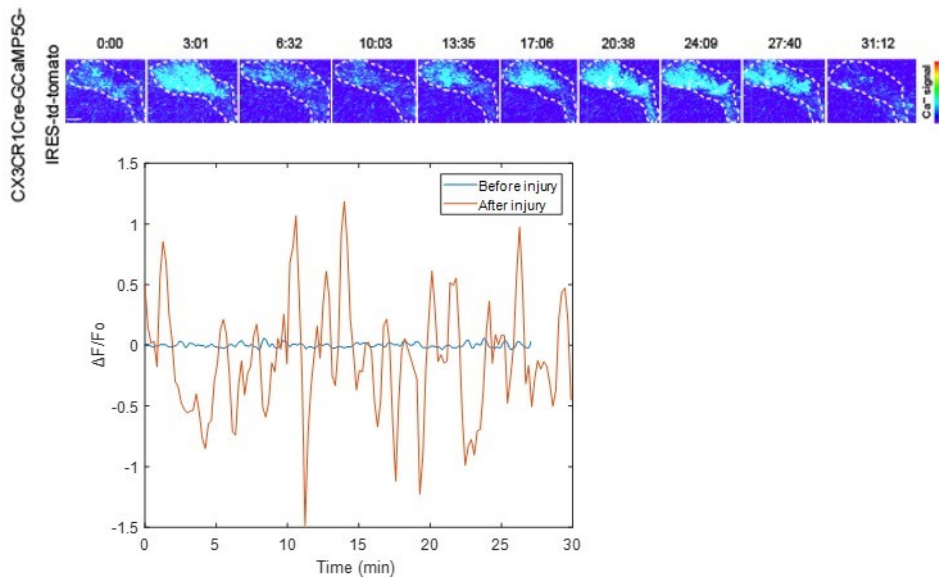
Figure 23: Macrophages' in vivo response to laser injury via Ca^{++}

Top: Representative time-lapse images of a TM showing intermittent surges in Ca^{++} signal (pseudocolor bar) after laser injury. Scale bar, 5 µm. Time is indicated as min:sec. **Bottom**: Mean fluorescence intensity-time plot of corresponding macrophage before and after injury.

Next, calcium signals in neutrophil were assessed to study Ca^{++} dynamics during the leukocyte migration cascade: LysMCre-GCaMP5G-IRES-td-tomatofl/fl mice were observed to display highly dynamic intracellular Ca^{++} oscillations during neutrophil rolling and adhesion using SDCM in the cremaster muscle model with a temporal resolution in the range of milliseconds. Neutrophils showed an intense Ca^{++} burst during the transition from rolling to adhesion on the endothelium, which was sustained when the neutrophils remained adherent. We also observed the constitutive tdTomato signal remained relatively flat as opposed to the highly dynamic Ca^{++}-GFP signal that is lined with peaks and troughs (**Figure 24**).
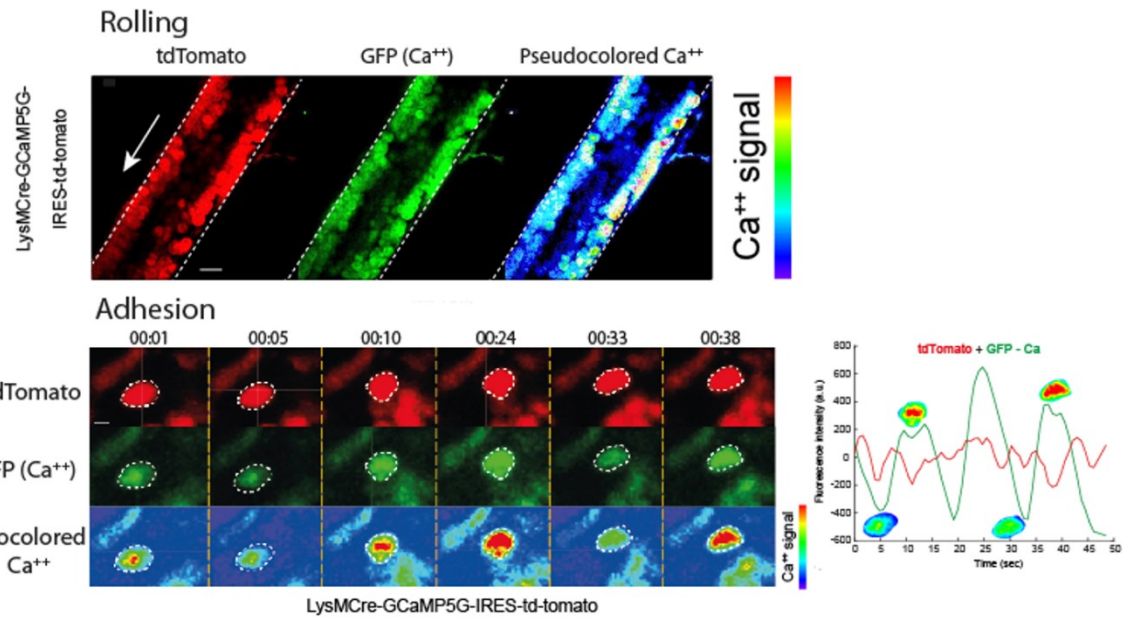
Figure 24: Neutrophils' intravital Ca⁺⁺ signal during rolling and adhesion

Top: Time projection of neutrophils rolling in vasculature (direction of flow depicted by arrow) depicted in constitutive tdtomato signal and Ca⁺⁺-signal in GFP and pseudocolor modes. Scale bar, 20 μm. **Bottom**: Time-lapse images of an adherent neutrophil's constitutive tdTomato signal and Ca⁺⁺-signal in GFP and pseudocolor modes. Scale bar, 5 μm. Time is indicated as min:sec (left). Mean fluorescence intensity-time plot tracings of the Ca⁺⁺-signal green and constitutive tdTomato red of the corresponding cell (right).

Following that, we looked at calcium activity depending on the distance to necrosis. We assessed spatiotemporal calcium activity in neutrophils in response to a laser injury using LysMCre-PC::G5-tdT mice *in vivo*. When they reached to zone of tissue necrosis, neutrophils stopped to migrate and the frequency of transients markedly increased, indicating a switch of calcium activity associated with execution of their effector functions and a gradient-dependent activity (**Figure 25**).
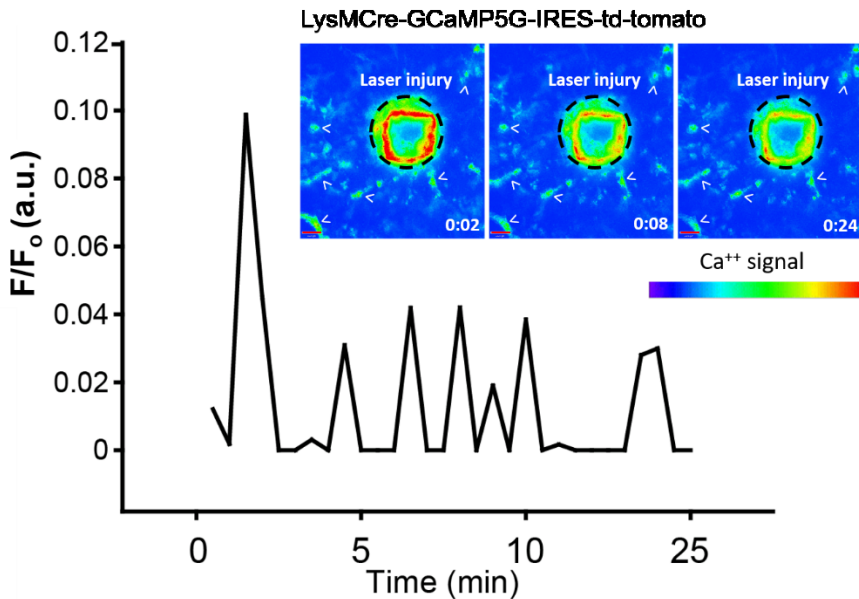
Figure 25: Neutrophil Ca⁺⁺ signal upon arrival at site of focal necrosis

Representative Ca^{++}-signal intensity tracing of neutrophils (marked with <) at the site of tissue necrosis (black dotted circle) in the ear model of a LysMCre-GCaMP5G-IRES-td-tomatofl/fl mouse shows peaks that are signs of cellular activity in response to tissue inflammation. Time is given as h:min Scale bar, 10 µm.

Taken together, the above *in vitro* and *in vivo* data of myeloid leukocytes show *that CX3CR1Cre-GCaMP5G-IRES-td-tomatofl/fl* and *LysMCre-GCaMP5G-IRES-td-tomatofl/fl* mice coupled with the specific experimental models allow assessment of Ca^{++} signals with high temporal and spatial resolution.

3.1.1 Ca⁺⁺ signal analysis algorithm

Intravital Ca^{++} signals are inherently prone to systematic shifts and noise. In order to uncover the true signals, they have to undergo a detrending process which ensures that any systematic shifts such as those caused by tissue drift and bleaching have no impacts on further analyses. Inherent peaks in the signal originating from Ca^{++} bursts will not be affected by the detrending process. Calcium signals are first smoothed through the Matlab built-in Savitzky-Golay filter (SGolayFilt) function. This is particularly useful in this case since it is being applied on F_{norm} values which are typically characterized by plenty of peaks and troughs, small and large alike. SGolayFilt is effective in smoothing Ca^{++} signals. Savitzky-Golay filtered signals are then detrended, which accentuates the peaks and centers the signal's mean to 0. A strict ruleset on how to select meaningful peaks and troughs is crucial so as to not detect noise as Ca^{++} peaks and to compare across the same detrending and filtering settings as much as possible. Hence, a ruleset consisting of SGolayFilt and Minimum Peak Prominence – MP (eq. 4) – a function that seeks out to eliminate unnecessarily small peaks and troughs that are smaller than a percentage of the Highest Peak Amplitude – HPA (eq. 5) – was put in place. The HPA is defined as the difference between the highest peak and the lowest trough. Therefore, a smaller

mp value means a highly unselective ruleset leading to less selective quantitative results. A point is considered a peak if at least on either of its sides there is a drop of more than 0.1*p to the previous/next sample point (**Figure 26**).
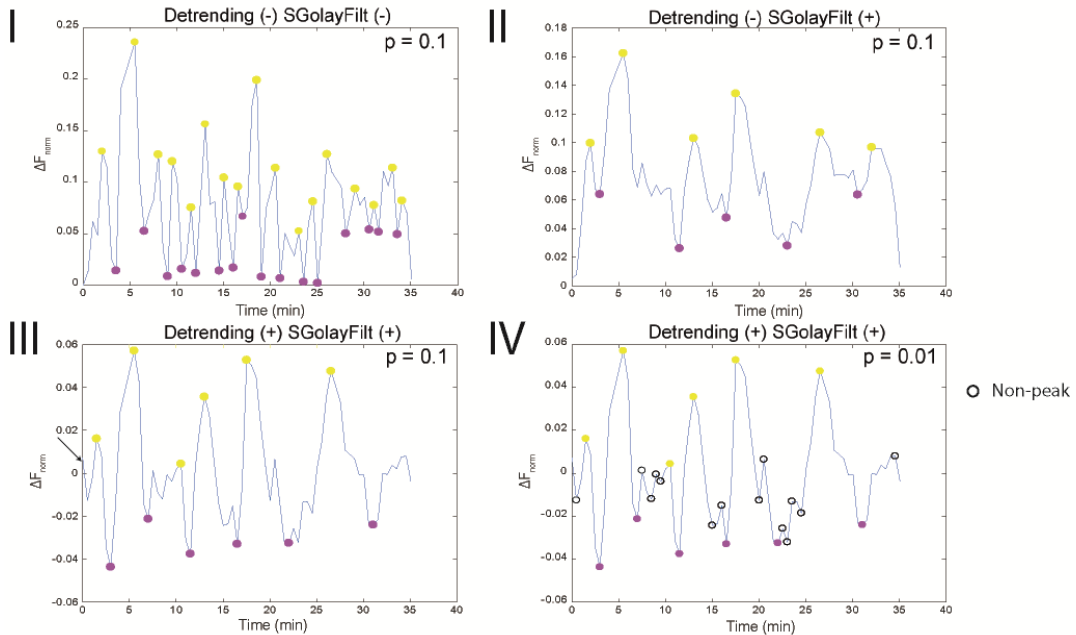
Figure 26: Ca⁺⁺ signal analysis *in vivo*

Representative mean fluorescence intensity-time plot of a TM going through systematic and successive steps of filtering and detrending (I – IV) uncovers oscillatory patterns.

In some instances, Ca⁺⁺ signals are characterized by bigger peaks followed by smaller peaks about half the size in amplitude of the bigger ones, in a repeating fashion. Keeping this distinctive feature in mind, it is easier to appreciate the effects of detrending and Savitzky-Golay filtering. Without detrending and Savitzky-Golay filtering, such features are not as distinguishable. In addition, these bigger peaks are flanked by satellite peaks that are smaller than 0.1*p and hence not labeled as peaks. This filtered Ca⁺⁺ signal is quantified by using several parameters. The first parameter for quantifying Ca⁺⁺ signals is the normalized fluorescence intensity – F_{norm} – (eq. 1) which is the value of the Ca⁺⁺ dependent GFP signal originating from the GCaMP5G construct divided by that of the constitutive tdTomato signal. The difference in normalized intensity between consecutive time points is referred to as ΔF_{norm} (eq. 2). Furthermore, we defined the difference between the averages of the normalized intensity of the positive and negative peaks as amplitude, because the highly irregular nature of the Ca⁺⁺ signal *in vivo* does not allow the application of equations used for regular (e.g. sine wave) signals (eq. 3) (**Figure 27**).

A

B

$$F_{norm} = \frac{Green\ channel\ intensity}{Red\ channel\ intensity} \qquad (1)$$

$$\Delta F_{norm} = F_{norm}(t+1) - F_{norm}(t);\ t\text{ - time} \qquad (2)$$

$$Amplitude = F_{norm_{ave}}^{pos} - F_{norm_{ave}}^{neg} \qquad (3)$$

$$Minimum\ Peak\ Prominence\ (MP) = p * [max(F_{norm}) - min(F_{norm})];\ \text{p-percentage} \qquad (4)$$
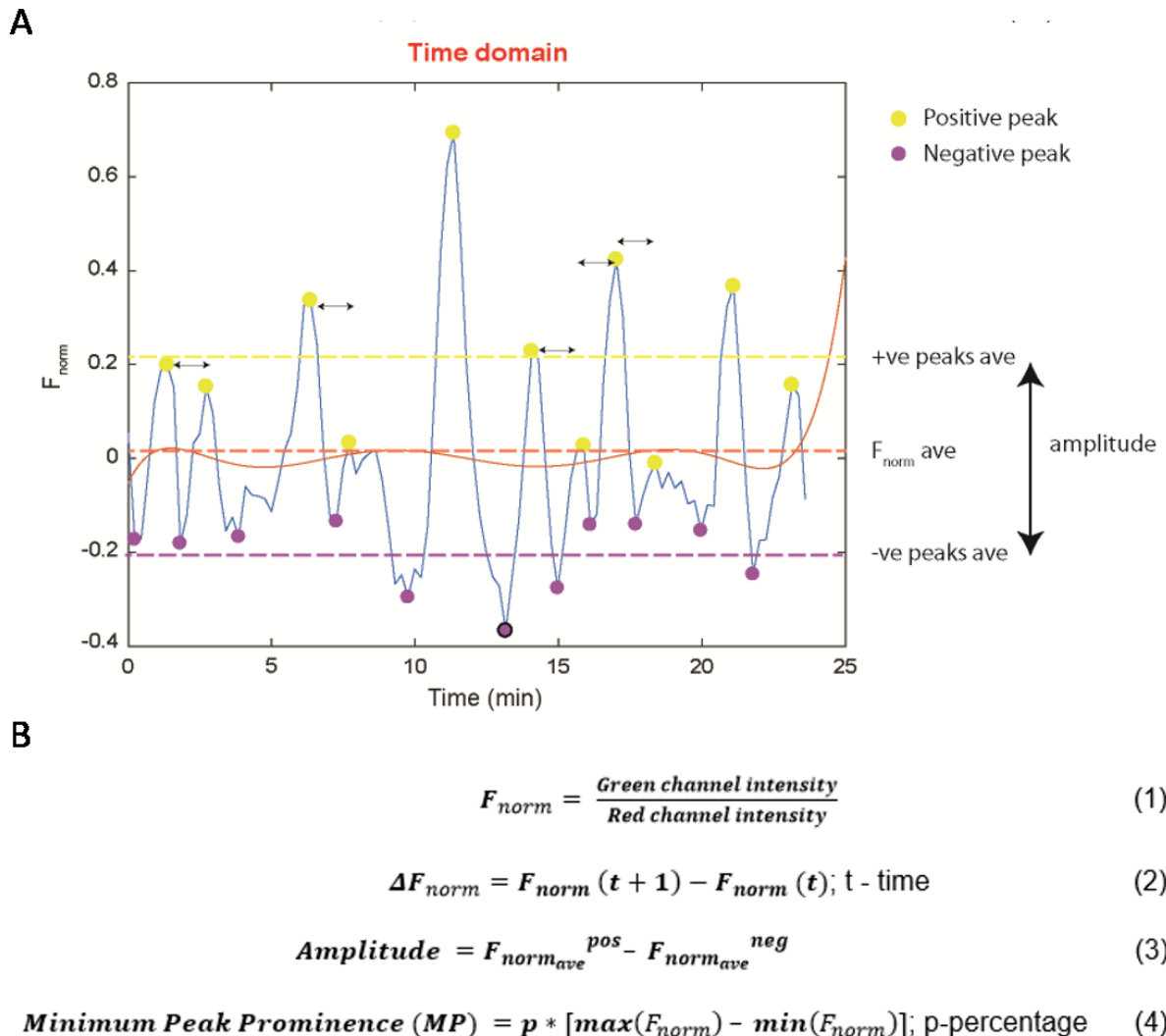
Figure 27: Ca++ signal basic parameters

A representative mean fluorescence intensity-time plot of a TM displaying the basic parameters used to characterize Ca++ signals in the time domain (A) and the mathematical formulas that define them (B).

Frequency in Ca++ oscillations is commonly depicted as the number of peaks in a specified amount of time, but this approach suffers from oversimplification and lack of information because Ca++ signals, like many other biological signals, are of highly irregular periodicity. To overcome these issues, the Ca++ signal is converted from the time domain to the frequency domain via Fourier transformation. The result is a display of all frequencies present in the signal arranged by their respective power (i.e. how often they were observed) called the PSD (also an indirect indicator of amplitude) giving a detailed picture of the ranges of frequency at which the Ca++ signals appear. This allows the identification of the overall frequency spectrum as well as the most dominant frequencies within the spectrum: This can be observed in **Figure 30** where the peak at 33.8 mHz is the most dominant frequency according to peak width, whereas the peak at 3.9 mHz would be most dominant as per peak height. Accordingly, the most dominant frequency 33.8 mHz corresponds roughly to half a minute of inter-peak spacing

(period) or 2 events per minute (**Figure 28**). Moreover, we can observe in this overall spectrum that frequency values are well spread across the 0 – 40 mHz range. In conclusion, a series of normalization, filtering, detrending and Fourier transformation steps of the Ca^{++} signal is required to characterize it. In addition, frequency spectra allow the analysis of complex *in vivo* Ca^{++} signals, which are characterized by quasiperiodicity.
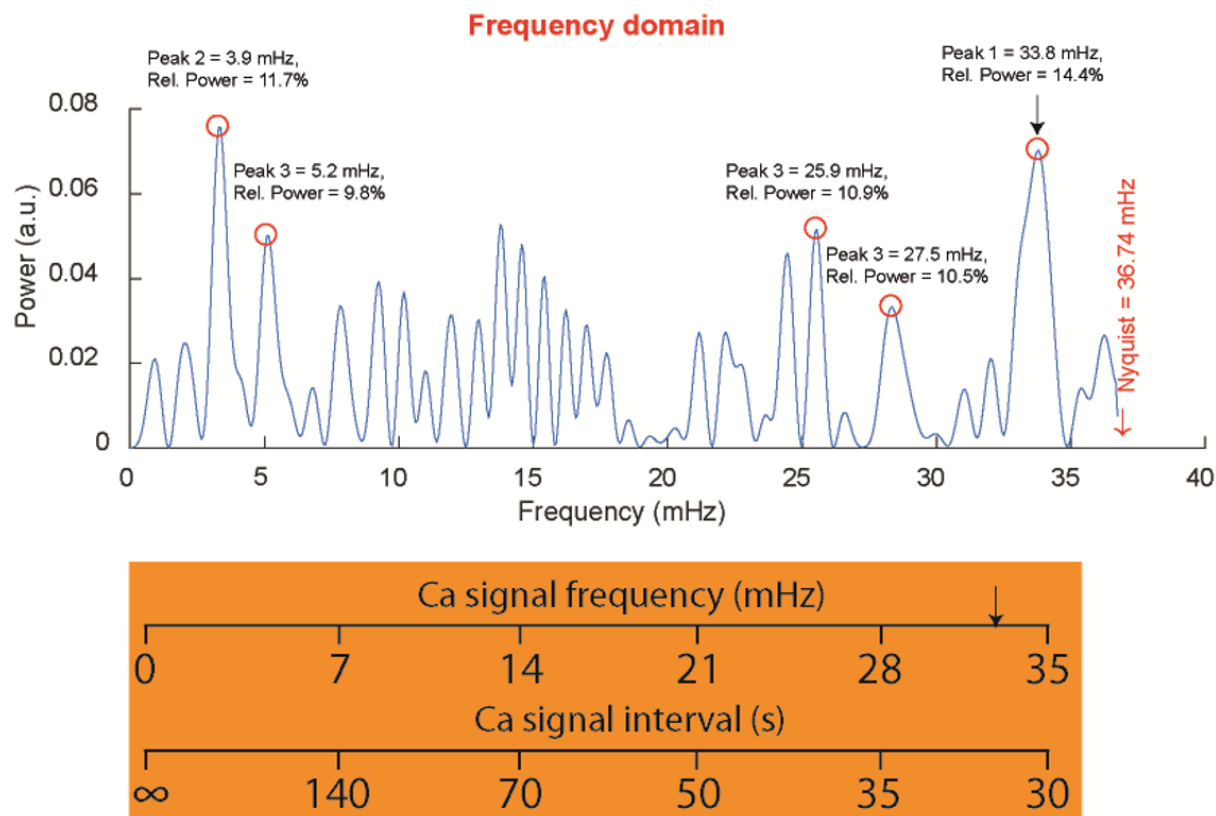
Figure 28: Fourier transformation from the time domain to frequency

Top: PSD of the plot in Figure 27a resulting from its Fourier transformation into the frequency domain displays the 5 most dominant frequencies (red circles) and the most dominant one from them (arrow). **Bottom**: A frequency-to-period conversion tool, with the black arrow corresponding to the most dominant frequency.

3.1.2 Spatiotemporal changes in Ca^{++}-activity of macrophages upon tissue injury

To assess if *in vivo* Ca^{++} imaging provides new insights into leukocyte activation, we examined the response of TMs to defined tissue necrosis caused by a laser injury. TMs are regarded as first responders to sterile inflammation, but this hypothesis is supported by sparse intravital evidence. When we assessed TMs in CX3CR1eGFP mice by intravital 2P-IVM after laser injury in the skin, we did not detect changes in morphology and the cells remained immotile over the first two hours not allowing us to deduce their state of activation (**Figure 29**).

To overcome these limits posed by intravital microscopy, we tested if and how intracellular changes in Ca^{++} signal can serve as a marker of macrophage activation by using our protocol with *CX3CR1^{Cre}-GCaMP5G-IRES-td-tomato^{fl/fl}* mice. During baseline conditions, CX3CR1$^+$ cells showed very low levels of Ca^{++} signals (**Figure 30**).
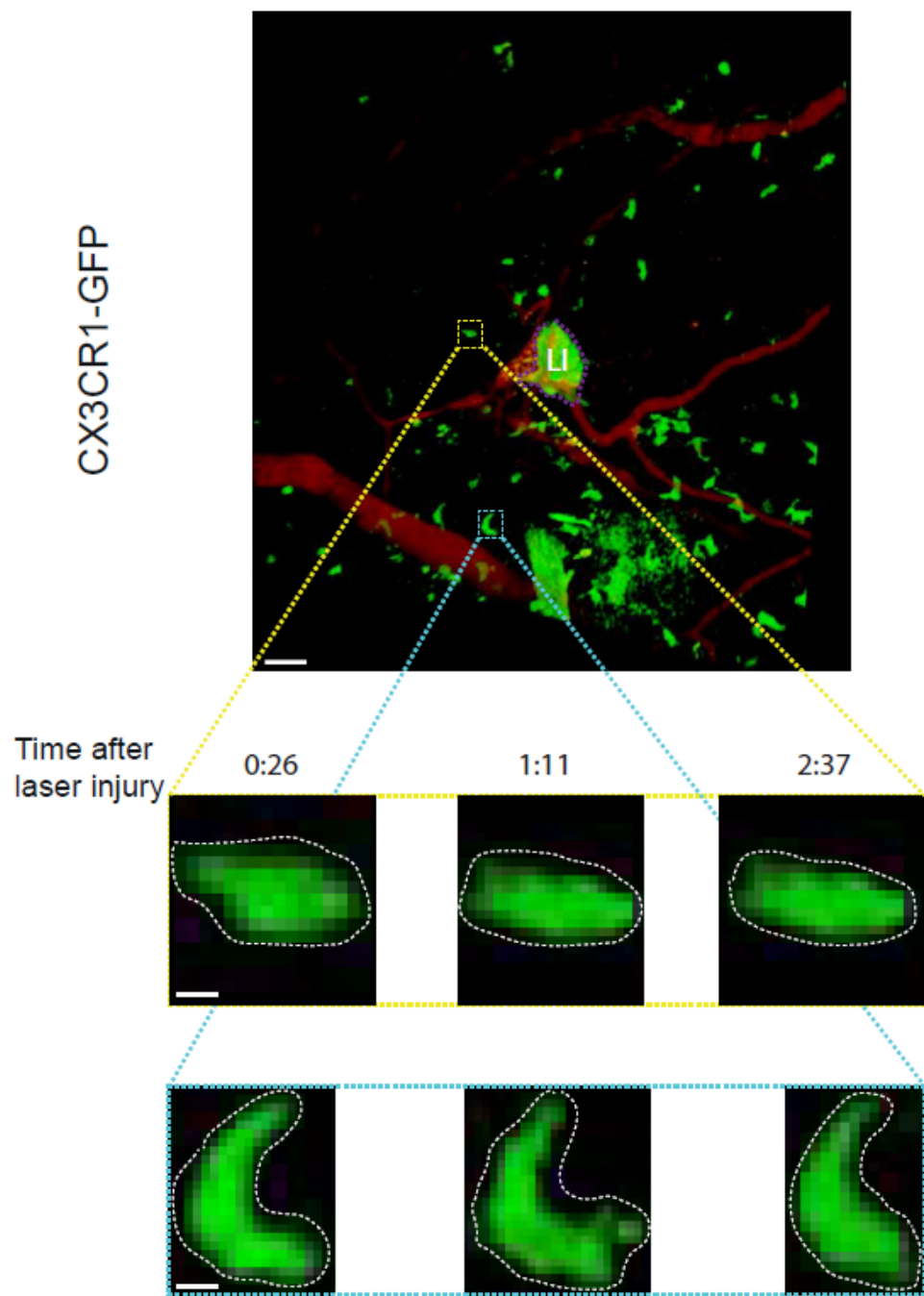
Figure 29: Tissue-resident macrophages

Time-lapse images from the ear model in a CX3CR1eGFP mouse of TMs showing no change in shape or position up to 2 hours after laser injury induction (LI, circular green patch outline by violet dotted line). Blood flow shown in red labeled i.v. by TRITC-dextran. Time is given as h:min Scale bar, 50 µm.

3. Results
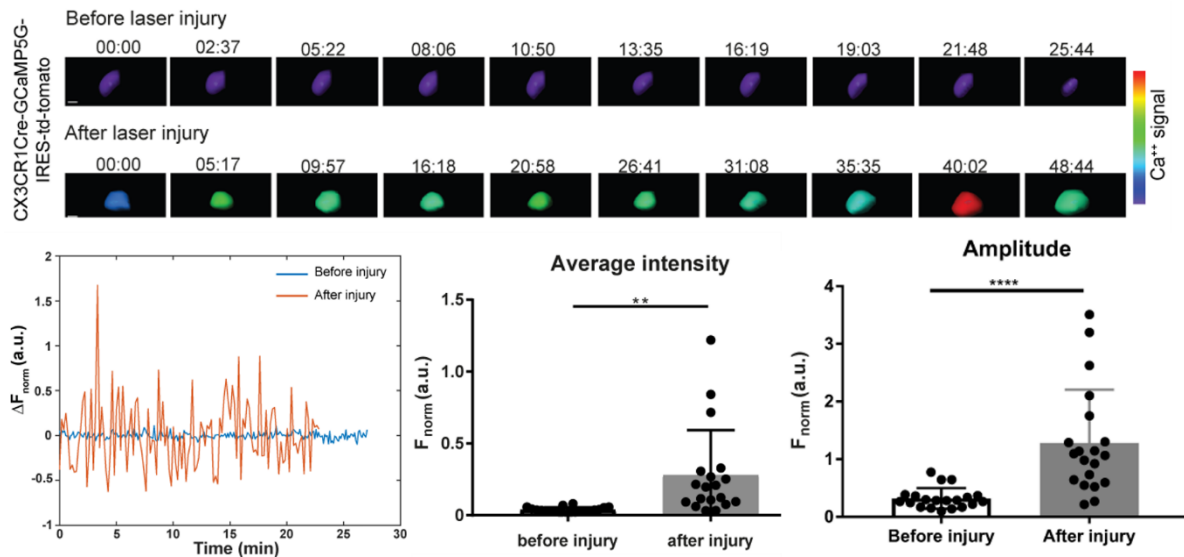
Figure 30: Activation of TMs by tissue necrosis

Top: Time-lapse images of a TM's Ca^{++} signal in pseudocolor mode before and after laser injury. Scale bar, 10 µm. Time is indicated as min:sec. **Bottom-left**: Mean fluorescence intensity-time plot tracings of the normalized Ca^{++} signal of the cell before and after laser injury. **Bottom-middle**: Ca^{++} signal amplitude of TMs before versus after laser injury. **Bottom-right**: Average mean fluorescence intensity of TMs before versus after laser injury. Unpaired t-test, **$P \leq 0.01$, ****$P \leq 0.0001$; n = 3/5 mice per group; means ± SEM.

This was altered drastically after induction of sterile inflammation by a laser injury following which most CX3CR1$^+$ macrophages showed significantly heightened intensity and amplitude values (**Figure 30**), frequent short Ca^{++} transients (< 2 min) and occasional long transients (> 2 min) of high amplitude and more diverse frequency values than the oscillations seen in unstimulated cells (**Figure 31, Figure 32**).
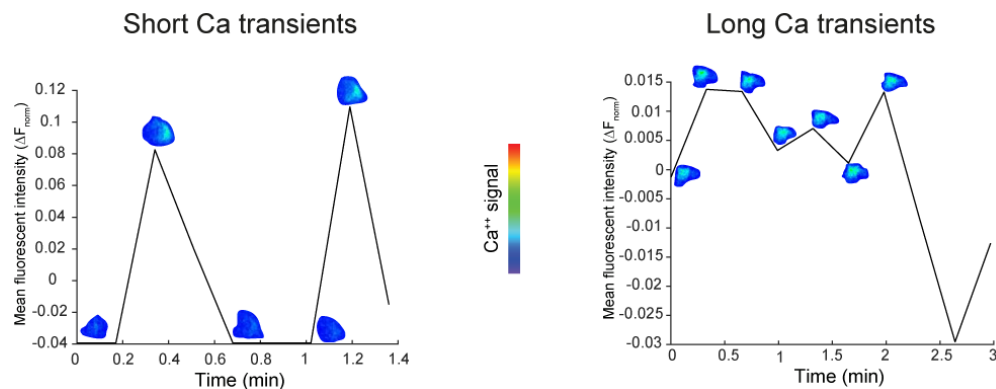
Figure 31: TMs' Ca^{++} transients

Left: Mean fluorescence intensity-time plot of a TM displaying short Ca^{++} transients. **Right**: Mean fluorescence intensity-time plot of a TM displaying long Ca^{++} transients; images of the cells' Ca^{++} signal in pseudocolor mode are transposed onto both plots.

3. Results

In summary, sterile inflammation by focal necrosis results in TM activation in surprisingly diverse manners as evidenced by increases in Ca^{++} intensity, amplitude, and frequency (**Figure 32**).
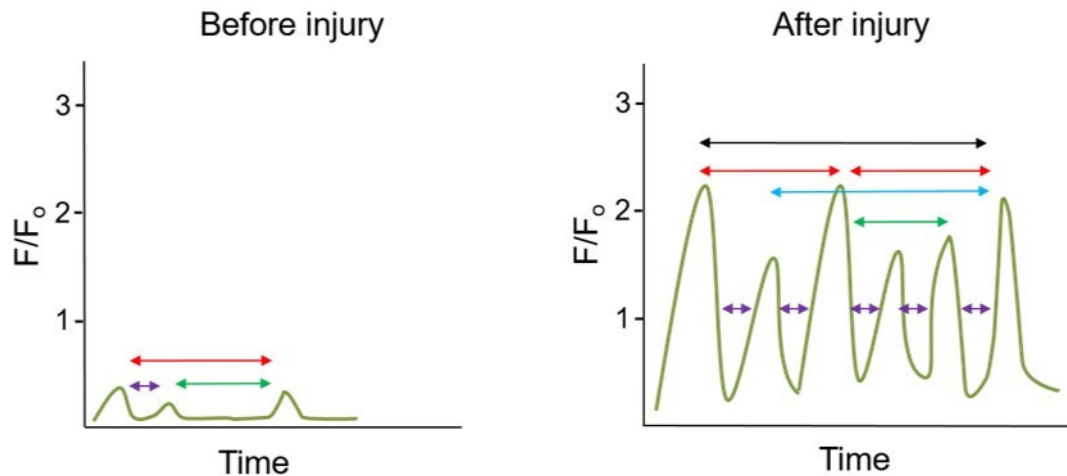
Figure 32: Summary of Ca^{++} signal response to tissue necrosis by TMs

Representative summary mean fluorescence intensity-time plots of a TM before and after laser injury showing differences in Ca^{++} signal parameters; arrows of different colors correspond to different periods/frequencies.

Because we hypothesize a focal necrosis generates gradients of DAMPs, chemokines, and lipid mediators depending on the distance to the necrosis, we investigated if the activation status and Ca^{++} signals of TM is also influenced by this (Weninger, Biro, and Jain 2014). In line with the hypothesis, we found that CX3CR1$^+$ cells closer to the site of necrosis were activated earlier and exhibited increased activity as indicated by overall Ca^{++} signal intensity, number of short and long lasting transients, and percentage of cells with transients (**Figure 33**).
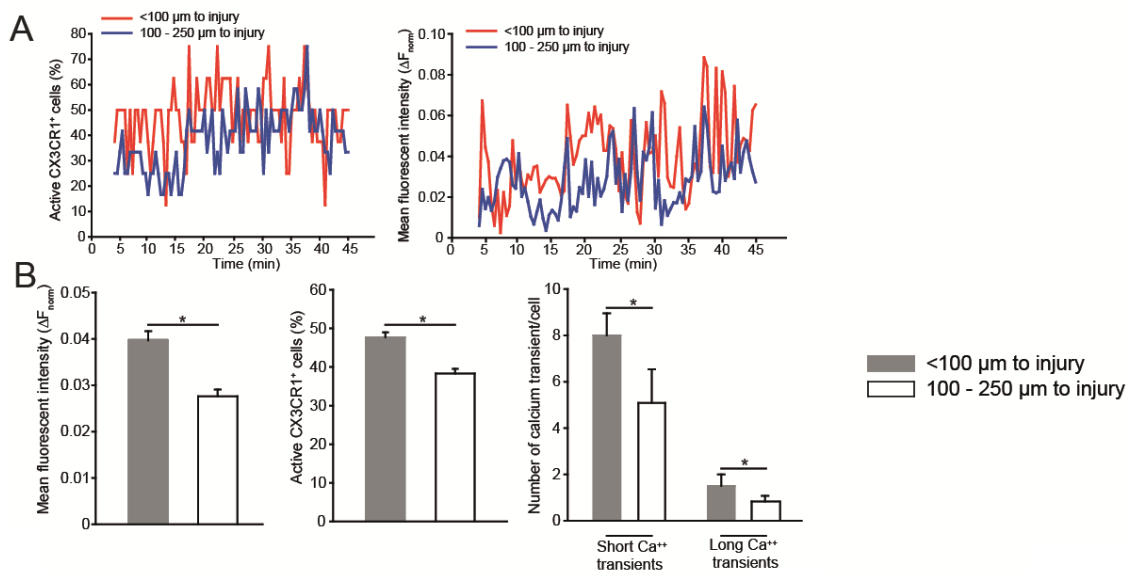
Figure 33: Distance-to-site-of-necrosis-dependent activation of myeloid leukocytes

A. **Left**: Representative temporal distribution of active TMs (percentage of those in field of view) within a 100-µm radius of the laser injury versus farther out. **Right**: Representative mean fluorescence intensity-time plot of TMs within a 100-µm radius of the laser injury versus farther out.

B. **Left**: Average Ca^{++} fluorescence intensity difference of TMs within a 100-µm radius of a laser injury versus 100 - 250 µm. **Middle**: Percentage of active TMs within a 100-µm radius of the laser injury versus farther out. **Right**: Number of Ca^{++} transients per TM within a 100-µm radius of the laser injury versus farther out, for both short and long Ca^{++} transients. Unpaired t-test; *$P \leq 0.05$, n = 5 mice per group; means ± SEM.

Similarly, neutrophils displayed spatial-dependent activation as evidenced in terms of average Ca^{++} signal intensity, amplitude, and PSD (**Figure 34**).
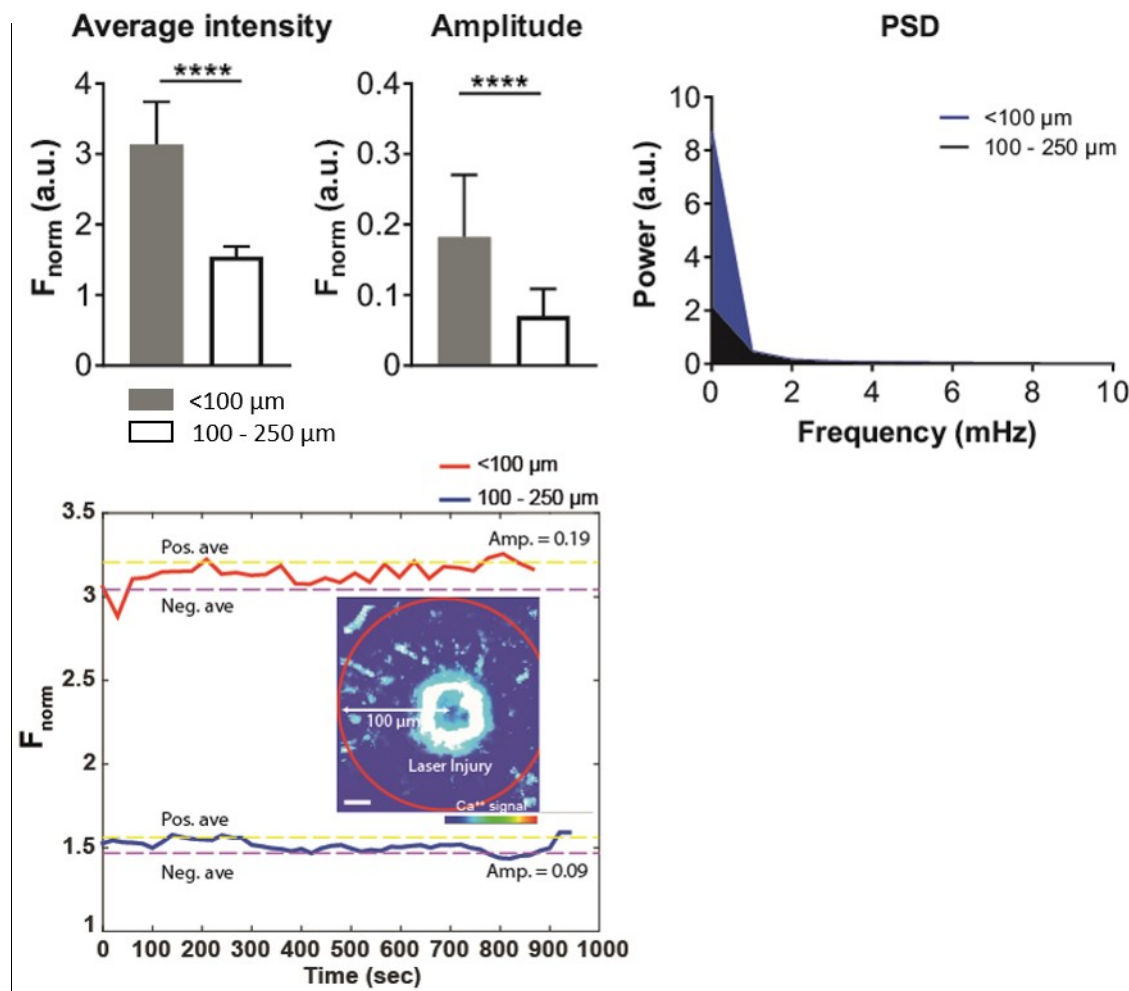
Figure 34: Distance-to-site-of-necrosis-dependent activation of myeloid leukocytes II

Top-left: Average Ca^{++} fluorescence intensity and amplitude of neutrophils within a 100-μm radius of a laser injury versus 100 - 250 μm. **Top-right**: PSD plot of neutrophils within a 100-μm radius of a laser injury versus 100 - 250 μm. **Bottom**: Average Ca^{++} fluorescence intensity-time plots of neutrophils within a 100-μm radius of a laser injury versus 100 - 250 μm. Unpaired t-test; ****P ≤ 0.0001, n = 14 and 18 cells per group; means ± SEM. Inset shows neutrophils in the vicinity of the laser injury in a LysMCre-GCaMP5G-IRES-td-tomatofl/fl mouse. Scale bar, 20 μm

Furthermore, we observed a higher number of Ca^{++} bursts in peritoneal macrophages *in vitro* after activation by HMGB1, although the average intensity and amplitude remained unaltered. This was coupled to a higher power after injury in the PSD, which is indicative of activation in terms of increased amplitude across the whole frequency spectrum – i.e. both short and long transient oscillations (**Figure 35**).
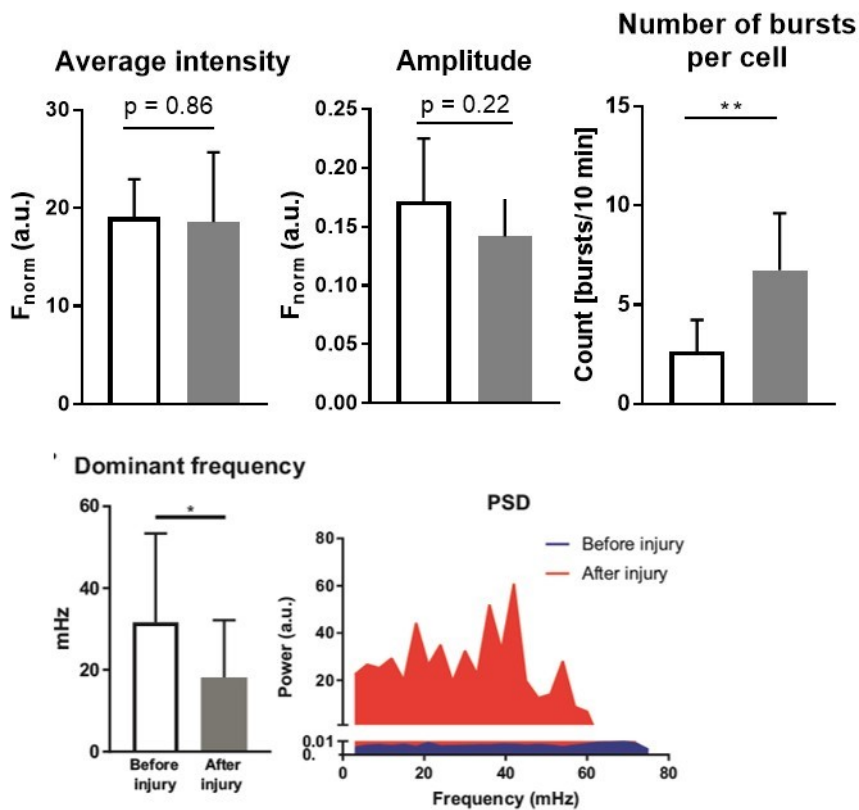
Figure 35: DAMP-dependent activation of myeloid leukocytes

Top-left: Average intensity of peritoneal macrophages *in vitro* before versus after HMGB1 treatment. **Top-middle**: Amplitude of the same macrophages before versus after HMGB1 treatment. **Top-right**: Number of Ca^{++} transients per macrophage visible during a 10-minute period before versus after HMGB1 treatment. Unpaired t-test; *P ≤ 0.05; means ± SEM. **Bottom-left**: Dominant frequency in TMs before versus after laser injury. **Bottom-right**: PSD plot of the macrophages before versus after laser injury. Unpaired t-test, **P ≤ 0.01; n = 3/5 mice per group; means ± SEM.

Hence, application of our Ca^{++} imaging system allowed the identification of TMs as first responders to sterile inflammation *in vivo* as demonstrated by enhanced Ca^{++} signaling, which was affected by the proximity to the tissue injury (**Figure 36**).
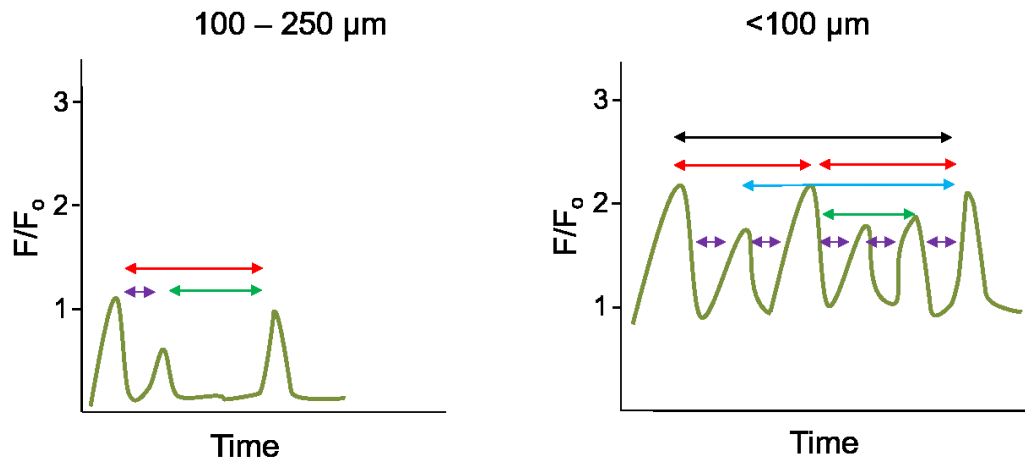
Figure 36: Ca^{++} signal response to tissue necrosis by TMs summary

Representative summary mean fluorescence intensity-time plots of a TM within a 100-µm radius of the laser injury versus farther out showing differences in Ca^{++} signal parameters; arrows of different colors correspond to different periods/frequencies.

3.1.3 Distinct Ca^{++} signal patterns during neutrophil recruitment stages *in vivo*

Having characterized the Ca^{++} activity in immotile TMs by 2P-IVM on a cellular level, we now wanted to assess the Ca^{++} dynamics of migrating neutrophils. For that purpose, we utilized intravital SDCM in the cremaster muscle after intrascrotal fMLP injection providing a subcellular spatial resolution and a temporal resolution in the range of milliseconds. This made it possible to determine Ca^{++} dynamics during the leukocyte recruitment cascade in *LysM^{Cre}-GCaMP5G-IRES-td-tomato$^{fl/fl}$* mice *in vivo*. During rolling on the endothelium, neutrophils had the highest Ca^{++} signal intensity in the center and on the endothelial-contacting side (**Figure 37**).
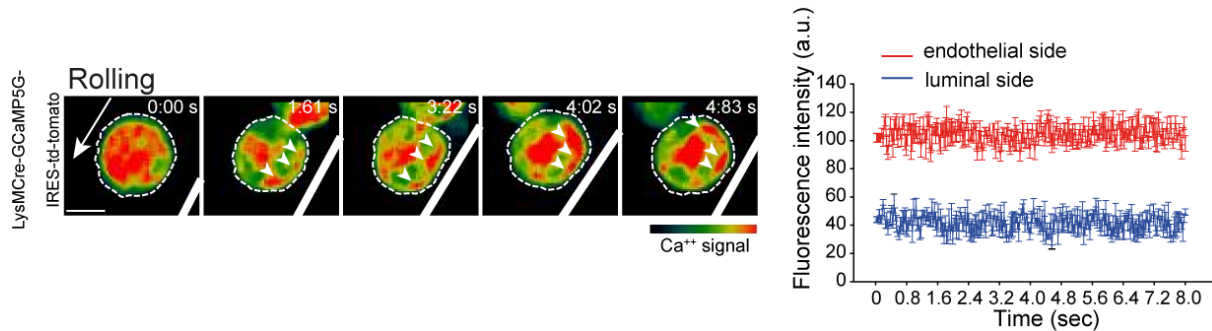
Figure 37: Intracellular Ca^{++} dynamics of neutrophils during rolling

Left: Time-lapse images of a neutrophil rolling along the endothelial wall in the cremaster muscle showing its spatiotemporal Ca^{++} signal distribution in pseudocolor mode. Arrow indicates overall direction of flow, whereas arrowheads point out pouches of high Ca^{++} concentration. Scale bar, 10 µm. Time is indicated as sec:millisec. **Right**: Fluorescence intensity-time plot of the neutrophil's shows higher intensity on the endothelial side versus the luminal side (n = 20 cells).

3. Results

During the following step of firm adhesion and arrest, neutrophils had a sharp increase of Ca^{++} signal in the whole cell, which shifted to a polarized pattern to the front when transmigration was initiated in the intravascular compartment (phase 1) (**Figure 38**).
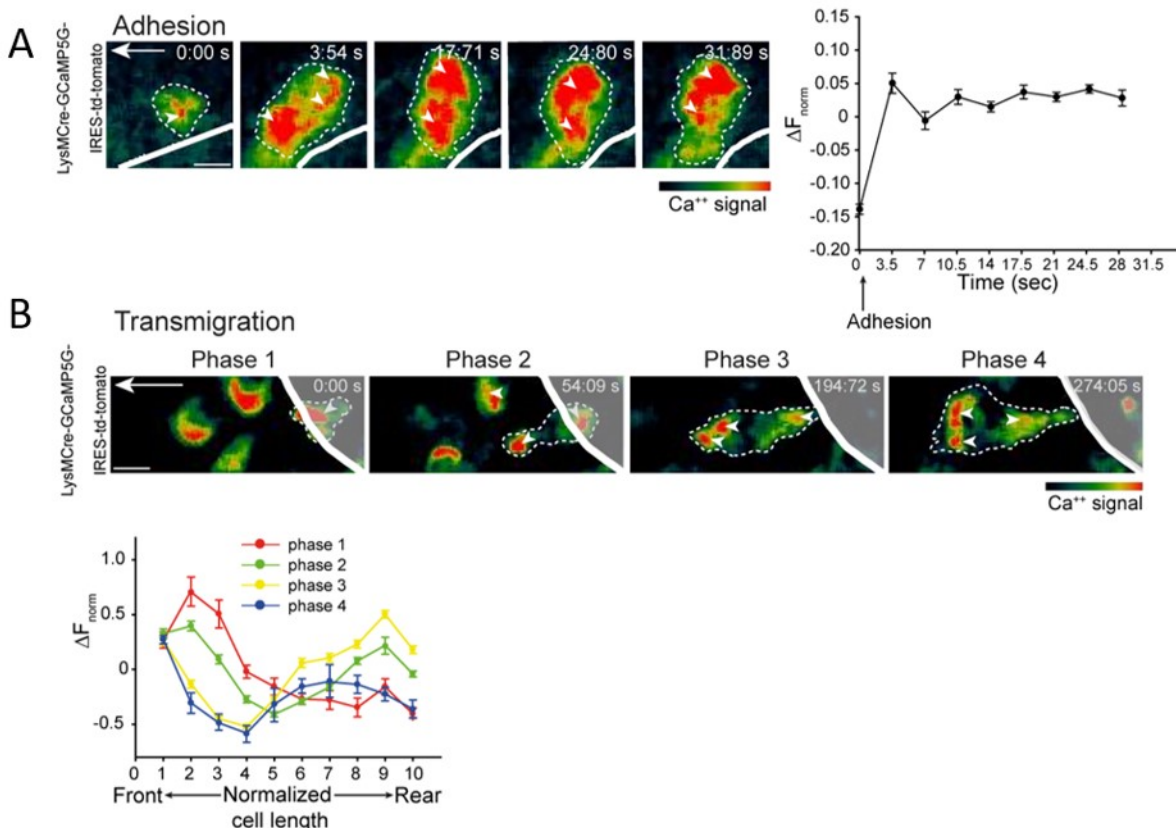
Figure 38: Intracellular Ca^{++} dynamics of neutrophils during adhesion and transmigration

- **A.** **Left**: Time-lapse images of a neutrophil adherent on the endothelial wall in the cremaster muscle showing its spatiotemporal Ca^{++} signal distribution in pseudocolor mode. Arrow indicates overall direction of flow. Scale bar, 10 µm. Time is indicated as sec:millisec. **Right**: Mean fluorescence intensity-time plot of the neutrophil's Ca^{++} signal shows sharp increase at point of adhesion and remains sustained afterwards (n = 14 cells).
- **B.** **Top**: Time-lapse images of a neutrophil transmigrating through the endothelial wall in the cremaster muscle with its spatiotemporal Ca^{++} signal distribution in pseudocolor mode depict phases 1 to 4 (left to right) of the transmigration process. Arrow indicates overall migration direction. Scale bar, 10 µm. Time is indicated as sec:millisec. **Bottom**: Mean fluorescence intensity profile across the length of a transmigrating neutrophil (normalized to direction of migration, where 10 is the lagging edge and 1 is the leading edge). Each of the four successive stages of the transmigration process is depicted by its mean profile with a unique color (n = 13 cells), bound by 95% confidence intervals (dashed lines).

During latter stages of transmigration, the Ca^{++} activity remained polarized. As the neutrophils extended from the blood stream into the interstitial space (phase 2) as well as when they reached the interstitial space (phase 3), they displayed strong intensity at the leading and trailing edges. After fully leaving the vasculature and arriving in the interstitial space, the Ca^{++} signal was polarized to the lamellipodium (phase 4) and remained so during interstitial migration with a polarization in the direction of migration (**Figure 38, Figure 39**).
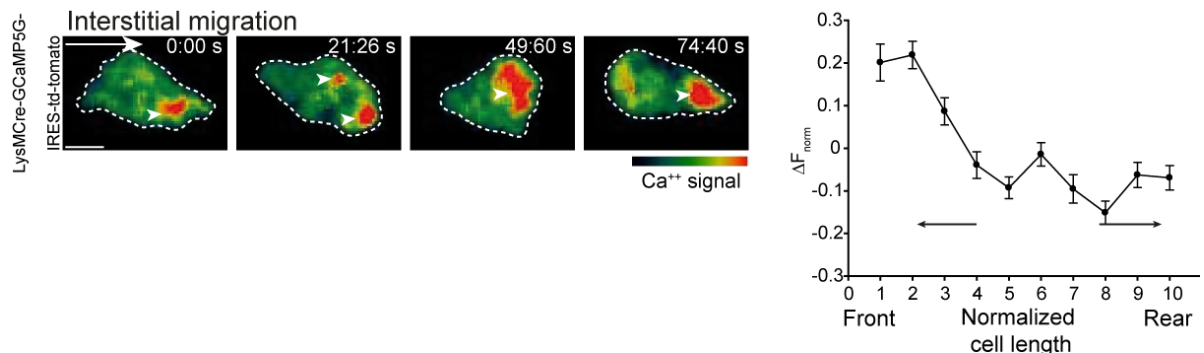
Figure 39: Intracellular *Ca++ dynamics of neutrophils during interstitial migration in vivo*

Left: Time-lapse images of a neutrophil migrating through the interstitial space in the cremaster muscle with its spatiotemporal Ca++ signal distribution in pseudocolor mode depict the leading edge as highest in Ca++ signal intensity. Arrow indicates overall migration direction. Scale bar, 10 µm. Time is indicated as sec:millisec. **Right**: Mean fluorescence intensity profile across the length of an interstitially migrating neutrophil (normalized to direction of migration, where 10 is the lagging edge and 1 is the leading edge). The migration process is depicted by its mean profile (n = 18 cells), bound by 95% confidence intervals (dashed lines).

At this stage, there was no correlation in instantaneous change in normalized Ca++ signal intensity to that of change in cell speed or change in direction of interstitial cell migration (**Figure 40**). In summary, the intracellular distribution of Ca++ signal in neutrophils depends on the stage of the leukocyte cascade and allows conclusions on the leading edge during neutrophil interstitial migration, while the transition from rolling to adhesion is marked by a whole cell Ca++ burst.
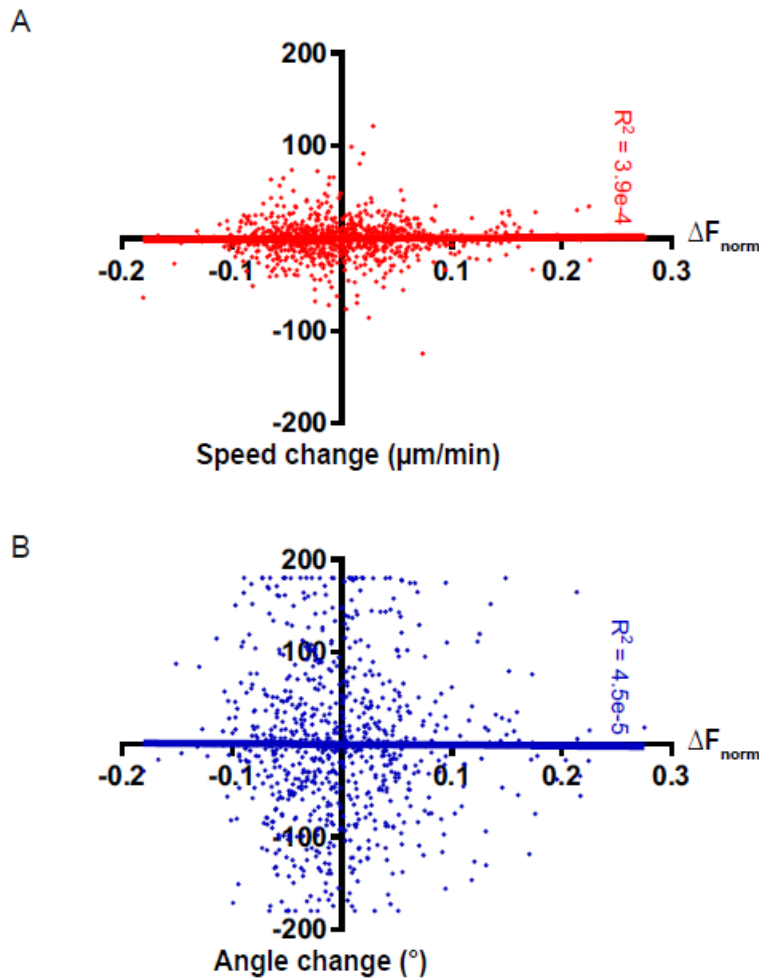
Figure 40: Correlation of migration speed and angle change to Ca⁺⁺ signal in neutrophils *in vivo*

    A. Mean fluorescence intensity-speed change correlations show no effect of instantaneous Ca^{++} signal changes on speed changes in neutrophils during interstitial migration.

    B. Mean fluorescence intensity-speed change correlations also show no effect of instantaneous Ca^{++} signal changes on direction changes in neutrophils during interstitial migration.

3.1.4 G-protein coupled receptors orchestrate neutrophil Ca^{++} dynamics during the migration cascade

Gαi-PCRs have been shown to orchestrate leukocyte Ca^{++} signals *in vitro*. We therefore tested if our setup detects the influence of inhibiting G-PCR *in vivo*. For that reason, we assessed how pertussis toxin (PTx) influences Ca^{++} signaling of neutrophils *in vivo* using the same inflamed cremaster muscle model as in section 3.4 in *LysM^Cre^-GCaMP5G-IRES-td-tomato^fl/fl^* reporter mice (**Figure 13**).

Staining the control and treated groups with differently colored markers made it possible to identify both groups simultaneously during intravital SDCM (**Figure 41**). PTx was selected for this purpose because it is known to deactivate Gαi-PCR of neutrophils, an important regulatory mechanisms of intracellular Ca^{++} (Lad et al. 1985).
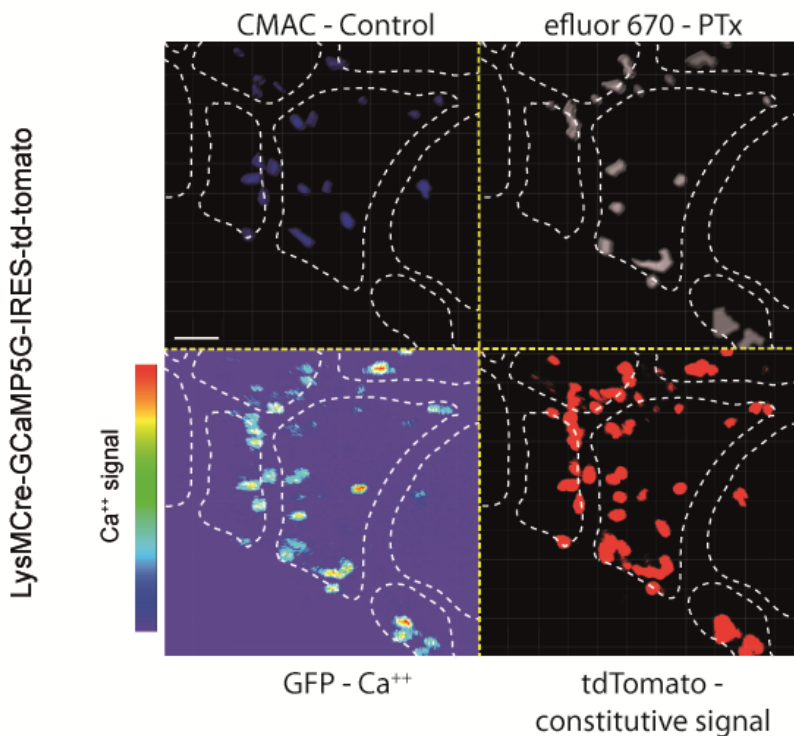
Figure 41: Gαi-PCR orchestration of *in vivo* Ca^{++} signal in neutrophil migration

Neutrophils from LysMCre-GCaMP5G-IRES-td-tomatofl/fl were adoptively transferred into a Black 6 mouse and observed in all migration stages within the microvasculature of the cremaster muscle. The different groups are displayed as follows: blue for non-treated control cells, grey for PTx-treated cells, pseudocolor mode for intracellular Ca^{++} signal and red for constitutive tdTomato. Still image from SDCM in the cremaster muscle *in vivo*. Scale bar, 30 μm.

During the first stage of the neutrophil migration cascade, PTx resulted in lower intensity and amplitudes in rolling cells in comparison to non-treated neutrophils. The treatment also led to a smaller dominant frequency, meaning longer transients (**Figure 42**).

However, once rolling cells had adhered and arrested on the endothelium, Gαi-PCR inhibition showed no significant difference in Ca^{++} signaling parameters. Migratory parameters are also not affected at this stage with adhesion being a rather stationary stage. In the second half of the migration cascade, the transmigration process is not affected by blockage of Gαi-PCRs in terms of migratory and Ca^{++} signaling parameters. Similarly, Gαi-PCRs do not seem to play a role in how fast or directed neutrophils leave the vasculature. The amount of transmigrated neutrophils at various time points after adoptive transfer showed no change when compared between control and PTx-treated groups (**Figure 43**).
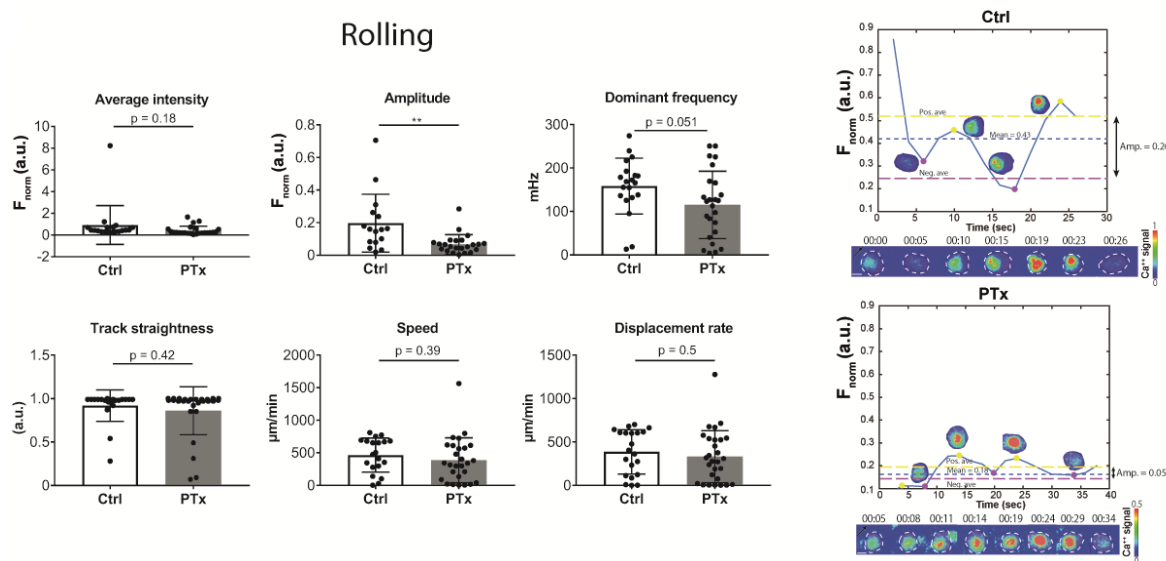
Figure 42: Gαi-PCR orchestration of *in vivo* Ca⁺⁺ signal during neutrophil rolling

Ca⁺⁺ signal parameters (average intensity, amplitude and dominant frequency) and migration parameters (track straightness, speed and displacement rate) of control versus PTx-treated neutrophils during rolling. Unpaired t-test, **P ≤ 0.01; n = 4 mice per group; means ± SEM. These are accompanied by representative mean fluorescence intensity-time plots and time-lapse images of each group. Scale bar, 5 μm. Time is indicated as min:sec.
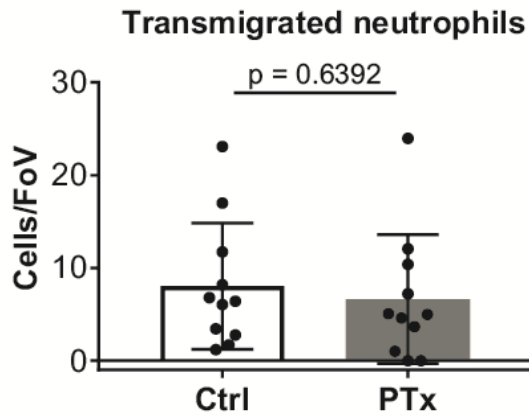
Figure 43: Neutrophil adoptive transfer

Number of neutrophils per field of view (500 μm x 500 μm) that transmigrated into the interstitial space in control versus PTx-treated groups. n = 3 mice per group; means ± SEM.

Once in the interstitial space, PTx-treated neutrophils exhibit higher amplitudes than control neutrophils during migration but no change in average intensity, dominant frequency and migratory parameters (**Figure 44**).
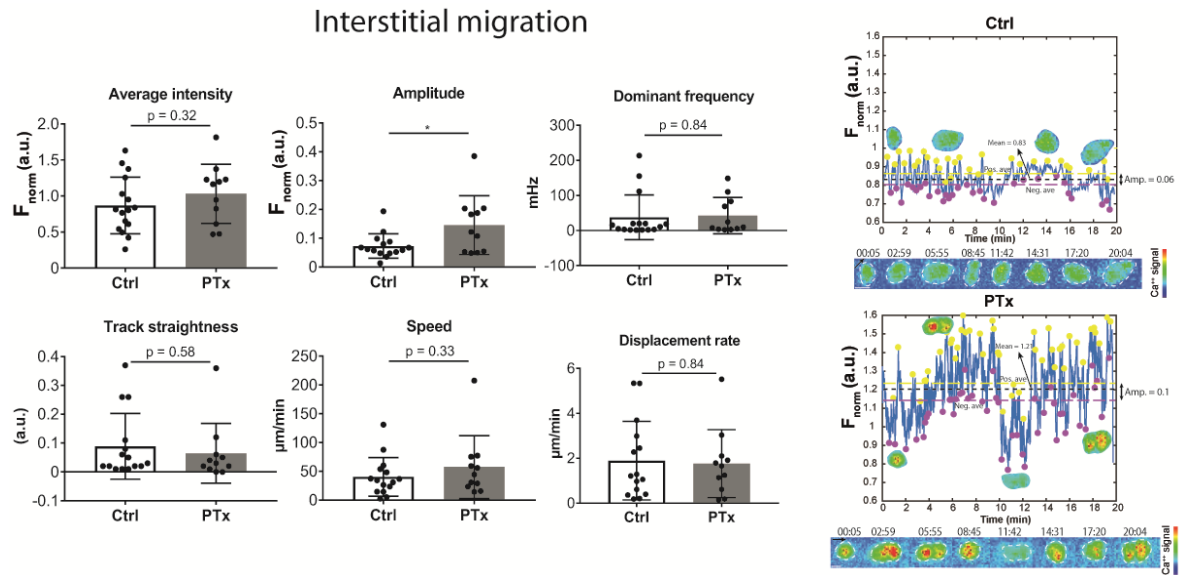
Figure 44: Gαi-PCR orchestration of *in vivo* Ca⁺⁺ signal in neutrophil interstitial migration

Ca⁺⁺ signal and migration parameters of control versus PTx-treated interstitially migrating neutrophils. Unpaired t-test, *P ≤ 0.05; n = 4/3 mice per group; means ± SEM. These are accompanied by representative mean fluorescence intensity-time plots and time-lapse images of each group. Scale bar, 5 μm. Time is indicated as min:sec.

We next looked at the development of the cascade stages in the control case and in Gαi-PCR blockage and used the same adoptive transfer experiments to do this. Concerning migratory parameters, rolling showed significantly elevated motion directedness, speed, and displacement rate in both control and Gαi-PCR-blocked neutrophils. With regard to Ca⁺⁺ signaling parameters, signal intensity remained unaltered throughout whereas amplitude and frequency were significantly increased during rolling in the control case. When Gαi-PCRs were blocked, rolling signal intensity fell significantly lower than the rest of the field, amplitude was highest during interstitial migration and dominant frequency remained highest during rolling like in the control case (**Figure 45**).
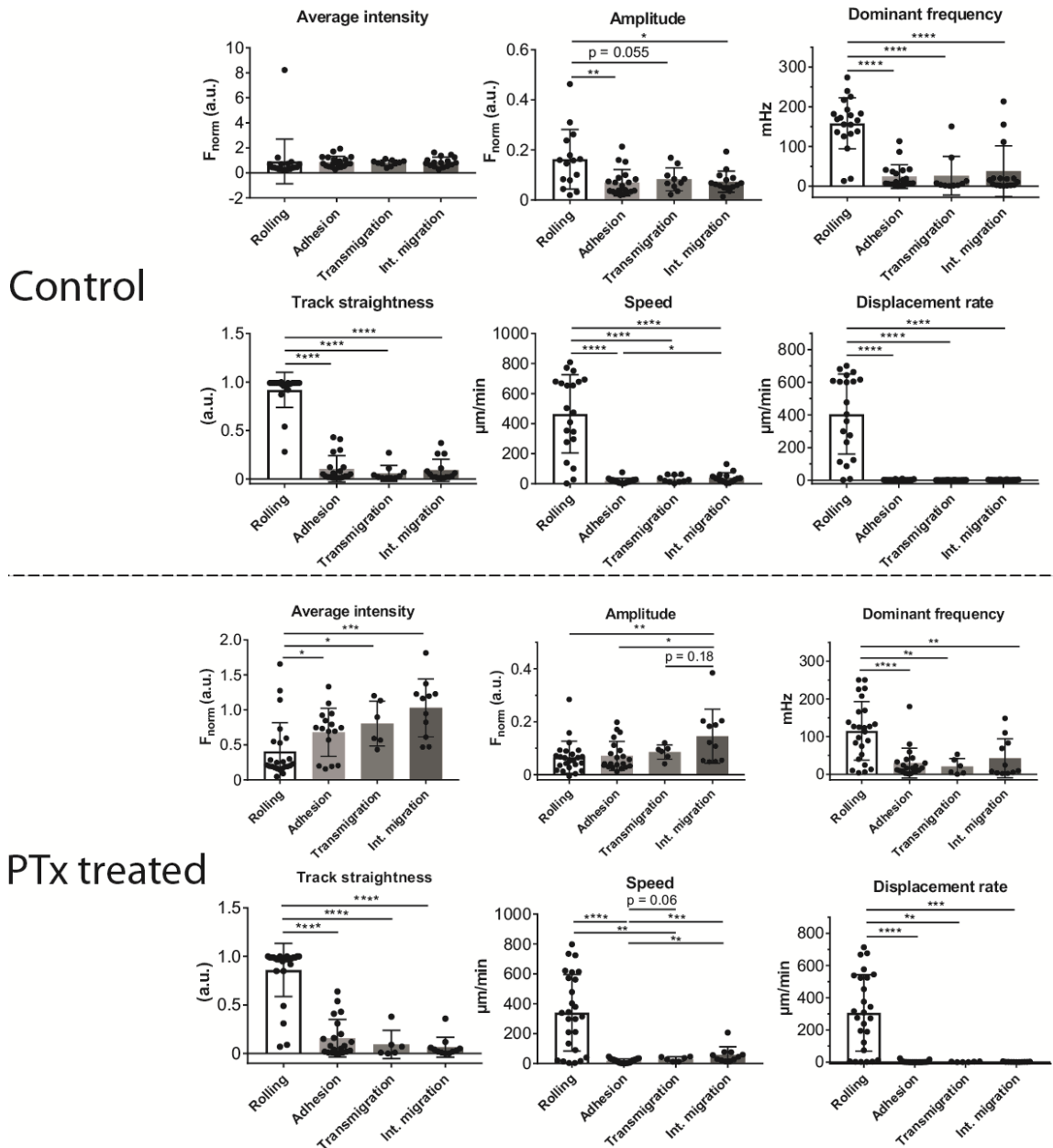
Figure 45: Ca⁺⁺ signaling parameters during neutrophil adoptive transfer

Top: Ca⁺⁺ signal parameters (average intensity, amplitude and dominant frequency) and migration parameters (track straightness, speed and displacement rate) of control neutrophils along the migration cascade. Unpaired t-test, *P ≤ 0.05, **P ≤ 0.01, ****P ≤ 0.0001; n = 3 - 5 mice per group; means ± SEM. **Bottom**: Ca⁺⁺ signal parameters and migration of PTx-treated neutrophils along the migration cascade. Unpaired t-test, *P ≤ 0.05, **P ≤ 0.01, ***P ≤ 0.001 ****P ≤ 0.0001; n = 3-4 mice per group; means ± SEM.

To further analyze differences in the signals of the control cells and PTx-treated cells that would not be revealed by classical parameters, we compared the PSD of all migratory stages of neutrophils from the two groups. The biggest difference was observed during rolling, with the power falling drastically after PTx treatment indicating less activation when Gαi-PCRs are blocked. During interstitial migration, the area under the PSD curve is unchanged but Gαi-PCR blockage shifted the PSD curve towards the lower end of the frequency spectrum, i.e. longer

oscillations (**Figure 46**). Adhesion and transmigration were not affected in terms of PSD or by classical measures (**Figure 47**).
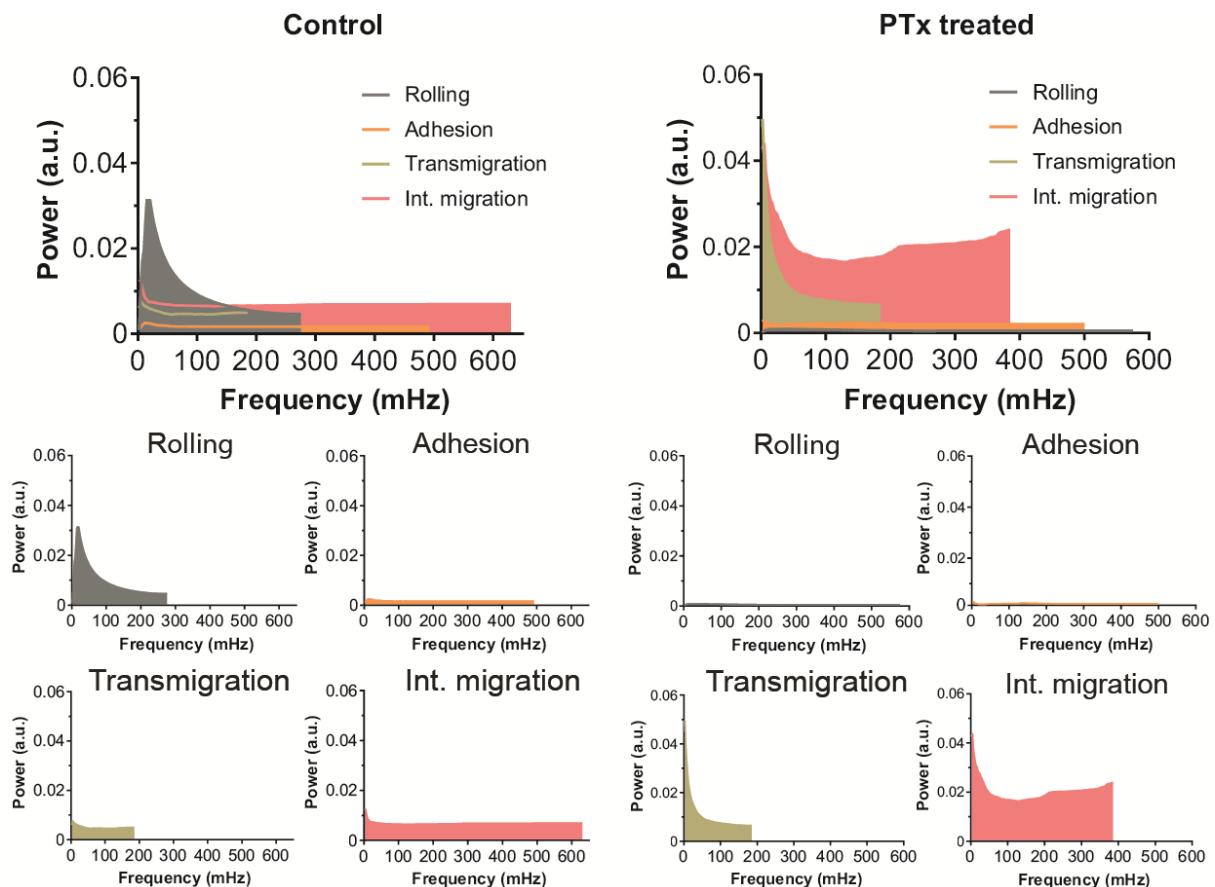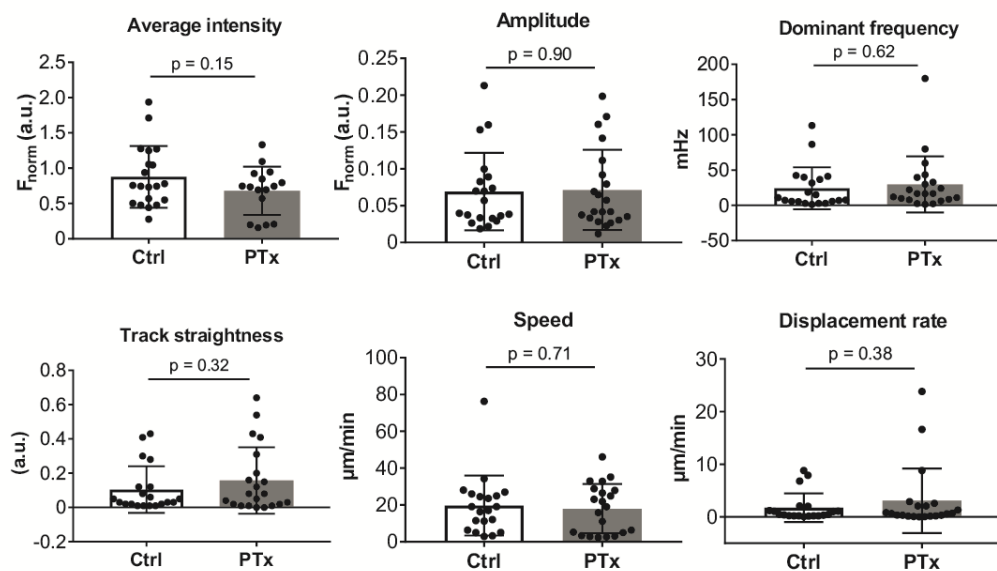
Figure 46: Gαi-PCR orchestration of *in vivo* Ca⁺⁺ signal in neutrophil migration II

Left: PSD plot of the cascade stages of control neutrophils displays rolling as the most active stage. **Right**: PSD plot of the cascade stages of PTx-treated neutrophils displays interstitial migration as the most active stage after Gαi-PCR intervention.

Adhesion

Transmigration
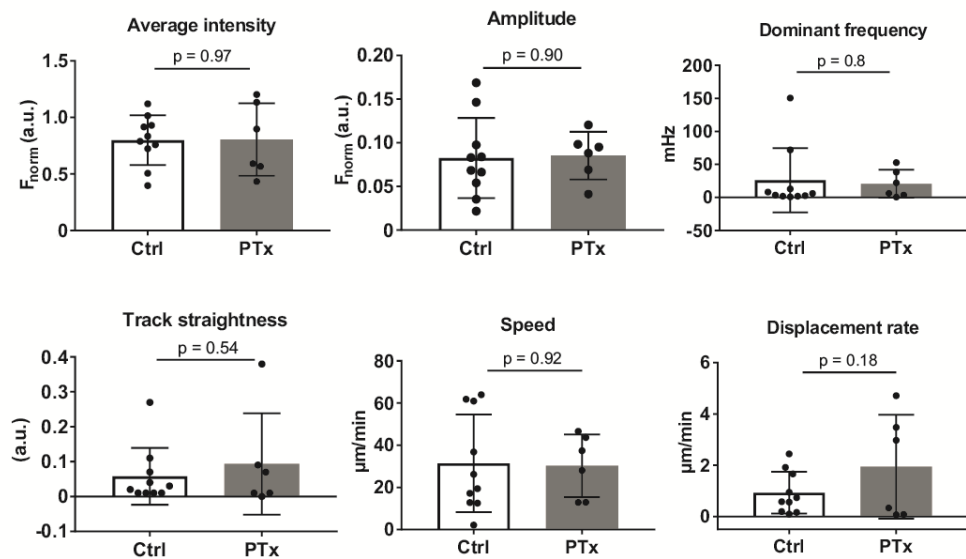
Figure 47: Neutrophil Ca^{++} and migration parameters during adhesion and transmigration

Ca^{++} signal and migration parameters of control versus PTx-treated adherent (n = 4/5 mice per group) and transmigrating (n = 3 mice per group) neutrophils. Unpaired t-test; means ± SEM.

In summary, Gαi-PCR inhibition reduces short Ca^{++} transients while keeping long Ca^{++} transients. Moreover, marking 2.5 seconds of interpeak temporal spacing (equivalent to 400 mHz frequency) as a watershed for short and long transients, short transients are heavily diminished in amplitude by Gαi-PCR inhibition, whereas that of longer transients is slightly elevated (**Figure 48**). In conclusion, Gαi-PCRs are implicated in the migration cascade of neutrophils as reflected by the change in Ca^{++} frequency spectra.
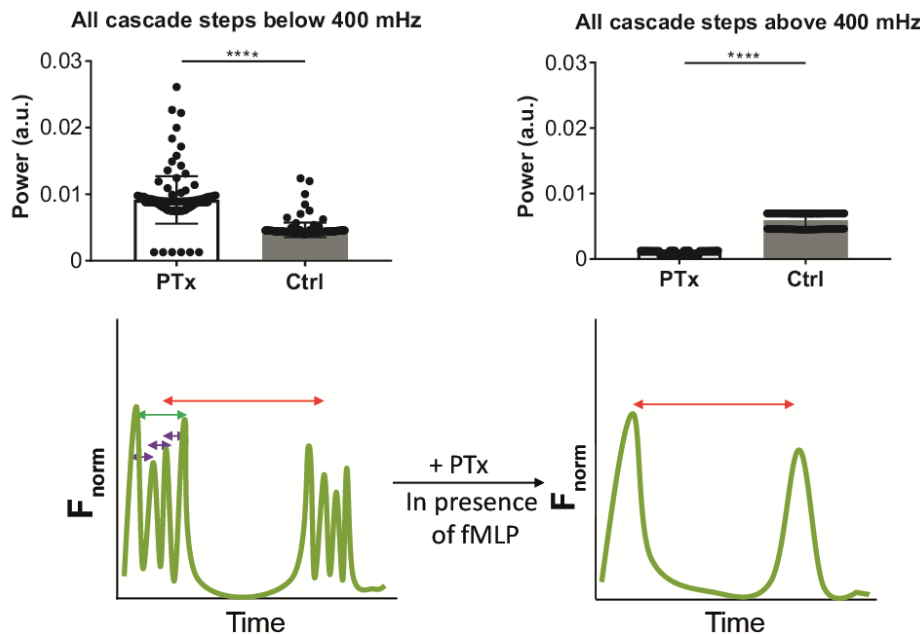
Figure 48: Neutrophil Ca^{++} and migration parameters during adhesion and transmigration

Top-left: Average power values below 400 mHz calculated from PSD plots with all migration stages combined for control and PTx-treated neutrophils. **Top-right**: Average power values above 400 mHz calculated from PSD plots with all migration stages combined for control and PTx-treated neutrophils. **Bottom**: Representative summary mean fluorescence intensity-time plots of a neutrophil show that short transients are abrogated by PTx treatment whereas long transients are not; arrows of different colors correspond to different periods/frequencies.

3.2 Abrogation of neutrophil accumulation by macrophage dendrite formation

Having characterized Ca^{++} signaling in neutrophils and macrophages during the initiation of inflammation, its dynamics during the resolution phase was analyzed next. Here, the analysis was focused on the interplay of tissue macrophages (TM) and neutrophils. When comparing neutrophil distance over time in TM-devoid and TM-filled areas around the same lesion site, we noticed more neutrophils came closer to the lesion site when there were no TMs in their way (**Figure 49a,b).** We also noticed the 2-hour mark to be the onset of dendrite formation in macrophages. Coincidentally, we found neutrophils swarmed the laser injury until that time point and then actively deflected their trajectory associated with direct contacts with dendrite forming macrophages

(**Figure 49c**). Hence, these data suggest an anti-inflammatory effect of TMs, limiting detrimental neutrophil accumulation through dendrite formation.
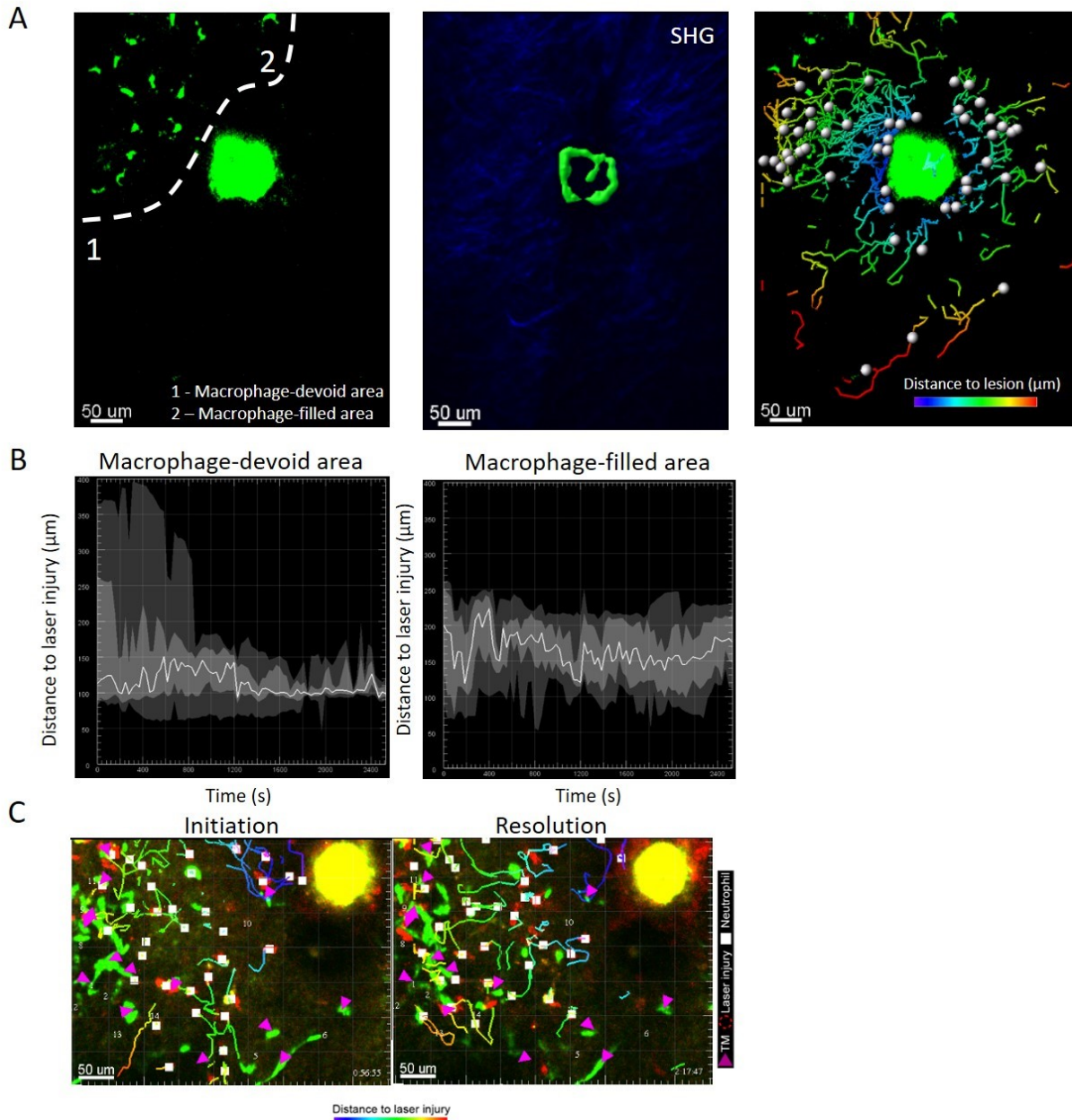
Figure 49: TM-dependent neutrophil recruitment to lesion site

    A.   Distinction of TM-devoid and TM-filled areas around a lesion site (left). Second harmonic generation depiction of the tissue around the tissue necrosis site, depicted in green (middle). Neutrophils' (spheres) migration tracks in these areas TM-devoid and TM filled areas (right) (n = 20 cells)

    B.   Distance of neutrophils from lesion sites versus time in the two areas. The dark-grey shades show the extent of the closest and farthest neutrophils from the lesion site while the light-grey shades represent the SEM (n = 20 cells).

    C.   Tracks of neutrophil displacement direction during initiation and resolution of tissue inflammation (n = 20 cells)

To investigate cellular activation on both sides of the interaction, we employed Ca^{++} signaling frequency analysis. We created LysMCre-PCGtTflox in CX3CR1eGFP chimera to analyze Ca^{++}-signals in neutrophils as they interacted with TMs. For TMs, we created CX3CR1Cre-PCGtTflox in Black 6 chimera and injected Ly6G-PE antibody to visualize interacting neutrophils. Neither cell type showed a significant change in normalized intensity, signal amplitude or dominant frequency when compared across all interaction stages (**Figure 50**). On the other hand, PSD analyses showed macrophages were more activated after interaction, whereas neutrophils were more activated before interaction (**Figure 51**).
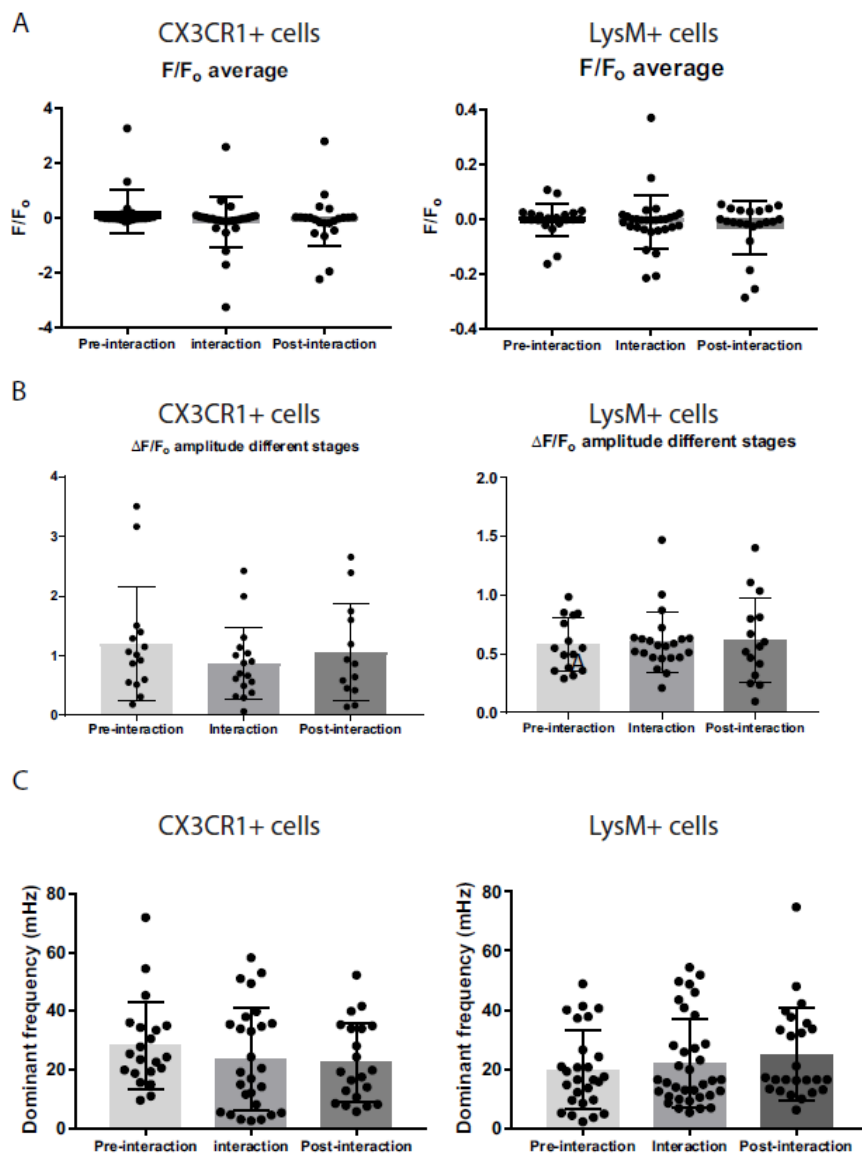
Figure 50: Ca^{++} signal parameters during interaction

Average intensity (A), amplitude (B) and dominant frequency (C) in CX3CR1+ and LysM+ cells across all interaction stages (n = 5)
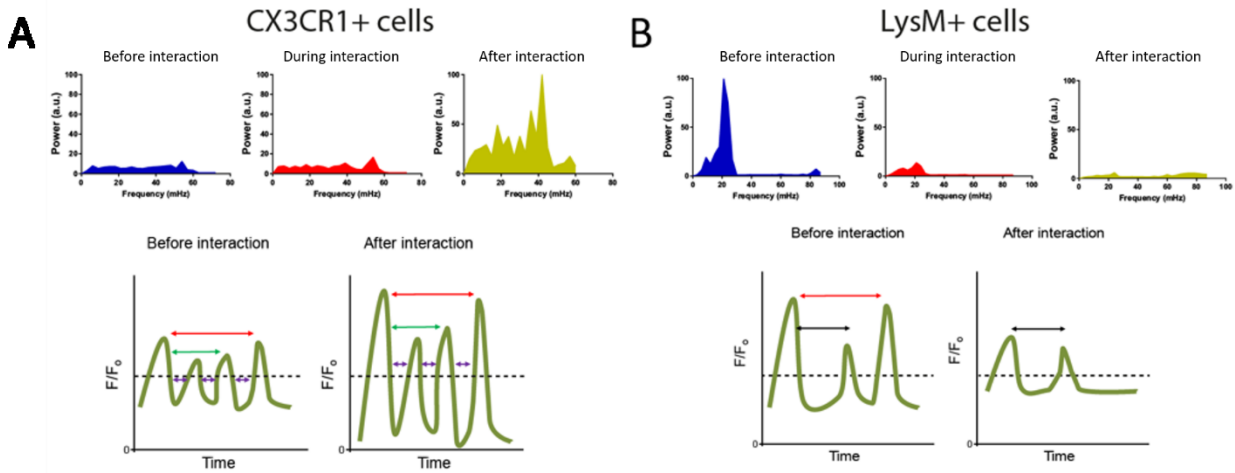
Figure 51: PSD plot of CX3CR1+ and LysM+ cells across all interaction stages

A. **Top:** PSD plots of TMs before, during and after interaction with neutrophils. **Bottom**: Summary Ca^{++}-signal tracing of TMs (n = 5 mice/30 cells).

B. **Top:** PSD plots of neutrophils before, during and after interaction with TMs. **Bottom**: Summary Ca^{++}-signal tracing of neutrophils (n = 5 mice/30 cells).

3.2.1 Neutrophil reprogramming depends on the presence of tissue macrophages

To check if there was causality between TMs and reprogramming of neutrophils, we administered a macrophage depleting PLX diet to CX3CR1eGFP mice. The number of TMs in the dermis diminished by 61% after CX3CR1eGFP mice were put on a 5-day PLX diet (**Figure 52**).
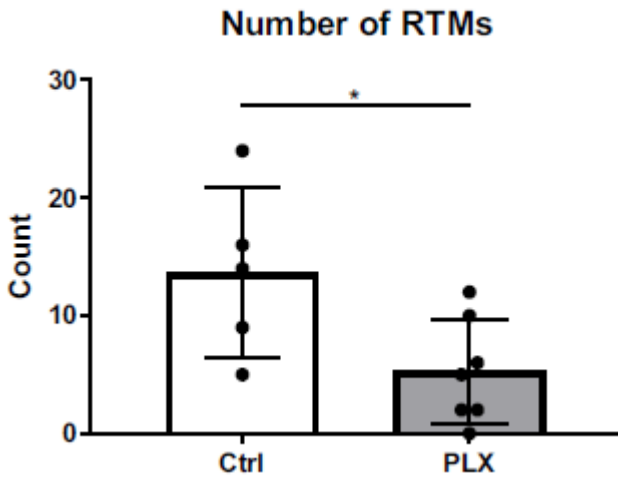
Figure 52: Number of TMs in control and PLX chow fed CX3CR1eGFP mice

The number of tissue macrophages per field of view in control and PLX chow fed CX3CR1eGFP mice showed the effectiveness of the PLX chow feed in significantly reducing the number of tissue macrophages (n = 5/7 mice per group).

Introduction of a laser injury in the dermis resulted in a sustained influx of neutrophils over several hours in both PLX treated and control mice. The TFI, which is the ratio of number of neutrophils

close to the tissue necrosis to that of neutrophils farther away, significantly increased with macrophage depletion (**Figure 53a**). An increase in TFI shows a more directed migration of neutrophils to the site of tissue necrosis. This suggests that when there were fewer macrophages in the tissue in the neutrophils' way, more neutrophils successfully made it to the site of necrosis possibly due to fewer interactions along their way. However, the total number of neutrophils within the imaging region of interest aggregated over the total imaging time of 5 hours was not significantly changed at single time points with macrophage depletion (**Figure 53b**). Therefore, TMs are involved in regulating tissue distribution and target finding behavior of neutrophils.
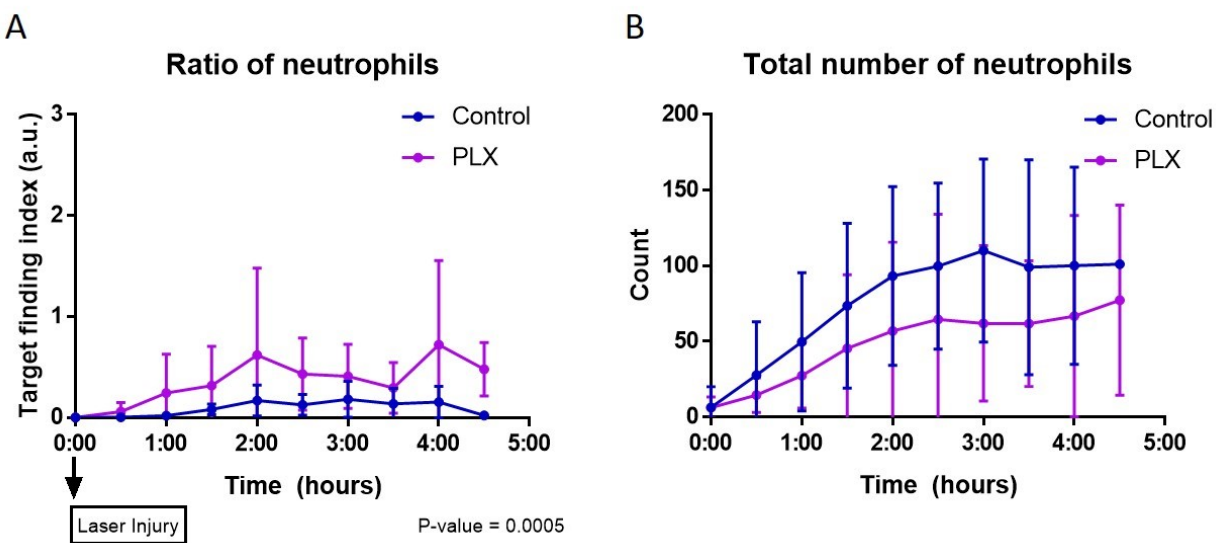
Figure 53: Target finding index and number of neutrophils per FoV in control and PLX chow fed mice

A. Neutrophil target finding index in the presence of a laser injury in the ear model is analyzed over 4 hours in control and PLX chow fed CX3CR1eGFP mice. TM depletion (PLX) results in higher proportion of neutrophils flocking to the tissue necrosis site (n = 5/7 mice per group).

B. The total number of neutrophils present in the field of view was not significantly different in control and PLX chow fed mice (n = 5/7 mice per group).

3.2.2 HMGB1- and TLR4-dependent dendrite formation in macrophages

To test if dendrite formation in interstitial TMs is specific for sterile inflammation, we exposed CX3CR1eGFP^kiwt mice to an intradermal E. coli injection, which also leads to protrusions with similar temporal dynamics (**Figure 54**).
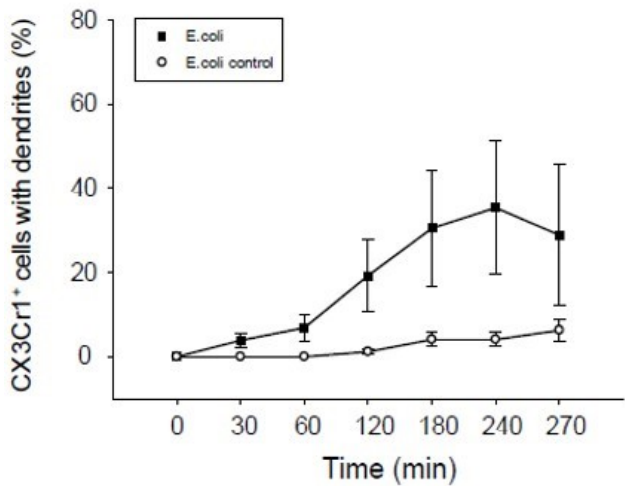
Figure 54: Dendrite formation in CX3CR1+ cells stimulated by E. coli

Laser injury-induced tissue inflammation was placed in the ears CX3CR1eGFP mice after intradermal injection of PBS (control) and E. coli. The proportion of TMs forming dendrites was then compared over 4 hours. Dendrite formation was significantly heightened in the case of E. coli (n = 3 mice).

To assess the mechanism of dendrite formation, we tested the importance of the CX3CR1-CX3CL1 axis in the setting of a focal necrosis, but dendrite formation in CX3CR1eGFP^{kiwt} and CX3CR1eGFP^{kiki} mice was equal (**Figure 55**).
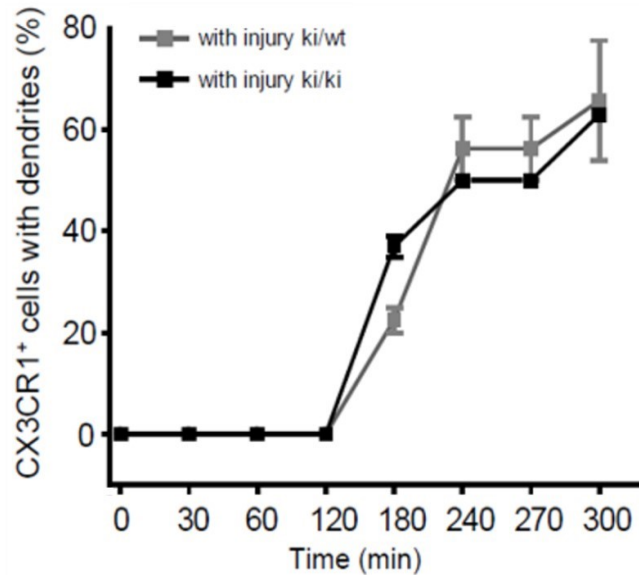
Figure 55: Mechanisms of dendrite formation in TMs

Laser injury-induced tissue inflammation was placed in the ears CX3CR1eGFP ki/wt and ki/ki mice and the time after injury TMs took to form dendrites was observed. Dendrite formation in CX3CR1+ cells does not depend on CX3CR1-CX3CL1 axis (n = 4 mice).

To gain a mechanistic understanding of dendrite formation in CX3CR1$^+$ cells, we intradermally injected C34, a TLR4 antagonist, and Rage Antagonist Peptide (RAP). Compared to a PBS control, TLR4 inhibition significantly reduced the number of dendrite forming macrophages whereas RAP did not. No change was observed in the temporal onset of dendrite formation (**Figure 56a**).

To test if the interaction with other cell types might influence the protrusion of dendrites, we depleted neutrophils (with a neutrophil-depleting antibodies; anti-Ly6G (1A8)) and introduced a focal lesion in CX3CR1eGFP^{kiwt} mice. This resulted in a marked acceleration of dendrite formation, which could now be detected within 30 min after laser injury, compared to 120 min in isotype treated mice. Moreover, HMGB1 proved to be critical for dendrite formation in macrophages, because application of the HMGB1 antagonist BoxA significantly impaired this process after laser injury (**Figure 56b**).
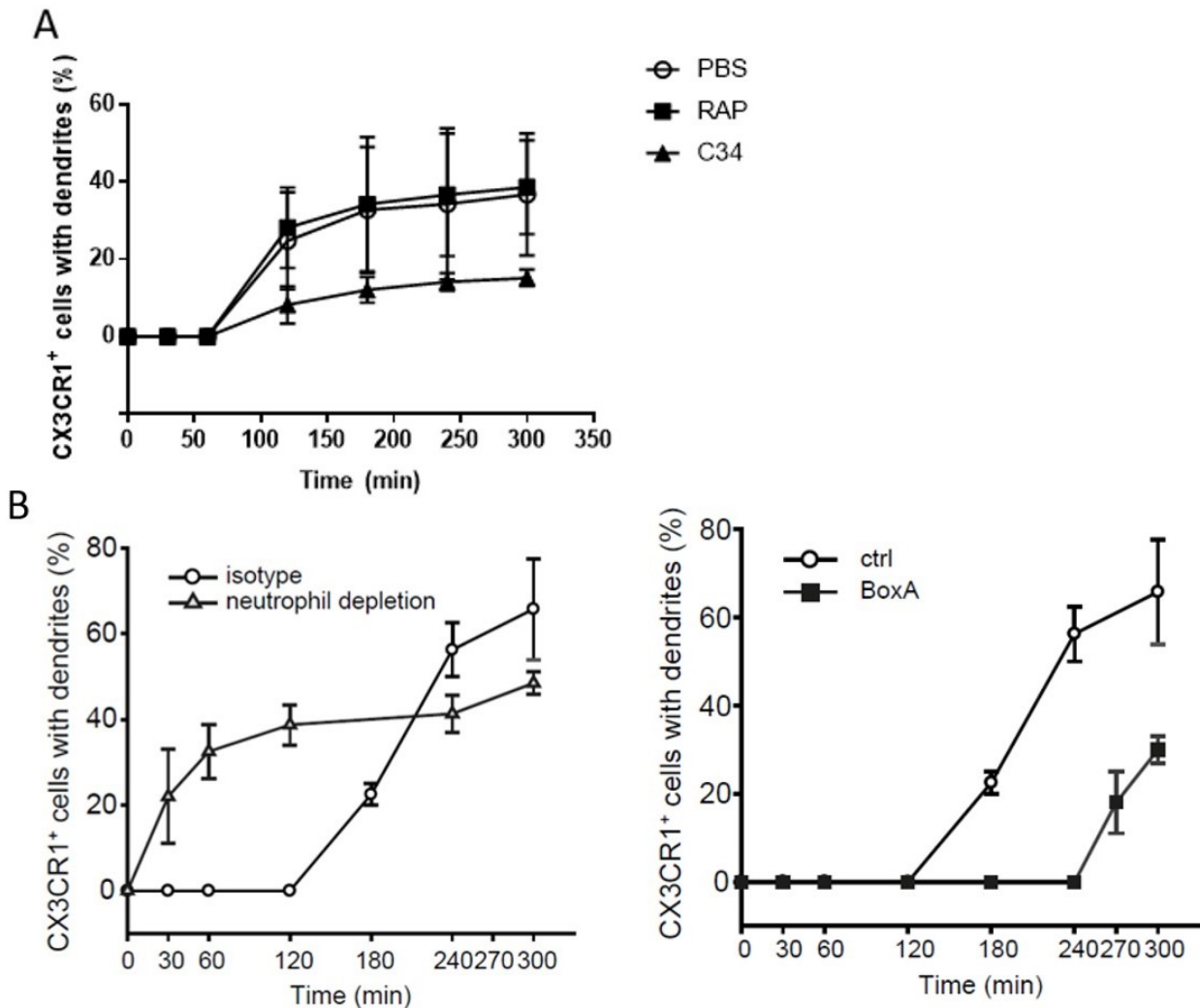
Figure 56: Mechanisms of dendrite formation in TMs II

A.   TLR4 mediates dendrite formation in CX3CR1+ cells (n = 5)

B.   **Left**: neutrophil presence suppresses dendrite formation in CX3CR1+ cells. **Right**: CX3CR1eGFP ki/wt mice were intradermally injected with either PBS (control) or BoxA after which laser injury-induced tissue inflammation was placed in their ears. HMGB1 inhibition by BoxA suppresses dendrite formation in CX3CR1+ cells (n = 4)

To find out if dendrite formation in TMs activates Ca^{++} signaling, we imaged dendrite formation in PC-G5-tdTflox x CX3CR1cre mice and compared Ca^{++} signaling parameters before and after dendrite formation. Interestingly, dendrite formation in TMs does not correlate to changes in the Ca^{++} signal (**Figure 57**). In summary, TMs form dendrites depending on HMGB1 and TLR4.
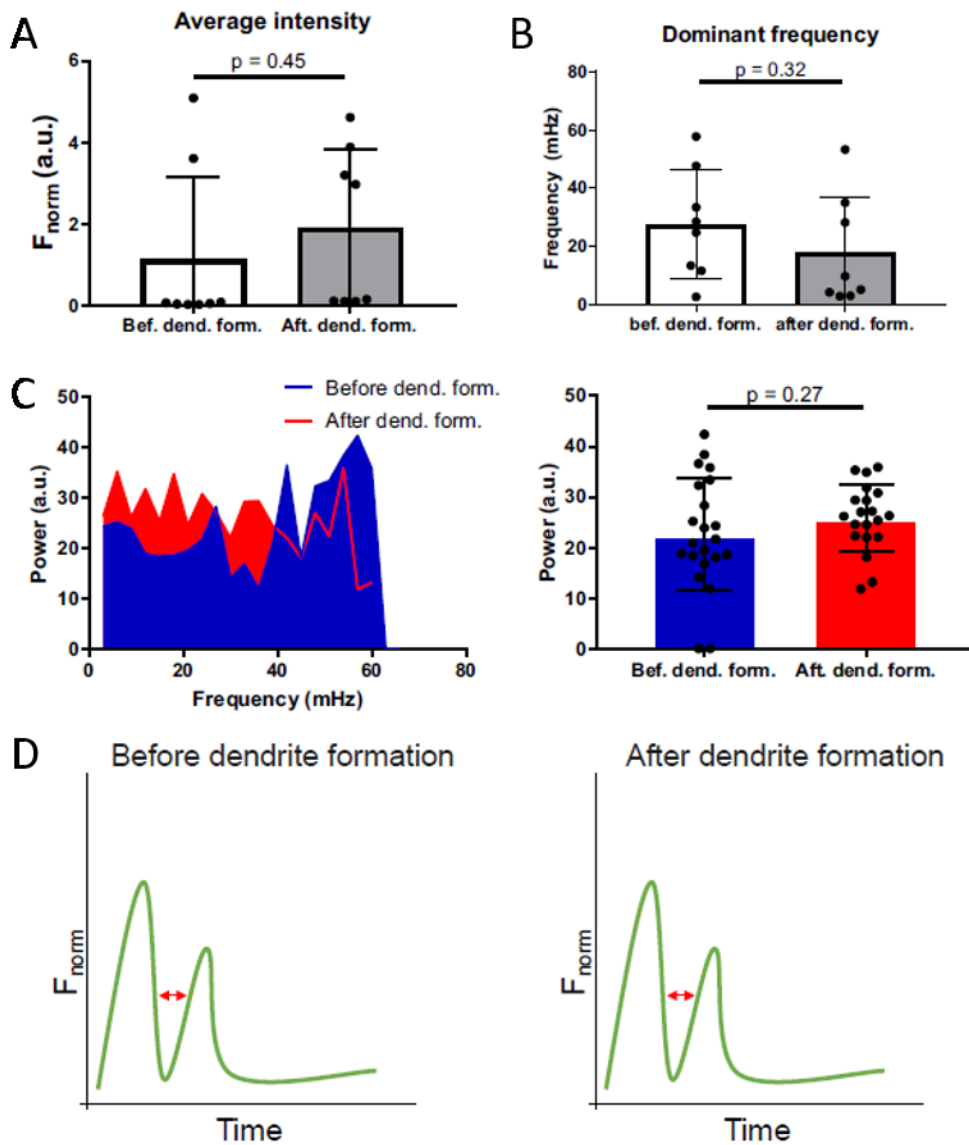
Figure 57: Ca⁺⁺ signal parameters during dendrite formation

Average intensity (A), amplitude (B) and PSD (C) reflect no change in cellular activation in CX3CR1+ cells as a result of dendrite formation. This is captured in the general scheme (D) (n = 5 mice).

3.2.3 LFA-1 mediated neutrophil reprogramming by TMs

Next, we designed an experiment where LFA-1 would be blocked by a blocking antibody compared to an isotype control to investigate if neutrophil reprogramming was dependent on physical contacts with TMs. To do so, we injected an LFA-1 blocking agent or the isotype control in CX3CR1eGFP mice intradermally and labeled neutrophils with Ly6G-PE antibody i.v. When LFA-1 was blocked, neutrophils were significantly faster than control neutrophils during interaction with macrophages and the duration of interaction was decreased with neutrophils spending half as much time interacting with TMs (**Figure 58**).
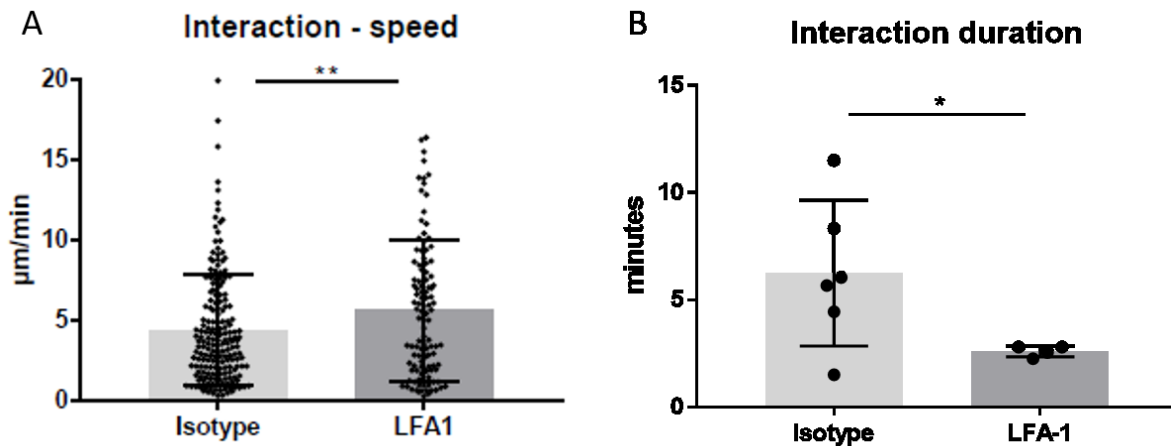
Figure 58: Effect of LFA-1 inhibition on neutrophil speed and interaction duration during neutrophil-TM interaction

A. Neutrophil speed was analyzed at every time point of the neutrophil-TM interaction and compared between isotype and LFA-1 inhibited groups (n = 5/4 mice for isotype/LFA-1 groups)
B. Duration of neutrophil-TM interaction was visually analyzed interaction and compared between isotype and LFA-1 inhibited groups (n = 5/4 mice for isotype/LFA-1 groups)

In the control situation, number of neutrophils in the direct vicinity of the LI (laser injury) never surpassed that of those in the complete area at large. They reached their peak at 3 hours after laser injury and were then cleared away by the 4th hour back to steady-state levels. On the other hand, when TM-neutrophil contact was abrogated by an LFA-1 antagonist, the number of neutrophils in direct vicinity of the LI surpassed that of those in the area at large, showing a higher TFI, and continued to do so until the 5th hour (**Figure 59a**). This shows a causal connection between failure to limit neutrophils influx to the LI and abrogation of TM-neutrophil contact. The total number of neutrophils in the region of interest was not significantly different in isotype and treated mice (**Figure 59b**).
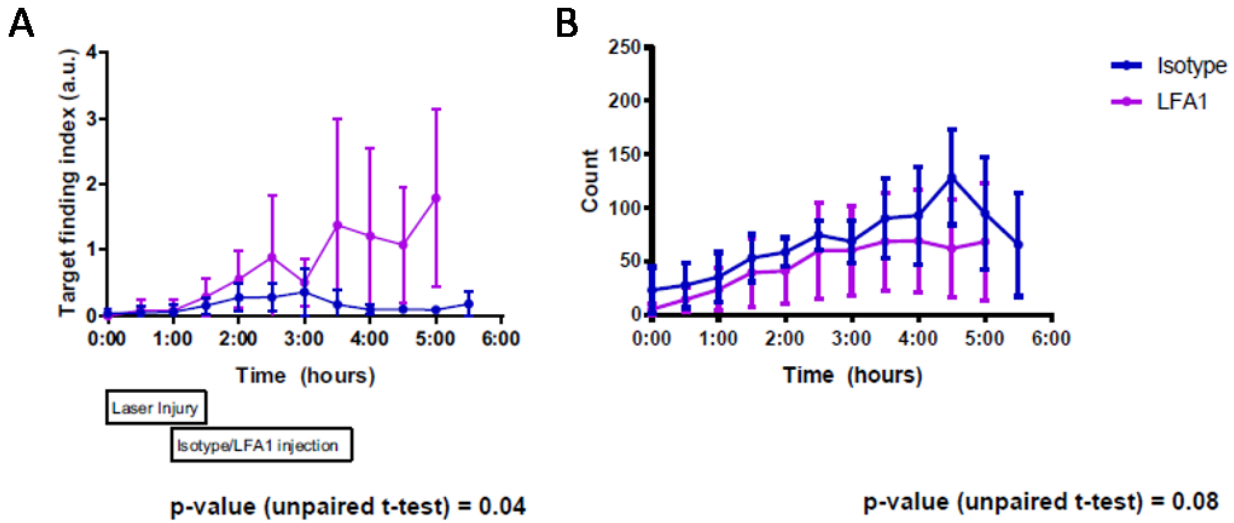
Figure 59: Target finding index and number of neutrophils per FoV in control and LFA-1 inhibited neutrophils

C. Neutrophil target finding index in the presence of a laser injury in the ear model of CX3CR1eGFP mice is analyzed over 5 hours upon intradermal injection of isotype antibody and LFA-1 inhibitor. LFA-1 inhibition results in higher proportion of neutrophils flocking to the tissue necrosis site (n = 5 mice).

D. The total number of neutrophils present in the field of view was not significantly different in isotype antibody treated and LFA-1 inhibited mice (n = 5 mice).

In congruous fashion to the analysis of the number of neutrophils, neutrophils in control mice stayed on average at a distance of 200 µm from the lesion site whereas those in LFA-1 treated mice migrated towards the LI over time averaging out at about 50 µm during the last couple hours of imaging (**Figure 60**).
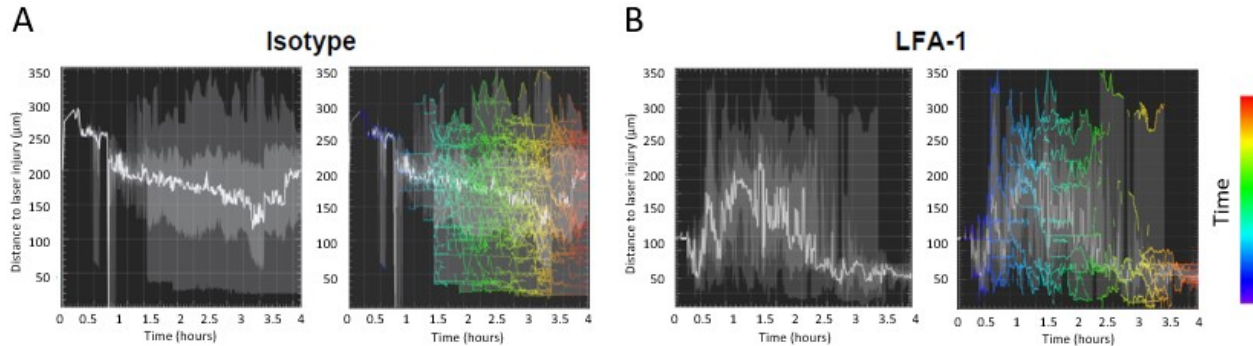
Figure 60: Migration of neutrophils to focal necrosis in control and LFA-1 inhibitor treated CX3CR1eGFP mice

A. **Left**: Interstitial migration of neutrophils towards the tissue necrosis site in the ear model of isotype antibody-treated mice is shown by a representative tracing of the average distance (white line) from the laser injury over 4 hours of migration. The dark-grey shades show the extent of the closest and farthest neutrophils from the lesion site while the light-grey shades represent the SEM. **Right**: Individual neutrophil tracks (pseudocolored for time) are superposed on the image on the left side.

B. Similar representative tracing as in A of the average neutrophil distance from the laser injury in LFA-1 inhibitor-treated mice shows a smaller distance to site of tissue necrosis site after 4 hours of migration.

Despite LFA-1's role in neutrophils, we did not notice changes in neutrophil activation in terms of calcium signal intensity across all stages between control and treated neutrophils (**Figure 61**). However, LFA-1 inhibition resulted in a significant shift to shorter transients before and during interaction and a significant PSD reduction after interaction in neutrophils (**Figure 62**). In summary, these data indicate that dendrite-forming TMs reprogram neutrophils through direct contacts, resulting in the limitation of neutrophil influx in sterile inflammation

.
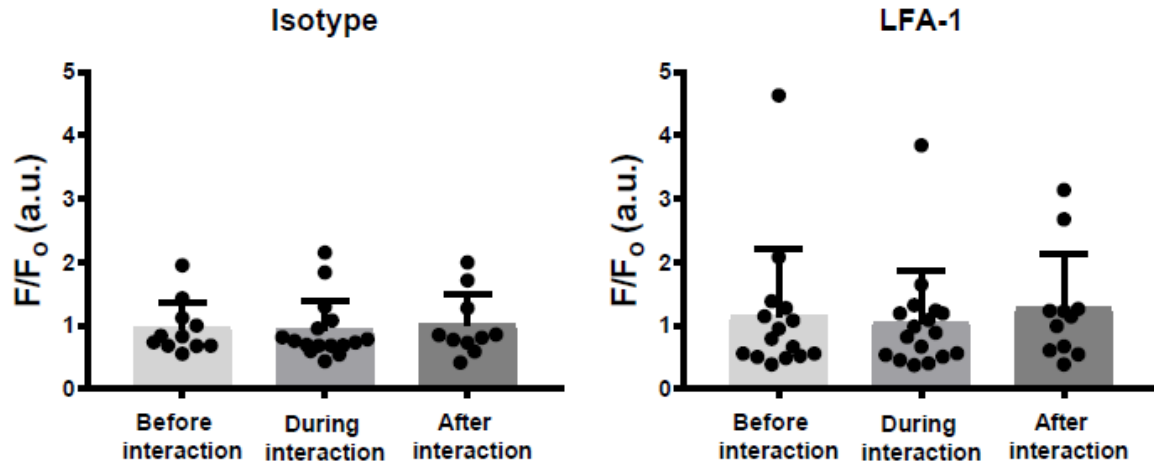
Figure 61: Ca^{++} average intensity in neutrophils across interaction stages is not affected by HMGB1

The Ca^{++}-signal average intensity of neutrophils that interact with TMs during interstitial migration was analyzed before, during, and after interaction in the ear model of LysMCre-PCGtTflox in Cx3cr1eGFP chimera mice upon intradermal injection of isotype antibody (**left**) and LFA-1 inhibitor (**right**). No significant effect was observed (n = 5 mice).
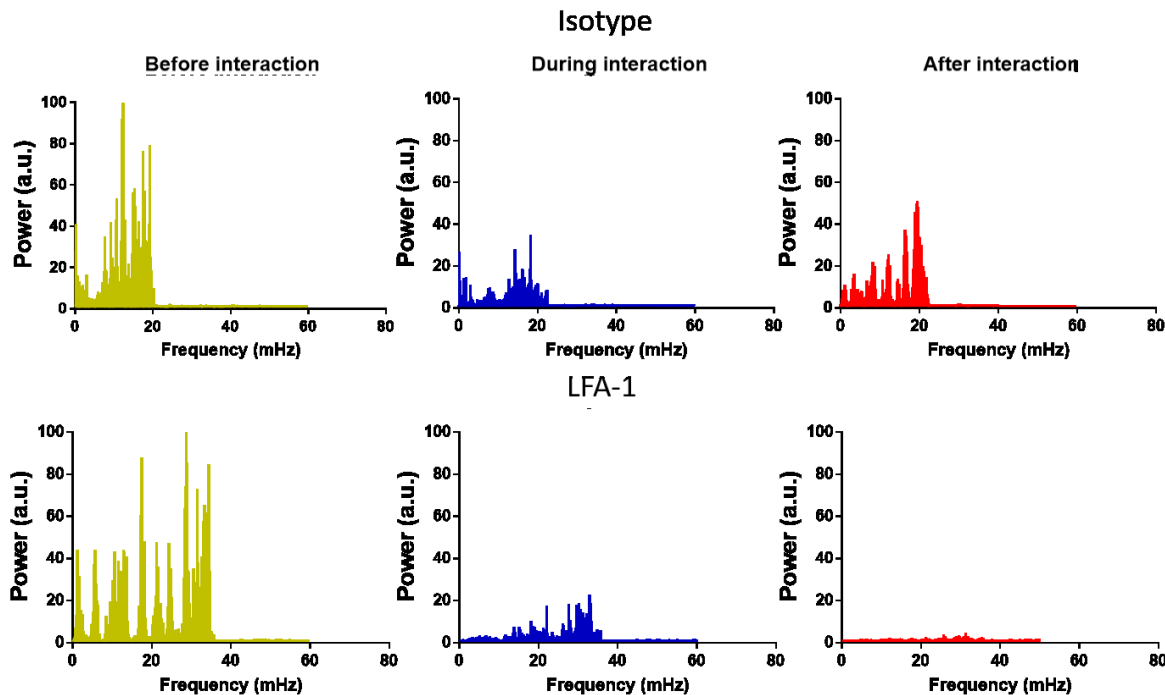
Figure 62: PSD across interaction stages in control versus LFA-1 inhibited neutrophils

The Ca^{++}-signal PSD of neutrophils that interact with TMs during interstitial migration was analyzed before, during, and after interaction in the ear model of LysMCre-PCGtTflox in Cx3cr1eGFP chimera mice upon intradermal injection of isotype antibody (**top**) and LFA-1 inhibitor (**bottom**). The PSD values were normalized to 100 with all 6 groups taken into consideration (n = 5 mice).

4. Discussion

4.1 Novel Ca^{++} signaling analysis uncovers immune cellular functional states

The current knowledge about Ca^{++} signaling in myeloid leukocytes encompasses mainly dye-loaded cellular *in vitro* imaging techniques. *In vivo* imaging of transgenic Ca^{++} reporter mouse strains allows us here to capture Ca^{++} oscillations in TMs following sterile injury and unique signal patterns in neutrophils for each migration cascade step. Having looked at the first layer of Ca^{++} signaling in neutrophils, we confirm the involvement of Gαi-PCRs in neutrophil activation during the migration cascade. These findings are based on classical Ca^{++} signaling parameters being coupled to the comprehensive spectral method for assessment of Ca^{++} complex signals *in vivo*.

The cre-dependent GCaMP5G-IRES-tdTomato reporter mouse was used *in vivo* by (Gee et al. 2014) in neurons and glial cells (Gee et al. 2014). They used the constitutive tdTomato signal as an indicator for cells that expressed low Ca^{++} signals. Similarly, we were able to replicate this for our LysMCre and CX3CR1Cre constructs in neutrophils and macrophages. Different cell types employ Ca^{++} signaling at various ranges of frequencies: dorsal root ganglion neurons are known to operate in the frequency range of 200 – 2000 mHz, whereas immune cells such as T lymphocytes operate at a much lower frequency range of 0.5 – 200 mHz (Smedler and Uhlen 2014). Correspondingly, the GCaMP5G-IRES-tdTomato reporter mouse enables the detection of Ca^{++} oscillations in TMs and neutrophils in the migration cascade *in vivo* covering 20 – 40 mHz and 20 – 150 mHz, respectively.

(Gee et al. 2014) focused on normalized signal intensity, number of spikes, and frequency evaluated as number of spikes per minute for their analysis of Ca^{++} signals and their dynamics, as does the overwhelming majority of the *in vitro* and *in vivo* Ca^{++} signaling data out there (Gee et al. 2014). However, these classical parameters do not capture the full complexity of highly irregular *in vivo* Ca^{++} signals. One can overcome this limitation by spectral analysis of Ca^{++} signal oscillations. The spectral method makes use of the normalized signal intensity to transition from the time domain into the frequency domain by Fourier transformation. The PSD is a representation of one frequency's power in a spectrum relative to the combined power of all other frequencies, hence also referred to as relative power. Power is a measure of the squared amplitude of the signal and hence also a potential measure of cellular activation. Therefore, PSD-vs-frequency graphs primarily reveal the order of significance of a signal's frequencies and secondarily hint at a signal's amplitude and activation. It is evident from PSDs that there are a multitude of frequency values above the noise threshold, pointing out that Ca^{++} signals *in vivo* are not just a mere one-

frequency phenomenon but rather made of multiple frequencies that would be difficult to pick out from the time domain. Therefore, the spectral method has an advantage over the classical events per minute analysis because it offers insight into a broad range of frequency values as opposed to just one value.

Combining this new method with *in vivo* imaging models brings an added layer of complexity to what would have been achieved with *in vitro* systems. Although not discounting the novelty the spectral method would bring to classic *in vitro* systems, the ability to analyze activation of immune cells in different original disease states adds to the credibility of the results.

TMs have been shown to carry out immune functions of endocytosis and phagocytosis of bacterial infection debris in a Ca^{++}-dependent manner (Zhou et al. 2018). We therefore wanted to explore if this was also the case during non-pathogenic tissue damage and found that macrophage Ca^{++} signal intensity was significantly raised after induction of a sterile inflammation by a laser injury. Moreover, Ca^{++} signal analysis allowed us to uncover that immotile TMs closer to the center of necrosis were activated earlier und more intensively. This could be due to the high gradient of DAMPs in the vicinity of the necrotic area.

In contrast, neutrophils expose a different Ca^{++} signal pattern: (Beerman et al. 2015) showed that during migration of neutrophils in zebrafish towards a tissue injury, the leading edge has the highest Ca^{++} signal intensity, as is the case with our study of neutrophils during transmigration and interstitial migration in mice (Beerman et al. 2015). This cell context-dependent variability in the range of intracellular Ca^{++} spikes has been shown as a way in which cells encode different types of stimuli (Thurley et al. 2014). Comparably, we have shown that neutrophils produce starkly different frequency signatures depending on the stage of the cascade as well as while executing effector functions at the site of necrosis, adding to the notion that Ca^{++} signal spectra reflect different functional states.

It is known that PTx has an effect on Gαi-PCRs to inhibit intracellular Ca^{++} signaling in myeloid leukocytes and thereby their chemotactic response, but how Ca^{++} signals are affected *in vivo* is unclear (Goldman et al. 1985), (Zou et al. 2012), (Spangrude et al. 1985). Gαi-PCRs have been found to work with CRAC channels to trigger intracellular Ca^{++} flux resulting in the arrest and polarization of neutrophils (Schaff et al. 2010). Furthermore, Ca^{++} flux has been demonstrated to affect neutrophil arrest by initiating LFA-1 clustering (Dixit et al. 2012). We therefore chose PTx as a proven Ca^{++} signaling antagonist to highlight our novel *in vivo* Ca^{++} signaling characterization method.

Ca^{++} signaling is an inherent part of the neutrophil recruitment cascade as myeloid leukocytes leave the vasculature and arrive at a target site. Outside-in signaling mechanisms, which are responsible for leukocyte rolling and arrest, depend on $G\alpha i$-PCRs (Ley et al. 2007), (Nourshargh, Hordijk, and Sixt 2010). Correspondingly, we show the PSD of rolling gets immensely reduced upon PTx treatment whereas the successive stages are not affected. During rolling, intracellular Ca^{++} stores from the ER are released into the cytoplasm through other receptor pathways. With $G\alpha i$-PCR uninhibited, this small intracellular surge would in turn create a bigger influx of Ca^{++} ions from the outside. We therefore observe an overall reduced intracellular Ca^{++} signal intensity with PTx treatment. Moreover, this lack of constant influx and efflux results in very small intracellular concentration changes over time, which is reflected by the small amplitude. $G\alpha i$-PCR inhibition's lack of effect on migratory or Ca^{++} signaling parameters during adhesion and transmigration can be explained by the involvement of other intracellular Ca^{++} regulation mechanisms like SOCE- and ORAI-mediated Ca^{++} uptake and release during these stages of the cascade. This also explains why there is no clear interdependence between Ca^{++} signaling and speed or direction change and shows the complexity to correlate such parameters. Where the classical normalized intensity parameter fails to show the significance of the reduction in activation during rolling, the novel PSD shows $G\alpha i$-PCRs affect Ca-signal spectra in neutrophils *in vivo*.

With the spectral method of investigating Ca^{++} dynamics *in vivo*, we show a comprehensive way of assessing leukocyte activation. Coupled to the Cre-lox recombination system that allows the GCaMP5G-IRES-tdTomato reporter to be expressed in any cell line, a plethora of opportunities open up for novel *in vitro* and *in vivo* Ca^{++} signal-based activation characterizations. Ca^{++} signaling has been tapped before as a key mechanism to interfere with the fight against various autoimmune and inflammatory immune disease (Feske 2007). Our approach adds to this effort by establishing new opportunities to analyze reactions of leukocytes – or any immune cells thanks to the ubiquitous nature of Ca^{++} signaling – to therapeutic interventions *in vivo*. This opens up novel ways of analyzing leukocytes *in vivo* but also warrants the need for linking different Ca^{++} flux-signatures with distinct cellular programs.

4.2 Interstitial macrophages limit detrimental neutrophil accumulation via the HMGB1-TLR4 dependent dendrite formation and LFA-1 mediated contacts

The role of neutrophils and TMs in sterile and pathogenic inflammation settings has been the point of investigation of several studies (Foss, Sanchez-Bautista, and Jain 2018), (Oishi and Manabe 2018), (Kolaczkowska and Kubes 2013). In both cases, unabated neutrophil swarming to site of necrosis or pathogens has been shown to bring about detrimental results to the underlying tissue by production of ROS (Serhan and Levy 2018). Park et al. intradermally injected GFP$^+$ neutrophils into the ear of a Black 6 mouse and studied their response to a macrolesion induced by phototoxicity (Park et al. 2018). They found higher numbers of apoptotic neutrophils in the tissue to correspond to more severe tissue damage. In another case of sterile laser injuries, Uderhardt et al. induced phototoxic microlesions in the peritoneum serosa of LysM-GFP mice (Uderhardt et al. 2019). They showed that depending on the smallness of the injury, resident TMs in it is vicinity extend their dendrites to fully cloak the microlesion and shield it from any neutrophil swarming. By doing so, neutrophil-mediated inflammation is prevented thereby protecting the tissue from degradation. But once the injury size crosses a certain threshold, the macrolesion proves too big for the dendrites to fully cloak it leading to prolonged neutrophil swarming. Similarly, we created skin necrosis sites in the range of macrolesions, but did not notice cloaking.

Studies have shown lesions to be the source of DAMP release as a result of necrotic cells at the lesions releasing them (Einhorn and Gerstenfeld 2015). These mediators are believed to decrease in a gradient as one travels away from the source of necrosis. Furthermore, neutrophils have been shown to be first responders in sterile inflammation and undergo apoptotic processes at the lesion site releasing chemoattractant and proinflammatory molecules (Lammermann et al. 2013), (Ng et al. 2011). In congruence to the fact that lesion sites are sources of cytokine release and the highest point of the cytokine gradient, we noticed neutrophils became more activated upon arrival at the lesion site. They were immobilized at the site and exposed heightened Ca^{++} signal frequencies. In addition, these Ca^{++} signal transients were sustained for longer periods. Sustained Ca^{++} signals are a sign of heightened cellular activity made possible by release of intracellular Ca^{++} stores and opening of ion channels for Ca^{++} influx. In this specific scenario, neutrophils might attain this heightened state just before undergoing apoptosis enabling them to release copious amounts of cytokines driving neutrophil swarming.

We noticed, however, that neutrophil swarming did not go on unabated. There is a mechanism in place that prevents neutrophils from continually swarming the lesion site. This mechanism involves dendrite formation by TMs and these dendrites forming lengthy contacts with lesion-bound

neutrophils. Interestingly, it comes into effect only about 2 hours on average after tissue insult via laser injury giving neutrophils time to first carry out their inflammatory effector functions.

Furthermore, because pathogens have also been shown to lead to inflammation in the skin, we also investigated dendrite formation in TMs in the presence of E. coli. To do this, we intradermally injected E. coli and PBS and compared dendrite formation. Similar to sterile inflammation, the bacteria caused TM dendrite formation in analogous temporal dynamics. In summary, dendrite formation in TMs plays a crucial anti-inflammatory effect reversing the inflammatory cascade of events that is kicked off by neutrophils in both sterile and microbial inflammations.

Having uncovered that TM dendrite interaction with neutrophils induces anti-inflammatory effects that drive neutrophils away from the lesion site, we carried out proof-of-principle experiment. In this experiment, we investigated a model where TMs are not in play. In order to do that, CX3CR1eGFP mice were fed a macrophage-depleting diet that led to TM depletion by more than half. TM reduction had no effect on the total number of neutrophils recruited but it significantly augmented neutrophil target finding behavior. This provides even more proof that TMs play an important role in limiting neutrophil-caused damage at the site of lesion by physically reprogramming them to alter their pro-inflammatory effects.

Because we observed from the migration parameters that interaction between neutrophils and TM dendrites lead to functional changes at the cell population and single cell levels, we next asked if these alterations are also reflected in their Ca^{++} signals. What we found were surprisingly insignificant changes in normalized intensity, amplitude and dominant frequency in different stages of interaction. But PSD analysis of the interaction stages tell a story more in line with the migration parameters: TM Ca^{++} signal power is elevated after interaction while that of neutrophils decreases upon interaction and remains low after interaction. Elevated PSD indicates higher amplitude, in turn meaning bigger area under the curve which also means higher intracellular Ca^{++} concentration. This effectively translates to TM activation and neutrophil de-activation after interaction which goes hand in hand with neutrophils being deflected away by TM dendrites from their pro-inflammatory duties thereby promoting inflammation resolution. This analysis is another example that shows the superiority of the PSD analysis to the classical one.

Because we observed that neutrophils form cell-cell contacts with TMs and other neutrophils, we next asked if neutrophils had effects on TM dendrite formation beyond chemokine release and possibly through cell-cell contacts as they continually probed the tissue area adjacent to the lesion site. To do that, we depleted neutrophils in CX3CR1eGFP mice, placed a laser injury in the dermis and observed TM dendrite formation. Interestingly, this led to a much-hastened dendrite formation

albeit plateauing out at a moderately smaller proportion than isotype treated mice. Coupled to dendrites deflecting neutrophils away from the lesion site, this shows that neutrophils exert physical anti-dendrite formation effects on TMs that in turn allows them to employ their proinflammatory effector functions at the lesion site during the initiation of inflammation and swarming.

To understand the mechanisms underlying dendrite formation in TMs, we first looked at the CX3CR1-CX3CL1 axis. However, dendrite formation in TMs happens independently of the CX3CR1-CX3CL1 interaction. The next mechanistic approach we investigated was HMGB1's role in dendrite formation. To investigate the involvement of HMGB1 in dendrite formation, we injected Box-A intradermally in CX3CR1eGFP mice and introduced a laser injury. The result was a delayed onset of dendrite formation and a smaller proportion of dendrite forming TMs, confirming the involvement of HMGB1 in TM dendrite formation.

RAGE and TLR4 are two important receptors that mediate macrophage and neutrophil responses to inflammatory cues and interaction with other immune cells (Wang et al. 2017), (McDonald et al. 2013). Moreover, RAGE signaling has been implicated in macrophage disorder during wound healing (Wang et al. 2017). We next analyzed the mechanistic basis of TM dendrite formation by blocking these two receptors. For this purpose, we intradermally injected RAP – RAGE antagonist peptide – and C34 – TLR4 inhibitor – and introduced a laser injury (Arumugam et al. 2012), (Wipf et al. 2015). Compared to PBS injected control mice, only those that received C34 showed a reduced proportion of dendrite forming TMs while the onset of dendrite formation was unaffected. TLR4 is therefore the receptor with which TMs sense HMGB1, resulting in dendrite formation.

We continued by investigating the mechanistic background of this contact-based swarming cessation on the neutrophil side. For this reason, we chose to investigate LFA-1 as it has been shown to be one of the ways neutrophils interact with TMs. Indeed, our experiments showed that neutrophil-TM interaction is mediated by LFA-1. Much like the high affinity conformation the integrin LFA-1 adopts on endothelial surfaces to initiate adhesion (Lefort and Ley 2012), we speculate that LFA-1 also undergoes similar conformational changes that allow interactions with TMs. Although other docking mechanisms cannot be counted out, the dramatic drop in neutrophil-TM interaction time and increase in neutrophil flux to lesion site upon LFA-1 inhibition point to a central role of LFA-1 in this interaction. When LFA-1 is blocked, other chemotactic receptors like Gαi-PCR and formyl peptide receptors take over maneuvering the neutrophil in the direction of increasing chemokine gradient.

4.3 Outlook

The Ca^{++} signaling analysis algorithm that is presented in this thesis opens up the opportunity to look at many more cell types than neutrophils and TMs in their native environments. This can be done not only in settings of sterile and microbial inflammation, but in also to answer any other biologically relevant question as long as one can create the necessary setting in the proper Ca^{++} reporter mouse strain. The strength of this analysis technique lies in the endogenous labeling of Ca^{++}, getting rid of the need for dyes to label Ca^{++} signaling. In order for this intravital analysis technique to work, one needs to get hold of equipment like 2P-IVM and SDCM. Although there are new advancements resulting in GCaMP fusions with stronger fluorescence that may facilitate a more universal use of this tool (Chen et al. 2013). The most recent versions of the protein fusion, namely GCaMP6f and GCaMP7f, boost Ca^{++} signal intensity more than 3 times that of GCaMP5g and half-decay times of 140 ± 430 ms and 265 ± 20 ms, respectively (Dana et al. 2019).

There is a sizable amount of literature that points out to the involvement of neutrophils and TMs in the resolution of inflammation. This work supports those findings and furthermore provides a new angle to assess the cellular interplay that is at work. It would be important to use the Ca^{++} signal analysis tool to investigate other cells that may be taking part in this intricate relationship. More specifically, one could look at the involvement of platelets in the vasculature during the migration cascade as they have been previously shown to support neutrophil transmigration into inflamed and infected tissues (Pitchford, Pan, and Welch 2017). In the inflamed tissue, neutrophils are known to mediate monocyte recruitment and thereby also contribute to resolution (Soehnlein, Lindbom, and Weber 2009). It would therefore also make sense to investigate monocyte Ca^{++} signaling during their interaction with neutrophils in order to figure out the underlying mechanisms for resolution.

Finally, and most importantly, discoveries based on this analysis tool can lead to therapeutics that target either Ca^{++} channels or mechanisms of cellular interactions. Studies have already shown the potential of targeting the Ca^{++} interactome in cancer therapeutics, hemodialysis and prevention of various neuropathy types (Bong and Monteith 2018), (Aniort, Chupin, and Cindea 2018), (Boeckel and Ehrlich 2018). There have also been anti-Ca^{++} channel therapies developed for the treatment of autoimmune and inflammatory diseases (Vaeth and Feske 2018). Therefore, further research in the field of Ca^{++} signaling therapeutics will benefit from added insight from the new analysis tool.

5. Summary

5.1 Ca^{++} signaling analysis in myeloid leukocytes

Assessment of leukocyte activation *in vivo* is limited so far to surrogate parameters like shape change and migration patterns. Consequently, the complex spatiotemporal activation of leukocytes during inflammation remains incompletely understood. Here, we show that intravital microscopy of leukocyte Ca^{++} signals using Ca^{++} reporter strains provides a new tool to assess myeloid leukocyte activation *in vivo*. We demonstrate by 2-photon microscopy that macrophages react to sterile inflammation by Ca^{++} transients in a distinct spatiotemporal pattern. Moreover, using high-resolution intravital spinning disk confocal microscopy, we uncover intracellular Ca^{++} dynamics of neutrophils during the migration cascade *in vivo*, which depend on Gαi-protein-coupled receptors. This is based on the analysis of frequency spectra providing comprehensive insights into complex and highly irregular leukocyte Ca^{++} oscillations. Therefore, we establish Ca^{++} frequency spectra as an additional dimension to assess leukocyte activation during inflammation *in vivo* (**Figure 63**).
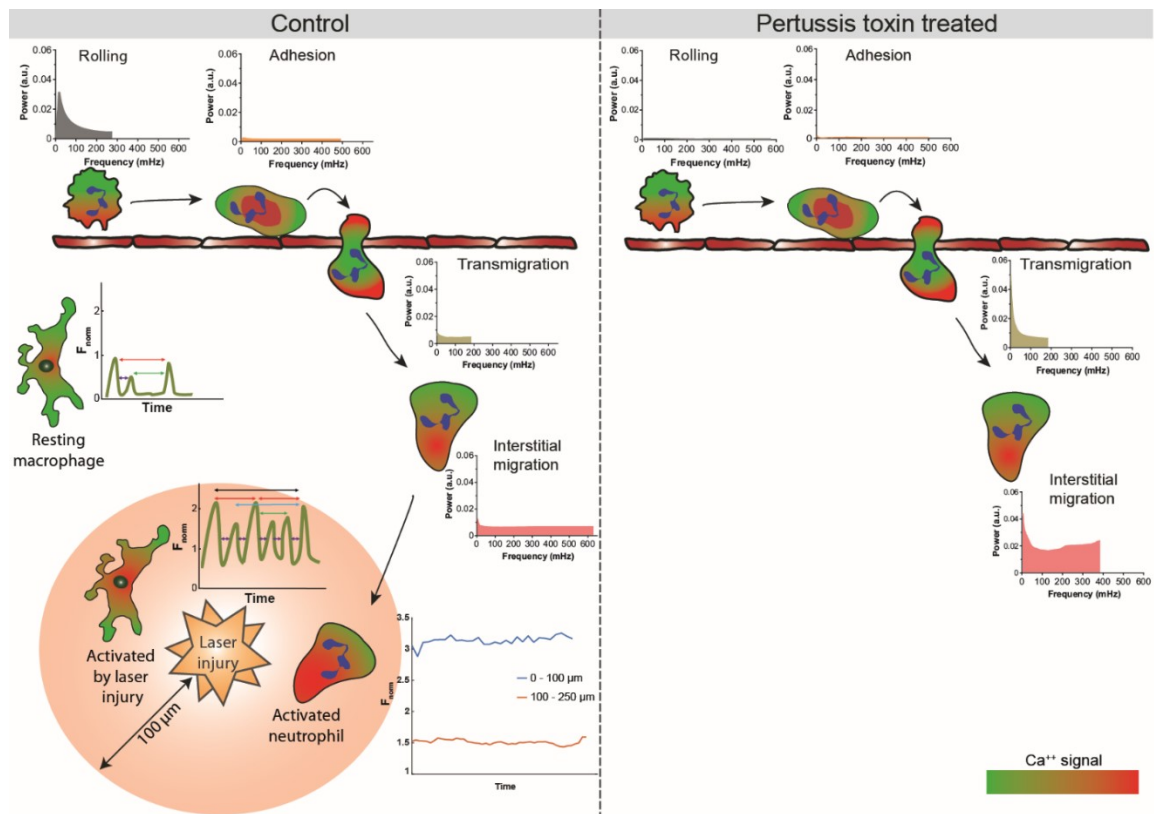
Figure 63: Summary I – Ca^{++} signaling as a parameter in leukocyte assessment

An overview scheme depicting how Ca^{++} signaling can be used to depict *in vivo* cellular activation in TMs and neutrophils by laser injury or signaling pathway blockage.

5.2 Inflammation limitation

The recruitment of neutrophils to a macrolesion in the mouse skin ear model ends after a certain time. Dendrite formation by TMs correlates with the ending of neutrophil influx. Neutrophils are also observed forming cell-cell contacts with these dendrite forming TM. Furthermore, depletion of TMs results in prolonged influx of neutrophils to the macrolesion. We see that interaction between neutrophils and dendrite forming TMs has an impact on the single-cell level and is reflected by changes in the calcium frequency spectrum. We identified disulfide HMGB1-TLR4 interaction as the mechanism of dendrite formation. Interstitial inhibition of LFA-1 results in prolonged neutrophil influx and altered neutrophil activity during and after interaction with TMs suggesting the interaction depends on LFA-1 (**Figure 64**).
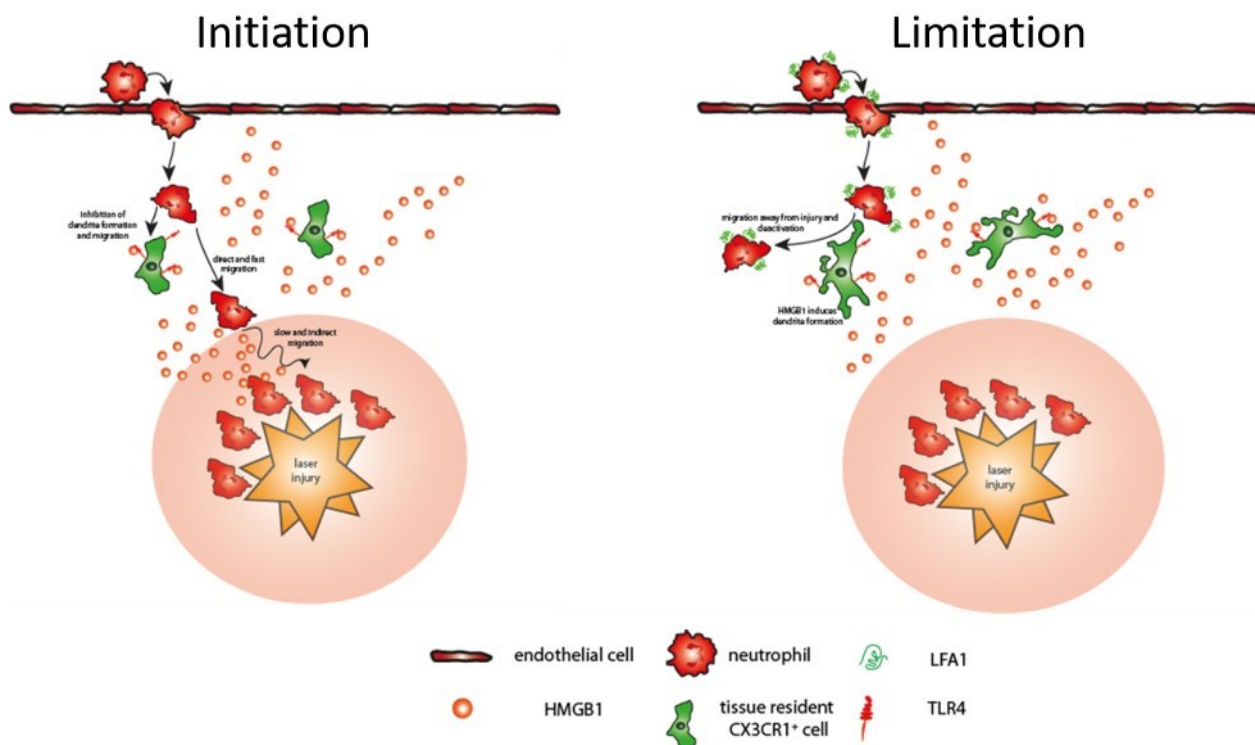
Figure 64: Summary II – Dendrite formation in TMs leads to resolution of neutrophil-induced inflammation

Laser injury in the skin gets swarmed by neutrophils until HMGB1-TLR4 dependent dendrite formation in TMs facilitates resolution via contact reprogramming of neutrophils mediated by LFA1.

References

Abdul Hamid, A. I., L. Nakusi, M. Givskov, Y. T. Chang, C. Marques, and P. Gueirard. 2020. 'A mouse ear skin model to study the dynamics of innate immune responses against Staphylococcus aureus biofilms', *BMC Microbiol*, 20: 22.

Acharya, M. M., K. N. Green, B. D. Allen, A. R. Najafi, A. Syage, H. Minasyan, M. T. Le, T. Kawashita, E. Giedzinski, V. K. Parihar, B. L. West, J. E. Baulch, and C. L. Limoli. 2016. 'Elimination of microglia improves cognitive function following cranial irradiation', *Sci Rep*, 6: 31545.

Aikawa, N. 1996. '[Cytokine storm in the pathogenesis of multiple organ dysfunction syndrome associated with surgical insults]', *Nihon Geka Gakkai Zasshi*, 97: 771-7.

Akerboom, J., T. W. Chen, T. J. Wardill, L. Tian, J. S. Marvin, S. Mutlu, N. C. Calderon, F. Esposti, B. G. Borghuis, X. R. Sun, A. Gordus, M. B. Orger, R. Portugues, F. Engert, J. J. Macklin, A. Filosa, A. Aggarwal, R. A. Kerr, R. Takagi, S. Kracun, E. Shigetomi, B. S. Khakh, H. Baier, L. Lagnado, S. S. Wang, C. I. Bargmann, B. E. Kimmel, V. Jayaraman, K. Svoboda, D. S. Kim, E. R. Schreiter, and L. L. Looger. 2012. 'Optimization of a GCaMP calcium indicator for neural activity imaging', *J Neurosci*, 32: 13819-40.

Akerboom, J., J. D. Rivera, M. M. Guilbe, E. C. Malave, H. H. Hernandez, L. Tian, S. A. Hires, J. S. Marvin, L. L. Looger, and E. R. Schreiter. 2009. 'Crystal structures of the GCaMP calcium sensor reveal the mechanism of fluorescence signal change and aid rational design', *J Biol Chem*, 284: 6455-64.

Amarante-Mendes, G. P., S. Adjemian, L. M. Branco, L. C. Zanetti, R. Weinlich, and K. R. Bortoluci. 2018. 'Pattern Recognition Receptors and the Host Cell Death Molecular Machinery', *Front Immunol*, 9: 2379.

Aniort, J., L. Chupin, and N. Cindea. 2018. 'Mathematical model of calcium exchange during haemodialysis using a citrate containing dialysate', *Math Med Biol*, 35: 87-120.

Arumugam, T., V. Ramachandran, S. B. Gomez, A. M. Schmidt, and C. D. Logsdon. 2012. 'S100P-derived RAGE antagonistic peptide reduces tumor growth and metastasis', *Clin Cancer Res*, 18: 4356-64.

Baez, S. 1973. 'An open cremaster muscle preparation for the study of blood vessels by in vivo microscopy', *Microvasc Res*, 5: 384-94.

Beerman, R. W., M. A. Matty, G. G. Au, L. L. Looger, K. R. Choudhury, P. J. Keller, and D. M. Tobin. 2015. 'Direct In Vivo Manipulation and Imaging of Calcium Transients in Neutrophils Identify a Critical Role for Leading-Edge Calcium Flux', *Cell Rep*, 13: 2107-17.

Beltman, J. B., A. F. Maree, and R. J. de Boer. 2009. 'Analysing immune cell migration', *Nat Rev Immunol*, 9: 789-98.

References

Benhamou, S. 2004. 'How to reliably estimate the tortuosity of an animal's path: straightness, sinuosity, or fractal dimension?', *J Theor Biol*, 229: 209-20.

Benninger, R. K., and D. W. Piston. 2013. 'Two-photon excitation microscopy for the study of living cells and tissues', *Curr Protoc Cell Biol*, Chapter 4: Unit 4 11 1-24.

Benzaquen, L. R., C. Brugnara, H. R. Byers, S. Gatton-Celli, and J. A. Halperin. 1995. 'Clotrimazole inhibits cell proliferation in vitro and in vivo', *Nat Med*, 1: 534-40.

Berridge, M. J., P. Lipp, and M. D. Bootman. 2000. 'The versatility and universality of calcium signalling', *Nat Rev Mol Cell Biol*, 1: 11-21.

Boda, Annegret Mina-Sophia. 2019. 'Interaktion von gewebsständigen CX3CR1+-Zellen mit neutrophilen Granulozyten bei steriler Inflammation in vivo', Ludwig-Maximilians University Munich.

Boeckel, G. R., and B. E. Ehrlich. 2018. 'NCS-1 is a regulator of calcium signaling in health and disease', *Biochim Biophys Acta Mol Cell Res*, 1865: 1660-67.

Bong, A. H. L., and G. R. Monteith. 2018. 'Calcium signaling and the therapeutic targeting of cancer cells', *Biochim Biophys Acta Mol Cell Res*, 1865: 1786-94.

Bouchery, T., and N. Harris. 2019. 'Neutrophil-macrophage cooperation and its impact on tissue repair', *Immunol Cell Biol*, 97: 289-98.

Buckley, C. D., E. A. Ross, H. M. McGettrick, C. E. Osborne, O. Haworth, C. Schmutz, P. C. Stone, M. Salmon, N. M. Matharu, R. K. Vohra, G. B. Nash, and G. E. Rainger. 2006. 'Identification of a phenotypically and functionally distinct population of long-lived neutrophils in a model of reverse endothelial migration', *J Leukoc Biol*, 79: 303-11.

Buonanno, A., and R. D. Fields. 1999. 'Gene regulation by patterned electrical activity during neural and skeletal muscle development', *Curr Opin Neurobiol*, 9: 110-20.

Carey, M. B., and S. G. Matsumoto. 1999. 'Spontaneous calcium transients are required for neuronal differentiation of murine neural crest', *Dev Biol*, 215: 298-313.

Chang, Y. C., M. Soriano, R. A. Hahn, R. P. Casillas, M. K. Gordon, J. D. Laskin, and D. R. Gerecke. 2018. 'Expression of cytokines and chemokines in mouse skin treated with sulfur mustard', *Toxicol Appl Pharmacol*, 355: 52-59.

Chen, G. Y., and G. Nunez. 2010. 'Sterile inflammation: sensing and reacting to damage', *Nat Rev Immunol*, 10: 826-37.

Chen, T. W., T. J. Wardill, Y. Sun, S. R. Pulver, S. L. Renninger, A. Baohan, E. R. Schreiter, R. A. Kerr, M. B. Orger, V. Jayaraman, L. L. Looger, K. Svoboda, and D. S. Kim. 2013. 'Ultrasensitive fluorescent proteins for imaging neuronal activity', *Nature*, 499: 295-300.

References

Conchello, J. A., and J. W. Lichtman. 2005. 'Optical sectioning microscopy', *Nat Methods*, 2: 920-31.

Crabtree, G. R. 1999. 'Generic signals and specific outcomes: signaling through Ca2+, calcineurin, and NF-AT', *Cell*, 96: 611-4.

Dal Santo, P., M. A. Logan, A. D. Chisholm, and E. M. Jorgensen. 1999. 'The inositol trisphosphate receptor regulates a 50-second behavioral rhythm in C. elegans', *Cell*, 98: 757-67.

Dalal, P. J., D. P. Sullivan, E. W. Weber, D. B. Sacks, M. Gunzer, I. M. Grumbach, J. Heller Brown, and W. A. Muller. 2021. 'Spatiotemporal restriction of endothelial cell calcium signaling is required during leukocyte transmigration', *J Exp Med*, 218.

Dana, H., Y. Sun, B. Mohar, B. K. Hulse, A. M. Kerlin, J. P. Hasseman, G. Tsegaye, A. Tsang, A. Wong, R. Patel, J. J. Macklin, Y. Chen, A. Konnerth, V. Jayaraman, L. L. Looger, E. R. Schreiter, K. Svoboda, and D. S. Kim. 2019. 'High-performance calcium sensors for imaging activity in neuronal populations and microcompartments', *Nat Methods*, 16: 649-57.

de Oliveira, S., E. E. Rosowski, and A. Huttenlocher. 2016. 'Neutrophil migration in infection and wound repair: going forward in reverse', *Nat Rev Immunol*, 16: 378-91.

de Seabra Rodrigues Dias, I. R., S. W. F. Mok, F. Gordillo-Martinez, I. Khan, W. W. L. Hsiao, B. Y. K. Law, V. K. W. Wong, and L. Liu. 2017. 'The Calcium-Induced Regulation in the Molecular and Transcriptional Circuitry of Human Inflammatory Response and Autoimmunity', *Front Pharmacol*, 8: 962.

Deroubaix, A., B. Moahla, and C. Penny. 2020. 'Monitoring of intracellular localization of Hepatitis B virus P22 protein using Laser Scanning Confocal Microscopy and Airyscan', *Microsc Res Tech*, 83: 499-506.

Ding, Z. M., J. E. Babensee, S. I. Simon, H. Lu, J. L. Perrard, D. C. Bullard, X. Y. Dai, S. K. Bromley, M. L. Dustin, M. L. Entman, C. W. Smith, and C. M. Ballantyne. 1999. 'Relative contribution of LFA-1 and Mac-1 to neutrophil adhesion and migration', *J Immunol*, 163: 5029-38.

Dixit, N., M. H. Kim, J. Rossaint, I. Yamayoshi, A. Zarbock, and S. I. Simon. 2012. 'Leukocyte function antigen-1, kindlin-3, and calcium flux orchestrate neutrophil recruitment during inflammation', *J Immunol*, 189: 5954-64.

Duchen, M. R. 2000. 'Mitochondria and calcium: from cell signalling to cell death', *J Physiol*, 529 Pt 1: 57-68.

Einhorn, T. A., and L. C. Gerstenfeld. 2015. 'Fracture healing: mechanisms and interventions', *Nat Rev Rheumatol*, 11: 45-54.

References

Eisner, D. A., and A. W. Trafford. 1996. 'A sideways look at sparks, quarks, puffs and blips', *J Physiol*, 497 (Pt 1): 2.

Fan, Z., and K. Ley. 2015. 'Leukocyte arrest: Biomechanics and molecular mechanisms of beta2 integrin activation', *Biorheology*, 52: 353-77.

Faust, N., F. Varas, L. M. Kelly, S. Heck, and T. Graf. 2000. 'Insertion of enhanced green fluorescent protein into the lysozyme gene creates mice with green fluorescent granulocytes and macrophages', *Blood*, 96: 719-26.

Ferrari, M. B., K. Ribbeck, D. J. Hagler, and N. C. Spitzer. 1998. 'A calcium signaling cascade essential for myosin thick filament assembly in Xenopus myocytes', *J Cell Biol*, 141: 1349-56.

Feske, S. 2007. 'Calcium signalling in lymphocyte activation and disease', *Nat Rev Immunol*, 7: 690-702.

Foss, C. A., J. Sanchez-Bautista, and S. K. Jain. 2018. 'Imaging Macrophage-associated Inflammation', *Semin Nucl Med*, 48: 242-45.

Friedl, P., S. Borgmann, and E. B. Brocker. 2001. 'Amoeboid leukocyte crawling through extracellular matrix: lessons from the Dictyostelium paradigm of cell movement', *J Leukoc Biol*, 70: 491-509.

Friedrich, R. W., and S. I. Korsching. 1997. 'Combinatorial and chemotopic odorant coding in the zebrafish olfactory bulb visualized by optical imaging', *Neuron*, 18: 737-52.

Fuchs, S., A. Rensing-Ehl, C. Speckmann, B. Bengsch, A. Schmitt-Graeff, I. Bondzio, A. Maul-Pavicic, T. Bass, T. Vraetz, B. Strahm, T. Ankermann, M. Benson, A. Caliebe, R. Folster-Holst, P. Kaiser, R. Thimme, W. W. Schamel, K. Schwarz, S. Feske, and S. Ehl. 2012. 'Antiviral and regulatory T cell immunity in a patient with stromal interaction molecule 1 deficiency', *J Immunol*, 188: 1523-33.

Furman, D., J. Campisi, E. Verdin, P. Carrera-Bastos, S. Targ, C. Franceschi, L. Ferrucci, D. W. Gilroy, A. Fasano, G. W. Miller, A. H. Miller, A. Mantovani, C. M. Weyand, N. Barzilai, J. J. Goronzy, T. A. Rando, R. B. Effros, A. Lucia, N. Kleinstreuer, and G. M. Slavich. 2019. 'Chronic inflammation in the etiology of disease across the life span', *Nat Med*, 25: 1822-32.

Gallin, E. K. 1986. 'Ionic channels in leukocytes', *J Leukoc Biol*, 39: 241-54.

Gee, J. M., N. A. Smith, F. R. Fernandez, M. N. Economo, D. Brunert, M. Rothermel, S. C. Morris, A. Talbot, S. Palumbos, J. M. Ichida, J. D. Shepherd, P. J. West, M. Wachowiak, M. R. Capecchi, K. S. Wilcox, J. A. White, and P. Tvrdik. 2014. 'Imaging activity in neurons and glia with a Polr2a-based and cre-dependent GCaMP5G-IRES-tdTomato reporter mouse', *Neuron*, 83: 1058-72.

Gistera, A., and G. K. Hansson. 2017. 'The immunology of atherosclerosis', *Nat Rev Nephrol*, 13: 368-80.

Glenn Merrill-Skoloff, Christophe Dubois, Ben Atkinson, Barbara Furie, Bruce Furie. 2013. 'Part II: Tests of Platelet Function.' in Alan D. Michelson (ed.), *Platelets (Third Edition)* (Academic Press).

References

Goldman, D. W., F. H. Chang, L. A. Gifford, E. J. Goetzl, and H. R. Bourne. 1985. 'Pertussis toxin inhibition of chemotactic factor-induced calcium mobilization and function in human polymorphonuclear leukocytes', *J Exp Med*, 162: 145-56.

Goodwin, G. H., C. Sanders, and E. W. Johns. 1973. 'A new group of chromatin-associated proteins with a high content of acidic and basic amino acids', *Eur J Biochem*, 38: 14-9.

Grant, R. T. 1964. 'Direct Observation of Skeletal Muscle Blood Vessels (Rat Cremaster)', *J Physiol*, 172: 123-37.

Hamilton, T. A., C. Zhao, P. G. Pavicic, Jr., and S. Datta. 2014. 'Myeloid colony-stimulating factors as regulators of macrophage polarization', *Front Immunol*, 5: 554.

Harris, C. M. 1998. 'The Fourier analysis of biological transients', *J Neurosci Methods*, 83: 15-34.

Hato, T., and P. C. Dagher. 2015. 'How the Innate Immune System Senses Trouble and Causes Trouble', *Clin J Am Soc Nephrol*, 10: 1459-69.

He, S. J., J. Cheng, X. Feng, Y. Yu, L. Tian, and Q. Huang. 2017. 'The dual role and therapeutic potential of high-mobility group box 1 in cancer', *Oncotarget*, 8: 64534-50.

He, W., S. Holtkamp, S. M. Hergenhan, K. Kraus, A. de Juan, J. Weber, P. Bradfield, J. M. P. Grenier, J. Pelletier, D. Druzd, C. S. Chen, L. M. Ince, S. Bierschenk, R. Pick, M. Sperandio, M. Aurrand-Lions, and C. Scheiermann. 2018. 'Circadian Expression of Migratory Factors Establishes Lineage-Specific Signatures that Guide the Homing of Leukocyte Subsets to Tissues', *Immunity*, 49: 1175-90 e7.

Heim, N., O. Garaschuk, M. W. Friedrich, M. Mank, R. I. Milos, Y. Kovalchuk, A. Konnerth, and O. Griesbeck. 2007. 'Improved calcium imaging in transgenic mice expressing a troponin C-based biosensor', *Nat Methods*, 4: 127-9.

Helmchen, F., and W. Denk. 2005. 'Deep tissue two-photon microscopy', *Nat Methods*, 2: 932-40.

Hermani, A., B. De Servi, S. Medunjanin, P. A. Tessier, and D. Mayer. 2006. 'S100A8 and S100A9 activate MAP kinase and NF-kappaB signaling pathways and trigger translocation of RAGE in human prostate cancer cells', *Exp Cell Res*, 312: 184-97.

Huang, B. K., and M. A. Choma. 2015. 'Microscale imaging of cilia-driven fluid flow', *Cell Mol Life Sci*, 72: 1095-113.

Hyun, Y. M., Y. H. Choe, S. A. Park, and M. Kim. 2019. 'LFA-1 (CD11a/CD18) and Mac-1 (CD11b/CD18) distinctly regulate neutrophil extravasation through hotspots I and II', *Exp Mol Med*, 51: 1-13.

Ibrahim, Z. A., C. L. Armour, S. Phipps, and M. B. Sukkar. 2013. 'RAGE and TLRs: relatives, friends or neighbours?', *Mol Immunol*, 56: 739-44.

References

Jacobs, P., R. Bissonnette, and L. C. Guenther. 2011. 'Socioeconomic burden of immune-mediated inflammatory diseases--focusing on work productivity and disability', *J Rheumatol Suppl*, 88: 55-61.

Jung, S., J. Aliberti, P. Graemmel, M. J. Sunshine, G. W. Kreutzberg, A. Sher, and D. R. Littman. 2000. 'Analysis of fractalkine receptor CX(3)CR1 function by targeted deletion and green fluorescent protein reporter gene insertion', *Mol Cell Biol*, 20: 4106-14.

Khoshnam, S. E., W. Winlow, M. Farzaneh, Y. Farbood, and H. F. Moghaddam. 2017. 'Pathogenic mechanisms following ischemic stroke', *Neurol Sci*, 38: 1167-86.

Kolaczkowska, Elzbieta, and Paul Kubes. 2013. 'Neutrophil recruitment and function in health and inflammation', *Nature Reviews Immunology*, 13: 159-75.

Krebs, J., L. B. Agellon, and M. Michalak. 2015. 'Ca(2+) homeostasis and endoplasmic reticulum (ER) stress: An integrated view of calcium signaling', *Biochem Biophys Res Commun*, 460: 114-21.

Kunkel, E. J., and K. Ley. 1996. 'Distinct phenotype of E-selectin-deficient mice. E-selectin is required for slow leukocyte rolling in vivo', *Circ Res*, 79: 1196-204.

Lacruz, R. S., and S. Feske. 2015. 'Diseases caused by mutations in ORAI1 and STIM1', *Ann N Y Acad Sci*, 1356: 45-79.

Lad, P. M., C. V. Olson, I. S. Grewal, and S. J. Scott. 1985. 'A pertussis toxin-sensitive GTP-binding protein in the human neutrophil regulates multiple receptors, calcium mobilization, and lectin-induced capping', *Proc Natl Acad Sci U S A*, 82: 8643-7.

Lammermann, T. 2016. 'In the eye of the neutrophil swarm-navigation signals that bring neutrophils together in inflamed and infected tissues', *J Leukoc Biol*, 100: 55-63.

Lammermann, T., P. V. Afonso, B. R. Angermann, J. M. Wang, W. Kastenmuller, C. A. Parent, and R. N. Germain. 2013. 'Neutrophil swarms require LTB4 and integrins at sites of cell death in vivo', *Nature*, 498: 371-5.

Lammermann, T., and R. N. Germain. 2014. 'The multiple faces of leukocyte interstitial migration', *Semin Immunopathol*, 36: 227-51.

Lammermann, T., and M. Sixt. 2009. 'Mechanical modes of 'amoeboid' cell migration', *Curr Opin Cell Biol*, 21: 636-44.

Lefort, C. T., and K. Ley. 2012. 'Neutrophil arrest by LFA-1 activation', *Front Immunol*, 3: 157.

Lefort, C. T., J. Rossaint, M. Moser, B. G. Petrich, A. Zarbock, S. J. Monkley, D. R. Critchley, M. H. Ginsberg, R. Fassler, and K. Ley. 2012. 'Distinct roles for talin-1 and kindlin-3 in LFA-1 extension and affinity regulation', *Blood*, 119: 4275-82.

References

Ley, K., C. Laudanna, M. I. Cybulsky, and S. Nourshargh. 2007. 'Getting to the site of inflammation: the leukocyte adhesion cascade updated', *Nat Rev Immunol*, 7: 678-89.

Li, J. L., C. C. Goh, J. L. Keeble, J. S. Qin, B. Roediger, R. Jain, Y. Wang, W. K. Chew, W. Weninger, and L. G. Ng. 2012. 'Intravital multiphoton imaging of immune responses in the mouse ear skin', *Nat Protoc*, 7: 221-34.

Li, N., H. Yang, M. Wang, S. Lu, Y. Zhang, and M. Long. 2018. 'Ligand-specific binding forces of LFA-1 and Mac-1 in neutrophil adhesion and crawling', *Mol Biol Cell*, 29: 408-18.

Liu, C., Y. Liang, and L. Wang. 2020. 'Single-shot photoacoustic microscopy of hemoglobin concentration, oxygen saturation, and blood flow in sub-microseconds', *Photoacoustics*, 17: 100156.

Lou, O., P. Alcaide, F. W. Luscinskas, and W. A. Muller. 2007. 'CD99 is a key mediator of the transendothelial migration of neutrophils', *J Immunol*, 178: 1136-43.

Lucas, C., N. Barnich, and H. T. T. Nguyen. 2017. 'Microbiota, Inflammation and Colorectal Cancer', *Int J Mol Sci*, 18.

Lutcke, H., M. Murayama, T. Hahn, D. J. Margolis, S. Astori, S. M. Zum Alten Borgloh, W. Gobel, Y. Yang, W. Tang, S. Kugler, R. Sprengel, T. Nagai, A. Miyawaki, M. E. Larkum, F. Helmchen, and M. T. Hasan. 2010. 'Optical recording of neuronal activity with a genetically-encoded calcium indicator in anesthetized and freely moving mice', *Front Neural Circuits*, 4: 9.

Majno, G., G. E. Palade, and G. I. Schoefl. 1961. 'Studies on inflammation. II. The site of action of histamine and serotonin along the vascular tree: a topographic study', *J Biophys Biochem Cytol*, 11: 607-26.

Mantovani, A., P. Allavena, A. Sica, and F. Balkwill. 2008. 'Cancer-related inflammation', *Nature*, 454: 436-44.

Maravall, M., Z. F. Mainen, B. L. Sabatini, and K. Svoboda. 2000. 'Estimating intracellular calcium concentrations and buffering without wavelength ratioing', *Biophys J*, 78: 2655-67.

Mathias, J. R., B. J. Perrin, T. X. Liu, J. Kanki, A. T. Look, and A. Huttenlocher. 2006. 'Resolution of inflammation by retrograde chemotaxis of neutrophils in transgenic zebrafish', *J Leukoc Biol*, 80: 1281-8.

McAllister, R. G., D. R. Sisan, and J. S. Urbach. 2008. 'Design and optimization of a high-speed, high-sensitivity, spinning disk confocal microscopy system', *J Biomed Opt*, 13: 054058.

McCarl, C. A., C. Picard, S. Khalil, T. Kawasaki, J. Rother, A. Papolos, J. Kutok, C. Hivroz, F. Ledeist, K. Plogmann, S. Ehl, G. Notheis, M. H. Albert, B. H. Belohradsky, J. Kirschner, A. Rao, A. Fischer, and S. Feske. 2009. 'ORAI1 deficiency and lack of store-operated Ca2+ entry cause immunodeficiency, myopathy, and ectodermal dysplasia', *J Allergy Clin Immunol*, 124: 1311-18 e7.

McDonald, B., C. N. Jenne, L. Zhuo, K. Kimata, and P. Kubes. 2013. 'Kupffer cells and activation of endothelial TLR4 coordinate neutrophil adhesion within liver sinusoids during endotoxemia', *Am J Physiol Gastrointest Liver Physiol*, 305: G797-806.

Miyazaki, S., H. Shirakawa, K. Nakada, and Y. Honda. 1993. 'Essential role of the inositol 1,4,5-trisphosphate receptor/Ca2+ release channel in Ca2+ waves and Ca2+ oscillations at fertilization of mammalian eggs', *Dev Biol*, 158: 62-78.

Mossman, B. T., and A. Churg. 1998. 'Mechanisms in the pathogenesis of asbestosis and silicosis', *Am J Respir Crit Care Med*, 157: 1666-80.

Muik, M., I. Frischauf, I. Derler, M. Fahrner, J. Bergsmann, P. Eder, R. Schindl, C. Hesch, B. Polzinger, R. Fritsch, H. Kahr, J. Madl, H. Gruber, K. Groschner, and C. Romanin. 2008. 'Dynamic coupling of the putative coiled-coil domain of ORAI1 with STIM1 mediates ORAI1 channel activation', *J Biol Chem*, 283: 8014-22.

Musumeci, D., G. N. Roviello, and D. Montesarchio. 2014. 'An overview on HMGB1 inhibitors as potential therapeutic agents in HMGB1-related pathologies', *Pharmacol Ther*, 141: 347-57.

Napolitano, L. M. 2018. 'Sepsis 2018: Definitions and Guideline Changes', *Surg Infect (Larchmt)*, 19: 117-25.

Neeper, M., A. M. Schmidt, J. Brett, S. D. Yan, F. Wang, Y. C. Pan, K. Elliston, D. Stern, and A. Shaw. 1992. 'Cloning and expression of a cell surface receptor for advanced glycosylation end products of proteins', *J Biol Chem*, 267: 14998-5004.

Newton, K., and V. M. Dixit. 2012. 'Signaling in innate immunity and inflammation', *Cold Spring Harb Perspect Biol*, 4.

Ng, L. G., J. S. Qin, B. Roediger, Y. Wang, R. Jain, L. L. Cavanagh, A. L. Smith, C. A. Jones, M. de Veer, M. A. Grimbaldeston, E. N. Meeusen, and W. Weninger. 2011. 'Visualizing the neutrophil response to sterile tissue injury in mouse dermis reveals a three-phase cascade of events', *J Invest Dermatol*, 131: 2058-68.

Nourshargh, S., P. L. Hordijk, and M. Sixt. 2010. 'Breaching multiple barriers: leukocyte motility through venular walls and the interstitium', *Nat Rev Mol Cell Biol*, 11: 366-78.

Oishi, Y., and I. Manabe. 2018. 'Macrophages in inflammation, repair and regeneration', *Int Immunol*, 30: 511-28.

Oka, Y., S. Katada, M. Omura, M. Suwa, Y. Yoshihara, and K. Touhara. 2006. 'Odorant receptor map in the mouse olfactory bulb: in vivo sensitivity and specificity of receptor-defined glomeruli', *Neuron*, 52: 857-69.

Ong, H. L., L. B. de Souza, C. Zheng, K. T. Cheng, X. Liu, C. M. Goldsmith, S. Feske, and I. S. Ambudkar. 2015. 'STIM2 enhances receptor-stimulated Ca(2)(+) signaling by promoting recruitment of STIM1 to the endoplasmic reticulum-plasma membrane junctions', *Sci Signal*, 8: ra3.

Ong, H. S., and H. C. H. Yim. 2017. 'Microbial Factors in Inflammatory Diseases and Cancers', *Adv Exp Med Biol*, 1024: 153-74.

Ortega-Gomez, A., M. Perretti, and O. Soehnlein. 2013. 'Resolution of inflammation: an integrated view', *EMBO Mol Med*, 5: 661-74.

Park, S. A., Y. H. Choe, E. Park, and Y. M. Hyun. 2018. 'Real-time dynamics of neutrophil clustering in response to phototoxicity-induced cell death and tissue damage in mouse ear dermis', *Cell Adh Migr*, 12: 424-31.

Pflugfelder, S. C., M. Stern, S. Zhang, and A. Shojaei. 2017. 'LFA-1/ICAM-1 Interaction as a Therapeutic Target in Dry Eye Disease', *J Ocul Pharmacol Ther*, 33: 5-12.

Pham, C., D. H. Moro, C. Mouffle, S. Didienne, R. Hepp, F. W. Pfrieger, J. M. Mangin, P. Legendre, C. Martin, S. Luquet, B. Cauli, and D. Li. 2020. 'Mapping astrocyte activity domains by light sheet imaging and spatio-temporal correlation screening', *Neuroimage*, 220: 117069.

Picard, C., C. A. McCarl, A. Papolos, S. Khalil, K. Luthy, C. Hivroz, F. LeDeist, F. Rieux-Laucat, G. Rechavi, A. Rao, A. Fischer, and S. Feske. 2009. 'STIM1 mutation associated with a syndrome of immunodeficiency and autoimmunity', *N Engl J Med*, 360: 1971-80.

Pitchford, S., D. Pan, and H. C. Welch. 2017. 'Platelets in neutrophil recruitment to sites of inflammation', *Curr Opin Hematol*, 24: 23-31.

Prame Kumar, K., A. J. Nicholls, and C. H. Y. Wong. 2018. 'Partners in crime: neutrophils and monocytes/macrophages in inflammation and disease', *Cell Tissue Res*, 371: 551-65.

Prantner, D., S. Nallar, and S. N. Vogel. 2020. 'The role of RAGE in host pathology and crosstalk between RAGE and TLR4 in innate immune signal transduction pathways', *FASEB J*, 34: 15659-74.

Proebstl, D., M. B. Voisin, A. Woodfin, J. Whiteford, F. D'Acquisto, G. E. Jones, D. Rowe, and S. Nourshargh. 2012. 'Pericytes support neutrophil subendothelial cell crawling and breaching of venular walls in vivo', *J Exp Med*, 209: 1219-34.

Rahman, A., and F. Fazal. 2009. 'Hug tightly and say goodbye: role of endothelial ICAM-1 in leukocyte transmigration', *Antioxid Redox Signal*, 11: 823-39.

Rankin, S. M. 2010. 'The bone marrow: a site of neutrophil clearance', *J Leukoc Biol*, 88: 241-51.

Renkawitz, J., and M. Sixt. 2016. 'A Radical Break: Restraining Neutrophil Migration', *Dev Cell*, 38: 448-50.

References

Rudi Rottenfusser, Erin E. Wilson, Michael W. Davidson. 1999. 'Education in Microscopy and Digital Imaging'.http://zeisscampus.magnet.fsu.edu/articles/basics/fluorescence.html#:~:text=Fluoresc ence%20molecules%20can%20only%20absorb,yellow%20spectrum%20in%20Figure%202).

Russell, J. T. 2011. 'Imaging calcium signals in vivo: a powerful tool in physiology and pharmacology', *Br J Pharmacol*, 163: 1605-25.

Sadik, C. D., N. D. Kim, and A. D. Luster. 2011. 'Neutrophils cascading their way to inflammation', *Trends Immunol*, 32: 452-60.

Salomon, B., and J. A. Bluestone. 1998. 'LFA-1 interaction with ICAM-1 and ICAM-2 regulates Th2 cytokine production', *J Immunol*, 161: 5138-42.

Saxena, R., S. Ganguly, and A. Chattopadhyay. 2012. 'Comparative analysis of calcium spikes upon activation of serotonin(1A) and purinergic receptors', *PLoS One*, 7: e51857.

Scaffidi, P., T. Misteli, and M. E. Bianchi. 2002. 'Release of chromatin protein HMGB1 by necrotic cells triggers inflammation', *Nature*, 418: 191-5.

Schaff, U. Y., N. Dixit, E. Procyk, I. Yamayoshi, T. Tse, and S. I. Simon. 2010. 'Orai1 regulates intracellular calcium, arrest, and shape polarization during neutrophil recruitment in shear flow', *Blood*, 115: 657-66.

Schiraldi, M., A. Raucci, L. M. Munoz, E. Livoti, B. Celona, E. Venereau, T. Apuzzo, F. De Marchis, M. Pedotti, A. Bachi, M. Thelen, L. Varani, M. Mellado, A. Proudfoot, M. E. Bianchi, and M. Uguccioni. 2012. 'HMGB1 promotes recruitment of inflammatory cells to damaged tissues by forming a complex with CXCL12 and signaling via CXCR4', *J Exp Med*, 209: 551-63.

Semerad, C. L., F. Liu, A. D. Gregory, K. Stumpf, and D. C. Link. 2002. 'G-CSF is an essential regulator of neutrophil trafficking from the bone marrow to the blood', *Immunity*, 17: 413-23.

Serhan, C. N., S. K. Gupta, M. Perretti, C. Godson, E. Brennan, Y. Li, O. Soehnlein, T. Shimizu, O. Werz, V. Chiurchiu, A. Azzi, M. Dubourdeau, S. S. Gupta, P. Schopohl, M. Hoch, D. Gjorgevikj, F. M. Khan, D. Brauer, A. Tripathi, K. Cesnulevicius, D. Lescheid, M. Schultz, E. Sarndahl, D. Repsilber, R. Kruse, A. Sala, J. Z. Haeggstrom, B. D. Levy, J. G. Filep, and O. Wolkenhauer. 2020. 'The Atlas of Inflammation Resolution (AIR)', *Mol Aspects Med*, 74: 100894.

Serhan, C. N., and B. D. Levy. 2018. 'Resolvins in inflammation: emergence of the pro-resolving superfamily of mediators', *J Clin Invest*, 128: 2657-69.

Sharma, Y., S. Saha, A. Joseph, H. Krishnan, and P. Raghu. 2020. 'In vitro human stem cell derived cultures to monitor calcium signaling in neuronal development and function', *Wellcome Open Res*, 5: 16.

References

Shi, J., L. Hua, D. Harmer, P. Li, and G. Ren. 2018. 'Cre Driver Mice Targeting Macrophages', *Methods Mol Biol*, 1784: 263-75.

Smedler, E., and P. Uhlen. 2014. 'Frequency decoding of calcium oscillations', *Biochim Biophys Acta*, 1840: 964-9.

Soehnlein, O., L. Lindbom, and C. Weber. 2009. 'Mechanisms underlying neutrophil-mediated monocyte recruitment', *Blood*, 114: 4613-23.

Spangrude, G. J., F. Sacchi, H. R. Hill, D. E. Van Epps, and R. A. Daynes. 1985. 'Inhibition of lymphocyte and neutrophil chemotaxis by pertussis toxin', *J Immunol*, 135: 4135-43.

Stark, K., A. Eckart, S. Haidari, A. Tirniceriu, M. Lorenz, M. L. von Bruhl, F. Gartner, A. G. Khandoga, K. R. Legate, R. Pless, I. Hepper, K. Lauber, B. Walzog, and S. Massberg. 2013. 'Capillary and arteriolar pericytes attract innate leukocytes exiting through venules and 'instruct' them with pattern-recognition and motility programs', *Nat Immunol*, 14: 41-51.

Stephens, D. J., and V. J. Allan. 2003. 'Light microscopy techniques for live cell imaging', *Science*, 300: 82-6.

Sugimoto, M. A., J. P. Vago, M. M. Teixeira, and L. P. Sousa. 2016. 'Annexin A1 and the Resolution of Inflammation: Modulation of Neutrophil Recruitment, Apoptosis, and Clearance', *J Immunol Res*, 2016: 8239258.

Sumen, C., T. R. Mempel, I. B. Mazo, and U. H. von Andrian. 2004. 'Intravital microscopy: visualizing immunity in context', *Immunity*, 21: 315-29.

Summers, C., S. M. Rankin, A. M. Condliffe, N. Singh, A. M. Peters, and E. R. Chilvers. 2010. 'Neutrophil kinetics in health and disease', *Trends Immunol*, 31: 318-24.

Suratt, B. T., S. K. Young, J. Lieber, J. A. Nick, P. M. Henson, and G. S. Worthen. 2001. 'Neutrophil maturation and activation determine anatomic site of clearance from circulation', *Am J Physiol Lung Cell Mol Physiol*, 281: L913-21.

Szalai, G., R. Krishnamurthy, and G. Hajnoczky. 1999. 'Apoptosis driven by IP(3)-linked mitochondrial calcium signals', *EMBO J*, 18: 6349-61.

Tang, D., M. T. Loze, H. J. Zeh, and R. Kang. 2010. 'The redox protein HMGB1 regulates cell death and survival in cancer treatment', *Autophagy*, 6: 1181-3.

Tauzin, S., T. W. Starnes, F. B. Becker, P. Y. Lam, and A. Huttenlocher. 2014. 'Redox and Src family kinase signaling control leukocyte wound attraction and neutrophil reverse migration', *J Cell Biol*, 207: 589-98.

Thurley, K., S. C. Tovey, G. Moenke, V. L. Prince, A. Meena, A. P. Thomas, A. Skupin, C. W. Taylor, and M. Falcke. 2014. 'Reliable encoding of stimulus intensities within random sequences of intracellular Ca2+ spikes', *Sci Signal*, 7: ra59.

Tirone, M., N. L. Tran, C. Ceriotti, A. Gorzanelli, M. Canepari, R. Bottinelli, A. Raucci, S. Di Maggio, C. Santiago, M. Mellado, M. Saclier, S. Francois, G. Careccia, M. He, F. De Marchis, V. Conti, S. Ben Larbi, S. Cuvellier, M. Casalgrandi, A. Preti, B. Chazaud, Y. Al-Abed, G. Messina, G. Sitia, S. Brunelli, M. E. Bianchi, and E. Venereau. 2018. 'High mobility group box 1 orchestrates tissue regeneration via CXCR4', *J Exp Med*, 215: 303-18.

Tsien, R. Y. 1981. 'A non-disruptive technique for loading calcium buffers and indicators into cells', *Nature*, 290: 527-8.

Uderhardt, S., A. J. Martins, J. S. Tsang, T. Lammermann, and R. N. Germain. 2019. 'Resident Macrophages Cloak Tissue Microlesions to Prevent Neutrophil-Driven Inflammatory Damage', *Cell*, 177: 541-55 e17.

Uhlen, P. 2004. 'Spectral analysis of calcium oscillations', *Sci STKE*, 2004: pl15.

Vaeth, M., and S. Feske. 2018. 'Ion channelopathies of the immune system', *Curr Opin Immunol*, 52: 39-50.

Vaure, C., and Y. Liu. 2014. 'A comparative review of toll-like receptor 4 expression and functionality in different animal species', *Front Immunol*, 5: 316.

Venereau, E., M. Casalgrandi, M. Schiraldi, D. J. Antoine, A. Cattaneo, F. De Marchis, J. Liu, A. Antonelli, A. Preti, L. Raeli, S. S. Shams, H. Yang, L. Varani, U. Andersson, K. J. Tracey, A. Bachi, M. Uguccioni, and M. E. Bianchi. 2012. 'Mutually exclusive redox forms of HMGB1 promote cell recruitment or proinflammatory cytokine release', *J Exp Med*, 209: 1519-28.

Vladymyrov, M., J. Abe, F. Moalli, J. V. Stein, and A. Ariga. 2016. 'Real-time tissue offset correction system for intravital multiphoton microscopy', *J Immunol Methods*, 438: 35-41.

Voisin, M. B., A. Woodfin, and S. Nourshargh. 2009. 'Monocytes and neutrophils exhibit both distinct and common mechanisms in penetrating the vascular basement membrane in vivo', *Arterioscler Thromb Vasc Biol*, 29: 1193-9.

Wang, H., O. Bloom, M. Zhang, J. M. Vishnubhakat, M. Ombrellino, J. Che, A. Frazier, H. Yang, S. Ivanova, L. Borovikova, K. R. Manogue, E. Faist, E. Abraham, J. Andersson, U. Andersson, P. E. Molina, N. N. Abumrad, A. Sama, and K. J. Tracey. 1999. 'HMG-1 as a late mediator of endotoxin lethality in mice', *Science*, 285: 248-51.

References

Wang, Q., G. Zhu, X. Cao, J. Dong, F. Song, and Y. Niu. 2017. 'Blocking AGE-RAGE Signaling Improved Functional Disorders of Macrophages in Diabetic Wound', *J Diabetes Res*, 2017: 1428537.

Wang, Y., F. Du, A. Hawez, M. Morgelin, and H. Thorlacius. 2019. 'Neutrophil extracellular trap-microparticle complexes trigger neutrophil recruitment via high-mobility group protein 1 (HMGB1)-toll-like receptors(TLR2)/TLR4 signalling', *Br J Pharmacol*, 176: 3350-63.

Webb, S. E., and A. L. Miller. 2000. 'Calcium signalling during zebrafish embryonic development', *Bioessays*, 22: 113-23.

Weber, C., and H. Noels. 2011. 'Atherosclerosis: current pathogenesis and therapeutic options', *Nat Med*, 17: 1410-22.

Wegmann, F., B. Petri, A. G. Khandoga, C. Moser, A. Khandoga, S. Volkery, H. Li, I. Nasdala, O. Brandau, R. Fassler, S. Butz, F. Krombach, and D. Vestweber. 2006. 'ESAM supports neutrophil extravasation, activation of Rho, and VEGF-induced vascular permeability', *J Exp Med*, 203: 1671-7.

Weninger, W., M. Biro, and R. Jain. 2014. 'Leukocyte migration in the interstitial space of non-lymphoid organs', *Nat Rev Immunol*, 14: 232-46.

Wilgus, T. A., S. Roy, and J. C. McDaniel. 2013. 'Neutrophils and Wound Repair: Positive Actions and Negative Reactions', *Adv Wound Care (New Rochelle)*, 2: 379-88.

Wipf, P., B. R. Eyer, Y. Yamaguchi, F. Zhang, M. D. Neal, C. P. Sodhi, M. Good, M. Branca, T. Prindle, Jr., P. Lu, J. L. Brodsky, and D. J. Hackam. 2015. 'Synthesis of anti-inflammatory alpha-and beta-linked acetamidopyranosides as inhibitors of toll-like receptor 4 (TLR4)', *Tetrahedron Lett*, 56: 3097-100.

Wojcikiewicz, E. P., M. H. Abdulreda, X. Zhang, and V. T. Moy. 2006. 'Force spectroscopy of LFA-1 and its ligands, ICAM-1 and ICAM-2', *Biomacromolecules*, 7: 3188-95.

Woodfin, A., M. B. Voisin, M. Beyrau, B. Colom, D. Caille, F. M. Diapouli, G. B. Nash, T. Chavakis, S. M. Albelda, G. E. Rainger, P. Meda, B. A. Imhof, and S. Nourshargh. 2011. 'The junctional adhesion molecule JAM-C regulates polarized transendothelial migration of neutrophils in vivo', *Nat Immunol*, 12: 761-9.

Zamponi, G. W. 2015. 'Calcium Channel Signaling Complexes with Receptors and Channels', *Curr Mol Pharmacol*, 8: 8-11.

Zhang, D., G. Chen, D. Manwani, A. Mortha, C. Xu, J. J. Faith, R. D. Burk, Y. Kunisaki, J. E. Jang, C. Scheiermann, M. Merad, and P. S. Frenette. 2015. 'Neutrophil ageing is regulated by the microbiome', *Nature*, 525: 528-32.

Zhou, X., Z. Li, Z. Wang, E. Chen, J. Wang, F. Chen, O. Jones, T. Tan, S. Chen, H. Takeshima, J. Bryant, J. Ma, and X. Xu. 2018. 'Syncytium calcium signaling and macrophage function in the heart', *Cell Biosci*, 8: 24.

Zonneveld, R., G. Molema, and F. B. Plotz. 2016. 'Analyzing Neutrophil Morphology, Mechanics, and Motility in Sepsis: Options and Challenges for Novel Bedside Technologies', *Crit Care Med*, 44: 218-28.

Zou, W., X. Meng, C. Cai, M. Zou, S. Tang, X. Chu, X. Wang, and F. Zou. 2012. 'Store-operated Ca2+ entry (SOCE) plays a role in the polarization of neutrophil-like HL-60 cells by regulating the activation of Akt, Src, and Rho family GTPases', *Cell Physiol Biochem*, 30: 221-37.

Appendix

Matlab code 'Signal detrending'

```matlab
workbook = 'Imaris Output Sheet.xls'; % excel sheet output from Imaris
green_sheet = 'Intensity Mean Ch=2'; % specific sheet for green channel
red_sheet = 'Intensity Mean Ch=3'; % specific sheet for red channel
time_sheet = 'Time'; % specific sheet for time sheet
green = xlsread(workbook,green_sheet,'A:A'); % green channel intensity
values
red = xlsread(workbook,red_sheet,'A:A'); % red channel intensity values
time = xlsread(workbook,time_sheet,'A:A'); % time in seconds
norm.intensity = (green)./(red); % normalized intensity
degree = 1;
trend = polyfit(time,norm.intensity,degree);
norm.intensity_new = norm.intensity - polyval(trend,time);
c2=[norm.intensity,time];
T = array2table(c2, 'VariableNames', {'Norm_Intensity','Time'}
filename = 'Intermediate Sheet F_Fo.xls';
writetable (T,filename,'Sheet',1);
```

Matlab code 'Signal filtering and peak finding'

```
workbook = 'Intermediate Sheet F_Fo'; % excel sheet output from Signal
detrending
Tabelle1 = 'Tabelle1'; % specific sheet where all norm_intensity,
diff_in_norm_intensity and time are found
time = xlsread(workbook,Tabelle1,'B:B');
Time = time./60; % seconds to minutes
norm_int = xlsread(workbook,Tabelle1,'A:A');
mp = 0.3*[max(norm_int) - min(norm_int)]; % generalized formula for
obtaining a value for MinPeakProminence that is dependent on amplitude
of intensity
% Positive_&_Negative_peaks_AllInteraction %
AllInteractionCubicMA = sgolayfilt(norm_int,3,7);
[pAllInteraction, lAllInteraction,WidthPosPeaksAllInteraction] =
findpeaks(AllInteractionCubicMA,'MinPeakProminence',mp);
plot(Time,AllInteractionCubicMA);hold on
plot(Time(lAllInteraction),pAllInteraction,'ko','MarkerFaceColor','y');
[Pks,Locs] =
findpeaks(AllInteractionCubicMA,Time,'MinPeakProminence',mp);
[PksNeg,LocsNeg] = findpeaks(-
AllInteractionCubicMA,Time,'MinPeakProminence',mp);
[pAllInteraction2, lAllInteraction2,WidthNegPeaksAllInteraction] =
findpeaks(-AllInteractionCubicMA,'MinPeakProminence',mp);
plot(Time(lAllInteraction2),-
pAllInteraction2,'ko','MarkerFaceColor','m');
xlabel('Time (min)');
ylabel('Fnorm');
Ave_int = sum(AllInteractionCubicMA)/numel(AllInteractionCubicMA);
Pos_ave = sum(pAllInteraction)/numel(pAllInteraction);
Neg_ave = sum(-pAllInteraction2)/numel(pAllInteraction2);
amp = Pos_ave - Neg_ave;
Results = [Ave_int,Pos_ave,Neg_ave,amp];
T = array2table(Results, 'VariableNames',
{'Pos_ave''Pos_ave','Neg_ave','amp'})
filename = 'Results.xls';
writetable (T,filename,'Sheet',1);
```

Acknowledgements

I would like to express my heartfelt gratitude to my supervisor PD. Dr. med. Konstantin Stark without whose support I would not have gotten to this stage. Your dedication to your supervision role on top of your daily tasks as a medical doctor are really admirable. Our special situation required you to stay beyond normal working hours for meetings, take phone calls from me late at night, and read and reply to emails at very odd hours. I would also like to thank Prof. Dr. med. Steffen Massberg for having taken the time to help supervise my PhD project with the rest of my thesis advisory committee members, Prof. Dr. med. Christian Schulz and PD. Dr. rer. nat. Markus Moser.

In addition, I would like to extend my sincere thanks my colleagues who made it possible for me to successfully enter a new field of research: Meike Miller, Gerhild Rosenberger, Leo Nicolai, Hellen Ishikawa, Bernd Uhl, Laura Mittmann, Gabriele Zuchtriegel, for having taught me the basics of working with laboratory rodents and intravital imaging, Kami Pekayvaz for the jolly working atmosphere in the office, catering for many memorable moments, as well as for his scientific advice, and Annegret Boda for all the help during long microscopy sessions. Many of my imaging sessions would have been unsuccessful had it not been for Dominic van den Heuvel's constant assistance. My special thanks also go to Michael Lorenz, Verena Kochan, and Steffi Regenfelder who made sure things ran in order in this journey. I would also like to thank Prof. Dr. med. Markus Sperandio, Prof. Dr. Barbara Walzog and their working groups for their willingness to collaborate. I would like to say a collective thank you to the whole AG Massberg who made working in the lab an enjoyable experience.

Finally, I am extremely grateful to my family for their support and unabated encouragements throughout my life: my father 'Ababa' for having instilled his love for science in me, my mother 'Emama' for having been a rock solid foundation to everything I am today, and my two elder brothers Yisihak and Miki along with their families for providing all the help one could need. Last and most importantly, the highest gratitude goes to my wife Firehiwot for having accompanied me through this rocky journey. Although having spent most of this PhD journey in separate countries, your support was there whenever I needed it. Your willingness to discuss my line of work, to critic my manuscript, and to continuously nudge me to the finish line has been invaluable. Here is to more of this but in the same city.

Affidavit

Affidavit

Mehari, Fitsumbirhan Tetemke
_____

Surname, first name

Vladimir-Prelog-Weg 1-5/10
_____

Street

8093, Zurich, Switzerland
_____

Zip code, town, country

I hereby declare, that the submitted thesis entitled:

The role of calcium signaling in myeloid leukocyte activation and interactions in inflammation

is my own work. I have only used the sources indicated and have not made unauthorised use of services of a third party. Where the work of others has been quoted or reproduced, the source is always given.

I further declare that the submitted thesis or parts thereof have not been presented as part of an examination degree to any other university.

Zurich, 04.05.2021   Fitsumbirhan Tetemke Mehari
_____   _____

place, date   Signature doctoral candidate

Confirmation of congruency

Confirmation of congruency between printed and electronic version of the doctoral thesis

Mehari, Fitsumbirhan Tetemke

Surname, first name

Vladimir-Prelog-Weg 1-5/10

Street

8093, Zurich, Switzerland

Zip code, town, country

I hereby declare, that the submitted thesis entitled:

The role of calcium signaling in myeloid leukocyte activation and interactions in inflammation

is congruent with the printed version both in content and format.

Zurich, 04.05.2021

place, date

Fitsumbirhan Tetemke Mehari

Signature doctoral candidate